Noise modelling, Vibro-acoustic Analysis, Artificial neural networks on offshore platform

A Dissertation

Presented to

the Faculty

By

Xi Ji

In Partial Fulfillment

of the Requirements for the Degree

Doctor of Philosophy in the

Marine Technology

Newcastle University

June, 2018

Abstract

Due to the limitations of the present noise prediction methods used in the offshore industry, this research is aimed to develop an efficient noise prediction technique that can analyze and predict the noise level for the offshore platform environment during the design stage as practically as possible to meet the criteria for crews' comfort against high noise level.

Several studies have been carried out to improve the understanding of acoustic environment onboard offshore platform, as well as the present prediction techniques. The noise prediction methods for the offshore platform were proposed from three aspects: by empirical acoustic modeling, analytical computation or neural network method. First, through evaluating the five-selected empirical acoustic models originated from other applications and statistical energy analaysis with direct field (SEA-DF), Heerema and Hodgson model was selected for calculating the sound level in the machinery room on the offshore platform.

Second, the analytical model modeled three-dimensional fully coupled structural and acoustic systems by considering of the structural coupling force and the moment at edges, and structural-acoustic interaction on the interface. Artificial spring technique was implemented to illustrate the general coupling and boundary conditions. The use of Chebyshev expansions solutions ensured the accuracy and rapid convergence of the three-dimensional problem of single room and conjugate rooms. The proposed model was validated by checking natural frequencies and responses of against the results obtained from finite element software.

Third, a modified multiple generalised regression neural network (GRNN) was first proposed to predict the noise level of various compartments onboard of the offshore platform with limited samples available. By preprocessing the samples with fuzzy c-means (FCM) and principal component analysis (PCA), dominant input features can be identified before commencing the GRNN's training process. With optimal spread variables, the newly developed tool showed comparable performance to the SEA-DF and empirical formula that requires less time and resources to solve during the early stage of the offshore platform design.

Acknowledgements

Table of Contents

List of Table

x

List of Figures

List of Symbols

SEA model

Π_i^{in} External power entering the SEA subsystem

Π_i^{diss} Power dissipated in the SEA subsystem

Π_{ij} Power exchanged between the SEA subsystem i and j.

η_{ii} Internal loss factor of SEA subsystem i

E_i Averaged energy of SEA subsystem i

n_i Modal density of subsystem i

Empirical models

$L_{p,rev}$ Reverberant field sound pressure level

$L_{p,rev}$ Direct field sound pressure level

$L_{p,total}$ Total sound pressure level

L_w Sound power level

V_i Volume of cavity i

r Source/receiver distance

$\overline{\alpha}$ Mean absorption coefficient

TM Room temperature

BP Barometric pressure

S_i Surface area of cavity i

S_H Hard non-boundary areas

S_s Soft non-boundary areas

S_f Total surface area of the fittings exposed to the sound field

α_H Area coefficient factor for hard surfaces

α_S Area coefficient factor for softsurfaces

α_{min} Minimum room constant value

R_{min} Minimum room constant

F Fitting density

W Room width

H   Height of common construction with furnishings

Analytical model

p_T	Total pressure value of
p_0	Steady pressure value
Δp	Variation pressure value
$p_{incidence}$	Incidence pressure
$p_{transmit}$	Transmitted pressure
ρ_T	Total density
ρ_0	Steady density
$\Delta \rho$	Variation density
u_T	Total acoustic velocity
u_0	Steady acoustic velocity
Δu_0	Variation acoustic velocity
c	Speed of sound
$\mathbf{r} = (x, y, z)$	Coordinates in the acoustic domain
w	Transverse vibration displacement
u	In-plane vibration displacement in the x-direction
v	In-plane vibration displacement in the y-direction
h_s	plate thickness
ρ_s	Structure density
υ	Poisson ratio
D	Bending stiffness
G	Extensional rigidity
E	Young's modulus
K_w	Rotational boundary spring stiffnes
k_w	Transverse boundary spring stiffness
k_p	In-plane boundary spring stiffness in the x-direction
k_n	In-plane boundary spring stiffness in the y-direction
K_{c_ij}	Rotational coupling spring stiffnes
k_{cw_ij}	Transverse coupling spring stiffness

k_{cu_ij}	In-plane coupling spring stiffness in the x-direction
k_{cv_ij}	In-plane coupling spring stiffness in the y-direction
Q_i	Transverse shear force
M_i	Transverse moment
$L_{i,x}$	Length of plate i in the x-direction
$L_{i,y}$	Width of plate i in the y-direction
L_X	Length of cavity in the X-direction
L_Y	Width of cavity in the Y-direction
L_Z	Height of cavity in the Z-direction
L^S	Lagrangian function of the structural domain
L^A	Lagrangian function of the acoustic domain
$L_{AP,x}$	Length of aperture in the x-direction
$L_{AP,y}$	Width of aperture in the y-direction
V_i^S	Overall potential energy of plate i
V_i^T	Potential energy of plate i due to transverse deformation
V_i^{In}	Potential energy of plate i due to in-plane deformation
T_i^S	Overall kinetic energy of plate i
T_i^T	Kinetic energy of plate i due to transverse deformation
T_i^{In}	Kinetic energy of plate i due to in-plane deformation
W_i^{AS}	Work done by the interior acoustic pressure loading on the mutual structural-acoustic interface
W_i^F	Work done by external force
V_{ij}^C	Potential energy generated by coupling effect and stored in the coupling springs between plate i and j
x_i, y_i	Cartesian coordinates of structural domain
X, Y, Z	Cartesian coordinates of acoustic domain
α_i, β_i	Chebyshev coordinates of structural domain
$\alpha, \beta, \varepsilon$	Chebyshev coordinates of acoustic domain
$A_{i,m,n}, B_{i,m,n}, C_{i,m,n}, E_{mx,my,mz}$	Unknown coefficients of the Chebyshev expansions for the transverse displacement, in-plane displacements in x- and y-

	direction, and acoustic pressure, respectively
$T_{\Xi_i}(\chi)$	One-dimensional Chebyshev polynomial of the first kind
m, n, mx, my, mz	Order of polynomial
M, N	Truncate number for the structural domain
M_X, M_Y, M_Z	Truncate number for the acoustic domain
$\mathbf{K}_S$	Generalized global stiffness matrices of the structural domain
$\mathbf{M}_S$	Generalized global mass matrices of the acoustic domain
$\mathbf{K}_A$	Generalized global stiffness matrices of the acoustic domain
$\mathbf{M}_A$	Generalized global mass matrices of the structural domain
$\mathbf{P}$	External pressure loading vector
$\mathbf{F}$	External force loading vector
$\mathbf{C}_{SA}$	Global structure-acoustic coupling matrix
ω	Natural frequency
$N_{s,in}$	Number of interior plate
$N_{s,ex}$	Number of exterior plates
TL	Transmission loss
R_0	Mass Law sound transmission loss

FCM-PCA- GRNN model

L_{adj}	Sound pressure level of the adjacent room
L_{source}	Sound pressure level of the source room
L_{SB}	Structure-borne sound pressure level
L_V	Structure vibration level
σ	Radiation efficiency
S_C	Area of common plate
S_{adj}	Surface area of the adjacent receiver room
α_{adj}	Mean absorption coefficient of the adjacent receiver room
P_{rev}^i	Reverberant sound power
P_{in}^i	Total injected sound power
$\mathbf{X}$	Total number of samples

μ_{ji}	Membership
v_j	j^{th} cluster centre
m	Fuzziness index
$d(x_i, v_j)$	Euclidean distance between ith data and jth cluster's center
$J(\mathbf{X}; \mathbf{U}, \mathbf{V})$	Objective function
X_i^j	Input samples
N^j	Number of samples in the jth cluster
h	Number of eigenvectors for eigenvalues
$f(\mathbf{X}^j, y^j)$	Probability density function
$\hat{f}(\mathbf{X}^j, y^j)$	Probability estimator

Chapter 1. Introduction

1.1   Background and Motivation

Over the past years, the steady growing requirements for acoustic performance of products as well as comfortable working and living conditions, has made the interior acoustic behavior an important criterion in the offshore industry. In this framework, the vibro-acoustics in the steel constructed environment is significant and will become even more important over the next decades with increasingly restrictive legal regulations regarding the interior noise levels [1-3]. With regarding the noise emission characteristic from onboard machinery and human audition, regulations concern about the maximum permissible noise levels which covers the broad frequency range from 31.5 Hz to 8000 Hz for different spaces. Such areas may be classified as follows.

- Machinery spaces, where speech communication is not important and hearing conservation is the primary concern
- Working space, where speech communication is required and levels are specified in the frequency bands associated with speech interference, and
- Living spaces, where comfort is desirable and the specified levels are therefore lower than those required to protect hearing

The compact arrangement of high noise level equipment and steel constructed hull structures make the offshore platform a complex dynamic system reflected on noise sources emission and the paths transmission. The noise situation on board an offshore platform is determined by the sum of noise contributed by the many and varied forms of noise sources. Besides the airborne noises generated by the operating equipment, such as diesel generator, mud pump, cement pump, compressor, shaker, and drill floor [4], structure-borne sound is another important form. Vibrating structure directly induced by rotating machineries generated mechanical force acts as loading to the surrounding medium and generates the fluctuation of the pressure levels. The interactions between structure and surrounding medium have impact on the medium, also the motions of the structure [5]. In machinery spaces containing high level noise sources, sound level may be entirely governed by airborne sound; in some remote living spaces, with the possible exception of rooms directly adjoining a source, the noise level may be determined by structure-borne sound; but more frequently, the sound field of offshore platform compartments is influenced by both type of the sources. Therefore, noise calculation

for offshore platform shall consider both structure domain and acoustic domain. In other words, it is a vibro-acoustic analysis [6].

It is a remarkable fact that implementing noise control at design product design stage is more cost effective than reconstruction. Through performing noise calculation for all spaces in the offshore platform, if the initial design is found to be acoustically insufficient, the effects of improved sound insulation and general arrangement can readily be calculated. Therefore, reliable engineering prediction tools which can be used for parameter studies are of practical interest.

Over the last decades, Computer Aided Design (CAD) techniques have evolved into mature and widely used tools to support the geometrical design process to allow for digital mock-up creation. And numbers of CAD-based modeling and analysis tools for vibro-acoustic analysis exist. However, specific methods are restricted by a frequency range. At low frequencies (large wavelengths), the response of the system is usually described in terms of modes, and typically calculated using deterministic approach; at high frequencies with short wavelengths, statistical approaches are usually adopted. In this context, novel prediction tools have been developed to analyse the vibro-acoustics of the offshore platform environment, and predict the sound pressure level in a practical way for the broad frequency range.

1.2   Research Objectives

There is a lack of calculation techniques in offshore platform noise prediction which can be used in the entire frequency range of interest (31.5-8000 Hz). Statistical models can only be used at higher frequencies. Models taking into account the finite dimensions and modal behavior are restricted to the lower frequency range, especially if one wants to investigate more complex structures with finite element techniques. Analytical models looking at the vibro-acoustics problem only deal with cavity backed by plate configuration that is not applicable for offshore platform environment. The feasibility of applying the empirical formula originated from land-based industry room and merchant ships to the offshore platform machinery room is unknown.

This research aims to develop prediction tools for an offshore platform which is practical and can be used in a broad frequency range. The tools are proposed in three aspects: empirically

modeling, analytical modeling, and neural network modeling. First, the suitable empirical sound pressure level model is selected for the machinery room based on an evaluation of five empirical model originated from other application. Second, the analytical tool is based on Raleigh-Ritz method which has already been used successfully for a range of vibro-acoustic problems. A full three-dimensional structural-acoustic description allows reliable predictions in the low-frequency range. The superior convergence rate of the Raleigh-Ritz method compared to finite element models makes computations possible up to higher frequencies. The purpose of this tool is to get a better understanding of the vibro-acoustics of more complex finite-sized structures. The focus of the dissertation will be on noise prediction by neural network model. It is an innovation way of performing noise prediction for the offshore platform as compared to the classical methods.

1.3   Outline of the dissertation

Chapter 2 reviews the present technology on predicting vibro-acoustics, including THE analytical solutions for Vibro-acoustics, Finite Element Analysis (FEA) for the structural domain, Statistical Energy Analysis (SEA) for vibro-acoustic, Empirical methods for solving machinery room interior acoustic, and Artificial neural network method (ANN).

Chapter 3 evaluates the five empirical models mentioned in section 2.4 in the machinery rooms. Heerema and Hodgson sound pressure model exhibits very close to the experimental measurement results as compared to the rest. The statistical energy analysis with direct field (SEA-DF) approach presented in section 2.3 correctly predicted the machinery room's sound pressure level under both airborne and structure-borne sounds influences. A small deviation on the spatial averaging noise level is obtained as compared to the experimental measurements. The noise control strategy such as implementing acoustic insulation and damping treatment is investigated by using the SEA. The evaluated SEA-DF model in this chapter serves as the sample collection method for the neural network modeling in chapter 6.

In Chapter 4, an analytical model for the three-dimensional vibro-acoustics problem is presented. Considering the structural interaction force and the moment at edges, and structural-acoustic interaction on the interface, the structural and acoustic systems are fully coupled. Artificial spring technique is implemented to illustrate the general coupling and boundary conditions by assigning the springs with corresponding values. The use of Chebyshev expansions solutions ensure the result accuracy and rapid convergence that enable the complex three-dimensional problem to be solved analytically. The proposed model is

validated by checking eigen-frequencies and eigenvector of present methodology against those derived from finite element software.

In Chapter 5, the analytical model described in Chapter 4 is extended to handle more general configuration such as the conjugate room and coupled room instead of a single room.

Chapter 6 proposes a modified multiple generalised Regression Neural Network to predict the noise level of various compartments on board of an offshore platform. With limited samples collected from the SEA-DF, conventional GRNN can cause an error when it maps the available inputs to sound levels for the offshore platform. In addition, the problem of selecting suitable inputs parameters in each cluster is often impeded by lacking accurate information. Fuzzy C-Mean (FCM) is used to obtain more relevant group for GRNNs training, and Principal Component Analysis (PCA) is used to remove the outliers in the groups, so that ensure high relevance input variables in each cluster. By fusing multiple GRNNs by an optimal spread parameter, the proposed modeling scheme becomes quite useful for modeling multiple frequency dependent datasets with different input parameters. The performance of FCM-PCA-GRNN shows comparable performance to the analytical results and SEA-DF that requires more time and resources to solve during the early stage of the offshore platform design.

In Chapter 7 the key findings and contributions of the thesis are stated, as well as the related publications published during the Ph.D. works are shown. It is followed by potential future research works.

Chapter 2.   Literature Review

Vibro-acoustics is a dynamic interaction between acoustic (fluid) and structure domains. Whenever an elastic structure is in contact with a medium, the structural vibrations and the acoustic pressure field in the cavity are influenced by the mutual vibro-acoustic coupling interaction. The force loading on the structure, caused by the acoustic pressure along the fluid-structure interface, influences the structural vibrations. At the same time the acoustic pressure field in the cavity is also sensitive to the structural vibrations along the fluid-structure interface. The strength of this vibro-acoustic coupling interaction is largely dependent on the geometry of the structure and the fluid domain as well as on the fluid and structural material properties and the frequency of the dynamic disturbances. This section give a summary of the various approaches usually used to predict noise inside cavities and to review the major developments in these areas to serve as a starting point of the thesis.

2.1 Analytical solution for Vibro-acoustics

Vibro-acoustics is a topic that has been of interest to researchers for long history. During the analytical modeling, the acoustic medium is assumed to be perfect, compressible and adiabatic fluid, therefore, sound in the fluid (acoustic) domain can be described by the linear theory [7]. The acoustic wave propagation causes small changes in displacement and velocity of fluid particles. The basic variables of a fluid are the total pressure p_T and the total density ρ_T. Both can be described using a steady value (p_0 and ρ_0) and small variations (Δp and $\Delta \rho$). Similarly, the total acoustic velocity u_T can be defined

$$p_T(\mathbf{r},t) = p_0(\mathbf{r}) + \Delta p(\mathbf{r},t); \rho_T(\mathbf{r},t) = \rho_0(\mathbf{r}) + \Delta \rho(\mathbf{r},t); \mathbf{u}_T(\mathbf{r},t) = \mathbf{u}_0(\mathbf{r}) + \Delta \mathbf{u}(\mathbf{r},t); \qquad [2\text{-}1]$$

The mass conservation and linear momentum laws can be written regarding acoustic variables

$$\frac{\partial p(\mathbf{r},t)}{\partial t} + \rho_0 \nabla \mathbf{u} = 0 \qquad\qquad \text{[2-2]}$$

$$\rho_0 \frac{\partial \mathbf{u}(\mathbf{r},t)}{\partial t} + \nabla p(\mathbf{r},t) = 0 \qquad\qquad \text{[2-3]}$$

where the ∇ is the gradient representing the spatial derivative $\frac{\partial}{\partial x}, \frac{\partial}{\partial y}, \frac{\partial}{\partial z}$ .The linear relationship between pressure and density can be found though the adiabatic compression process in a small cavity driven by a vibrating piston.

$$p(\rho) = \rho \left(\frac{\partial p_T}{\partial \rho_T} \right)_{\rho_0} \qquad\qquad \text{[2-4]}$$

The constitutive equation for the acoustic fluid can be written as

$$\nabla p(\mathbf{r},t) = c^2 \rho(\mathbf{r},t) \qquad\qquad \text{[2-5]}$$

where c is the speed of sound and it is a constant value for linear fluids. The enclosed fluid is modelled with the linear wave equation which obtained by substituting equation [2-5] into equation [2-2] and [2-3]

$$\nabla^2 p(\mathbf{r},t) = \frac{1}{c^2} \frac{\partial^2 p(\mathbf{r},t)}{\partial t^2} \qquad\qquad \text{[2-6]}$$

where $\mathbf{r} = (x, y, z)$ denotes the coordinates in the acoustic domain. This linear wave equation is the governing equation of an acoustic fluid.

When additional information supplied to generate the sound field such as surfaces that reflect or absorb sound, objects that scatter sound, etc. boundary conditions are imposed. From acoustic point of view, four types boundaries are usually encountered, namely the rigid boundary S_1, the flexible boundary S_2, the impedance boundary condition S_3, and the elastic boundary condition S_4. In this thesis, according to the characteristic of offshore platform, we mainly concern about the elastic boundary condition, in which the acoustic pressure and particle velocity satisfy the continuity relationship

$$\frac{\partial p(\mathbf{r},t)}{\partial n}\bigg|_{s_4} = -j\omega^2 \rho_0 w(\mathbf{r_s},t) \qquad \text{[2-7]}$$

where n is the outer unit normal vector [8], w is the vibration displacement in the normal direction.

The fluid domain is determined via a solution of a three-dimensional wave equation [2-6] with specified initial and boundary conditions such as equation [2-7]. The acoustic room response can be considered as a superposition of individual responses of normal acoustic modes generated inside the room by a harmonic sound source. Acoustic modes are inherent properties of the enclosure, and are determined by a room geometry and boundary condition [9].

In the structural domain, vibration excited by the source is propagating throughout the entire offshore platform. The attenuation of vibration energy depends on losses in the structure, the number of obstructions or junctions in the propagation path, and the connecting manner between structures.

The governing differential equation for free transverse and in-plane vibration of a plate is given by [10] [11]

$$D\left(\frac{\partial^4 w(x,y,t)}{\partial x^4} + \frac{\partial^4 w(x,y,t)}{\partial x^2 \partial y^2} + \frac{\partial^4 w(x,y,t)}{\partial y^4}\right) + \rho_s h_s \omega^2 w(x,y,t) = 0 \qquad \text{[2-8]}$$

$$\frac{\partial^2 u(x,y,t)}{\partial x^2} + \frac{1}{2}(1-\upsilon)\frac{\partial^2 u(x,y,t)}{\partial x^2} + \frac{1}{2}(1+\upsilon)\frac{\partial^2 v(x,y,t)}{\partial x \partial y} + \frac{\rho_S(1-\upsilon^2)}{E}\omega_s^2 u(x,y,t) = 0 \qquad \text{[2-9]}$$

$$\frac{\partial^2 v(x,y,t)}{\partial y^2} + \frac{1}{2}(1-\upsilon)\frac{\partial^2 v(x,y,t)}{\partial x^2} + \frac{1}{2}(1+\upsilon)\frac{\partial^2 u(x,y,t)}{\partial x \partial y} + \frac{\rho_S(1-\upsilon^2)}{E}\omega_s^2 v(x,y,t) = 0 \qquad \text{[2-10]}$$

$$D = \frac{E h_s^3}{12(1-\upsilon^2)} \qquad \text{[2-11]}$$

The structural elements have various boundary and coupling conditions in the real world. A creative way of illustrating a general boundary and coupling conditions is to implement spring technique [10-13]. Using of the uniformly distributed artificial springs to restrain the boundary edges and coupling edges elastically can represent the homogeneous boundary

conditions such as simply supported, clamped, free and guided [10]. The specific boundary and coupling condition can be achieved by assigning the springs with corresponding stiffness values. For example, as shown in the figure 2.1, with the aid of the spring technique, the boundary forces and moments of plate i can be expressed as the resultants of displacements w_i u_i, v_i and value K_w, k_w, k_p, and k_n, refer to the rotational spring stiffness, transverse spring stiffness, the in-plane linear spring stiffness to the edge, and in the normal direction to the edge, respectively.
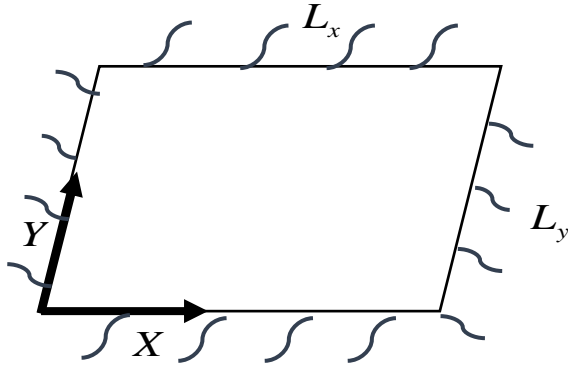
Figure 2.1 A rectangular plate i with elastic boundaries along edges

On $x_i = 0$,

$$k_{w\_x_i 0} w_i = -D\left(\frac{\partial^3 w_i}{\partial x_i^3} + (2 - \upsilon_i) \frac{\partial^3 w_i}{\partial x_i \partial y_i^2} \right),$$

$$K_{w\_x_i 0}\left(\frac{\partial w_i}{\partial x_i} \right) = -D\left(\frac{\partial^2 w_i}{\partial x_i^2} + \upsilon_i \frac{\partial^2 w_i}{\partial y_i^2} \right),$$

$$\frac{(1-\upsilon_i^2) \cdot k_{n\_x_i 0}}{E} u_i = \frac{\partial u_i}{\partial x_i} + \upsilon_i \frac{\partial v_i}{\partial y_i},$$

$$\frac{2(1+\upsilon_i) \cdot k_{p\_x_i 0}}{E} v_i = \frac{\partial u_i}{\partial y_i} + \frac{\partial v_i}{\partial x_i}$$

[2-12]

On $x_i = L_x$,

$$k_{w\_x_i1}w_i(x_i, y_i) = -D\left(\frac{\partial^3 w_i}{\partial x_i^3} + (2-\upsilon_i)\frac{\partial^3 w_i}{\partial x_i \partial y_i^2}\right),$$ [2-13]

$$K_{w\_x_i1}\left(\frac{\partial w_i}{\partial x_i}\right) = -D\left(\frac{\partial^2 w_i}{\partial x_i^2} + \upsilon_i\frac{\partial^2 w_i}{\partial y_i^2}\right),$$

$$\frac{(1-\upsilon_i^2)\cdot k_{n\_x_i1}}{E}u_i = -\left(\frac{\partial u_i}{\partial x_i} + \upsilon_i\frac{\partial v_i}{\partial y_i}\right),$$

$$\frac{2(1+\upsilon_i)\cdot k_{p\_x_i1}}{E}v_i = -\left(\frac{\partial u_i}{\partial y_i} + \frac{\partial v_i}{\partial x_i}\right)$$

On $y_i = 0$,

$$k_{w\_y_i0}w_i(x_i, y_i) = -D\left(\frac{\partial^3 w_i}{\partial y_i^3} + (2-\upsilon_i)\frac{\partial^3 w_i}{\partial x_i^2 \partial y_i}\right),$$ [2-14]

$$K_{w\_y_i0}\left(\frac{\partial w_i}{\partial y_i}\right) = D\left(\frac{\partial^2 w_i}{\partial y_i^2} + \upsilon_i\frac{\partial^2 w_i}{\partial x_i^2}\right),$$

$$\frac{(1-\upsilon_i^2)\cdot k_{n\_y_i0}}{E}u_i = \upsilon_i\frac{\partial u_i}{\partial x_i} + \frac{\partial v_i}{\partial y_i},$$

$$\frac{2(1+\upsilon_i)\cdot k_{p\_y_i0}}{E}v_i = \frac{\partial u_i}{\partial y_i} + \upsilon\frac{\partial v_i}{\partial x_i}$$

On $y_i = L_y$,

$$k_{w\_y_i1}w_i(x_i, y_i) = D\left(\frac{\partial^3 w_i}{\partial y_i^3} + (2-\upsilon_i)\frac{\partial^3 w_i}{\partial x_i^2 \partial y_i}\right),$$ [2-15]

$$K_{w\_y_i1}\left(\frac{\partial w_i}{\partial y_i}\right) = -D\left(\frac{\partial^2 w_i}{\partial y_i^2} + \upsilon_i\frac{\partial^2 w_i}{\partial x_i^2}\right),$$

$$\frac{(1-\upsilon_i^2)\cdot k_{n\_y_i1}}{E}u_i = -\left(\upsilon_i\frac{\partial u_i}{\partial x_i} + \frac{\partial v_i}{\partial y_i}\right),$$

$$\frac{2(1+\upsilon_i)\cdot k_{p\_y_i1}}{E}v_i = -\left(\frac{\partial u_i}{\partial y_i} + \upsilon\frac{\partial v_i}{\partial x_i}\right)$$

The subscripts x, y and $0,1$ denote the springs distributed along x or y axis and at the coordinate 0 or $L_x(L_y)$.

The coupling force and moments generated by the general coupling conditions at the coupling edge Γ between plate i and plate j can be determined similarly. For example, when two plates have an coupling angle $\theta = 0$, the coupling force and moment relations of plate i and j can be expressed as

$$k_{cw\_ij} w(x_\Gamma, y_\Gamma) = -Q_i(x_\Gamma, y_\Gamma) + Q_j(x_\Gamma, y_\Gamma), \qquad \text{[2-16]}$$

$$K_{c\_ij}\left(\frac{\partial w(x_\Gamma, y_\Gamma)}{\partial x_\Gamma}\right) = M_i(x_\Gamma, y_\Gamma) - M_j(x_\Gamma, y_\Gamma)$$

where k_{cw_ij} and K_{c_ij} denote the linear stiffness value in the transverse direction and torsional direction. The transverse shear force Q_i and moment M_i can be calculated by

$$Q_i = -D_i\left(\frac{\partial^3 w_i}{\partial x^3} + (2 - \upsilon_i)\frac{\partial^3 w_i}{\partial x \partial y^2}\right), \qquad \text{[2-17]}$$

$$M_i = D\left(\frac{\partial^2 w_i}{\partial x^2} + \upsilon_i \frac{\partial^2 w_i}{\partial y^2}\right)$$

When the coupling angle $\theta \neq 0$, additional force and moment terms participated in the equation equilibrium, such as the in-plane longitudinal force, shear force, and twisting moment,

The structural-acoustic interaction of a system can be determined by assembling the structural domain and acoustic domain as equation [2-18].

$$\begin{bmatrix} \mathbf{K}_S & \mathbf{C}_{SA}{}^T \\ 0 & \mathbf{K}_A \end{bmatrix}\begin{bmatrix} \mathbf{\Theta} \\ \mathbf{\Omega} \end{bmatrix} - \omega^2 \begin{bmatrix} \mathbf{M}_S & 0 \\ -\mathbf{C}_{SA} & \mathbf{M}_A \end{bmatrix}\begin{bmatrix} \mathbf{\Theta} \\ \mathbf{\Omega} \end{bmatrix} = \begin{Bmatrix} \mathbf{F} \\ \mathbf{P} \end{Bmatrix} \qquad \text{[2-18]}$$

where subscripts S and A denote that the variables are related to the structure and cavity respectively. $\mathbf{M}$ and $\mathbf{K}$ are the generalized global mass and stiffness matrices. $\mathbf{F}$ denotes the external loading vector originated by the point force. $\mathbf{C}_{SA}$ is the global structure-acoustic coupling matrix.

Three methods are usually employed to solve the equation [2-18], namely modal-coupling method [14], wave-based method [15], and Rayleigh-Ritz method [12]. Modal coupling approach considers acoustic and structural problem independently. The structural modes in vacuo and acoustic cavity modes with rigid walls need to be determined a priori [16-22]. The two sets of modes are then combined via spatial coupling coefficients, to determine the response of the coupled system. This method is suitable for weak coupling between structural and acoustic cavity because the particle velocity at the surface of rigid walls is zero. Apply wave-based method is another way of solving the vibro-acoustic problem [15][23-26]. It is based on the Trefftz method [27] and approximates the field variables by an expansion of wave function to satisfy the boundary condition. However, as the boundary and continuity condition errors are forced to zero due to the integral, it applies the same rigid boundary

assumption as the modal interaction approach and therefore has a similar limitation when dealing with strong coupling between structural and acoustic domain. The third approach solves the vibro-acoustic problem based on the energy equilibrium framework using Rayleigh-Ritz procedure[12-14] [20][28-29]. The Rayleigh method [30] works by the principle that the energy of a vibrating system interchange between the potential and kinetic form without dissipation at every natural mode. By using a set of admissible trial function for the mode shapes and assuming simple harmonic motion, the equalisation of maximum potential energy and the maximum kinetic energy yields the dynamic quantities. Ritz [31] generalised the Rayleigh method by assuming a set of admissible trial functions, each having independent amplitude coefficients. The approximations for the frequency can be achieved by minimising the energy functional with respect to each of the coefficients. Ritz demonstrated this method on a square plate under free boundary condition for which has no exact solution.

2.2 Numerical method - Finite Element Analysis (FEA) for the structural domain

The finite element analysis (FEA) [32-33] is a general framework for solving numerically integral and differential equations, particularly partial differential equations (PDEs). The ordinary low-frequency dynamic analysis is solved by the FEA that is well established, referenced in the literature and has a long tradition[34-35]. However, the FEA has not been extensively used for solving acoustic problem in the offshore platform. This technique requires the discretisation of the volumes. The number of finite elements increases with frequency to describe the short wavelength behaviour at increasing frequencies. A usual rule of thumb is that six linear finite elements per wave length are enough to obtain accurate results [36]. The wave length can be calculated as the length of a wave propagating in an unbounded medium or the wave length of the nearest eigenfrequency. Using this criterion, the computational costs soon become unaffordable. The large size of the models and expense in computation resources often limit the accurate prediction to relatively low frequencies, especially if full 3D modeling is used [37]. An advantage of this methods is that all details of interest in the structure can be described and included in the model, and at the same time the finiteness of the real structure is taken into account. Therefore, in the real practice, FEA is a common technique to evaluate the structural integrity [38-44] for the offshore structures, typically below 100 Hz. Through performing vibration analysis in the design stage, risk of resonance and severer vibration can be avoided, consequently reduces the structure-borne noise radiation throughout the offshore platform. This analysis is particular important for the major equipment. For instance, as a component of a rotary drilling rig, draw-works is primary

hoisting machinery. The periodic residual unbalance force of the rotary drum can be the major excitation source that causes the drill floor vibration. To perform the influences of operating draw-work on the drill floor structures, an FE model is built with Hyperwork software which extends 14 meters in elevation of the drill floor, with the distribution of all equipment masses to the exact location as shown in figure 2.2.

Considering +/- 20% margin from the draw-work excitation frequency of 5.33Hz, as shown in figure 2.3, the first stage modal analysis scanned six modes that fall into the interest frequency range of 4.3Hz to 6.4 Hz. These modes may cause resonance on the drill floor structures. Therefore, frequency response analysis is needed to determine the actual response of the affected area and identify whether the structures can sustain under the periodic loading when operating.
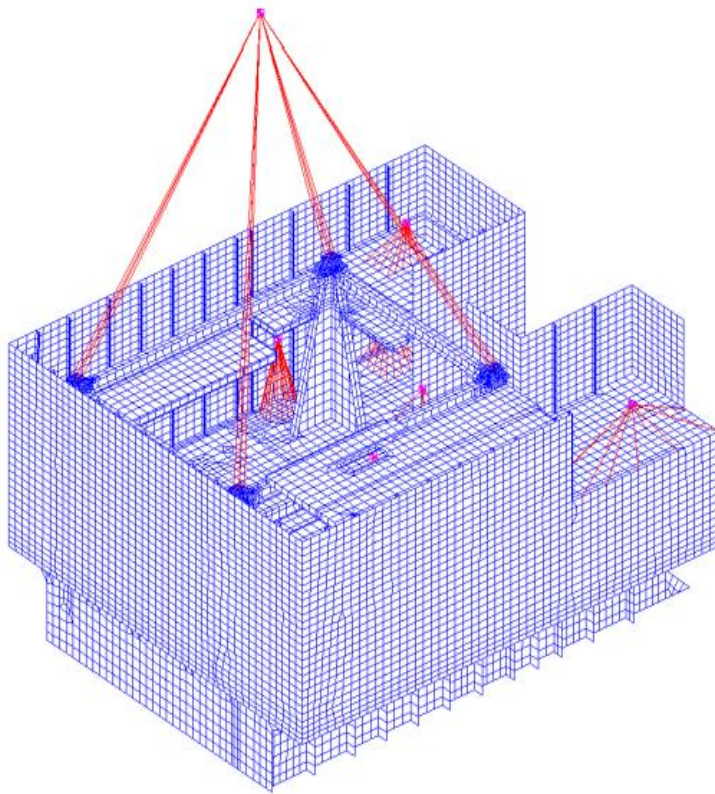
Figure 2.2 Drill floor FE model
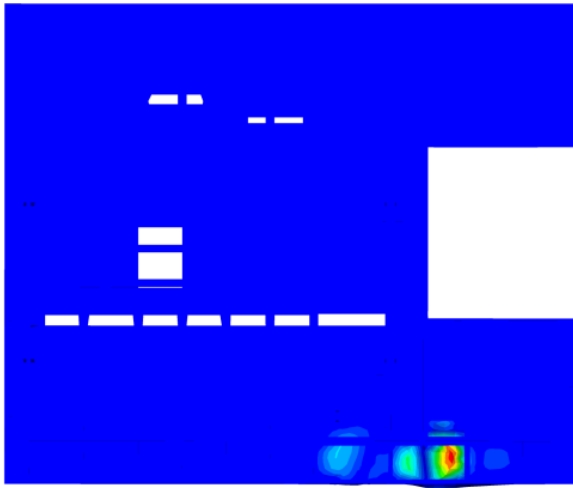
(a) Mode 6 at 4.34 Hz,
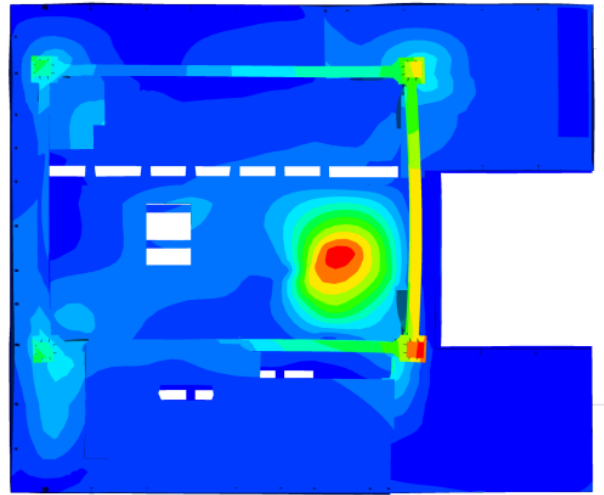
(b) Mode 7 at 5.1Hz,
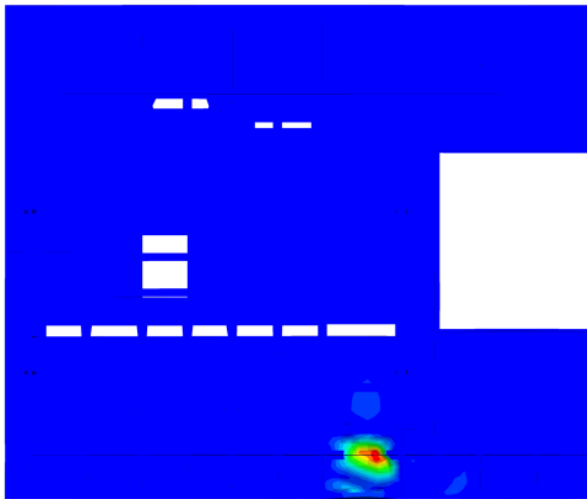
(c) Mode 8 at 5.69 Hz
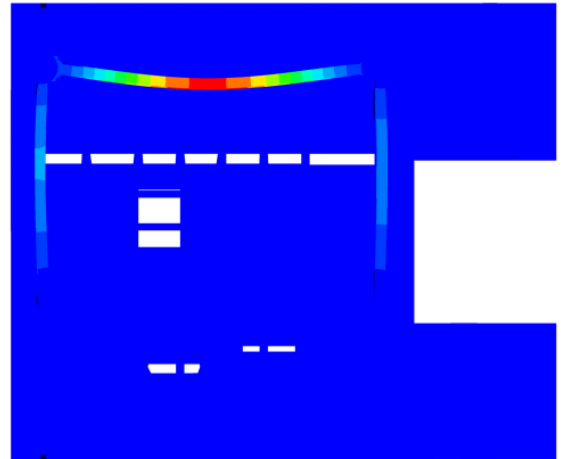
(e) Mode 10 at 6.05 Hz
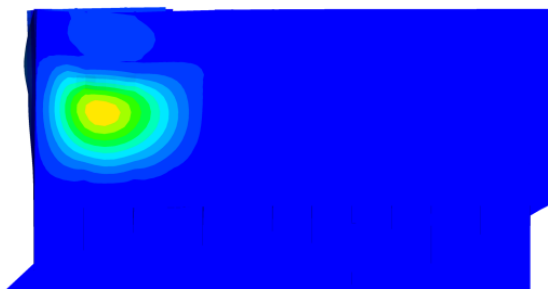
(d) Mode 9 at 5.92 Hz
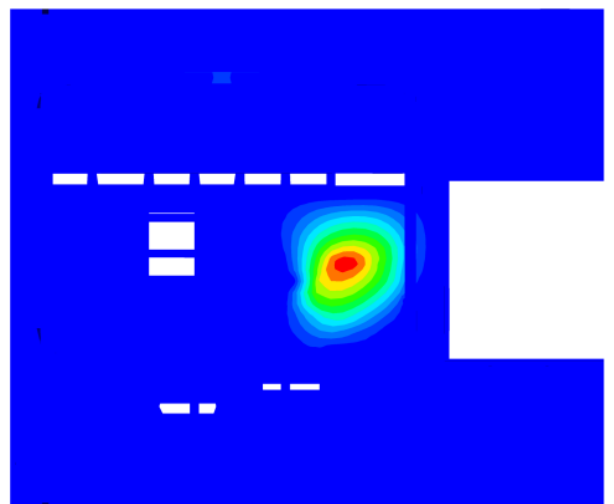
(f) Mode 11 at 6.21 Hz

Figure 2.3 Six modes close to the excitation frequency obtained by normal mode analysis

The maximum velocity amplitude is determined in the frequency response analysis and compared with the criteria set out in the ISO 10816-3. The maximum velocities in associated with an array of nodes in different frequencies are tabulated in Table 2.1 for the horizontal and vertical directions. According to the results, the maximum RMS velocity is 1.43mm/s occurs at local instrument room, and it is smaller than 4.5 mm/s shown in the vibration limit. Thus, the vibration of the drill floor is satisfied with the ISO 108816-3 category B (unrestricted long term operation).

This example illustrated the using of FEA in solving structure dynamic for an offshore platform; it also illustrates the vibration energy can be efficiently transmitted from a source to surrounding structures. Both transverse vibrations and in-plane vibrations are observed in the analysis. In fact, based on the measurements done by Kihlman and Plunt [45-46], vibration velocity levels in the normal and parallel direction of the shell can be the same magnitude in the steel made ship structure. If the in-plane motion of the shell is caused by longitudinal waves traveling the vertical direction, these waves would determine the velocity level perpendicular to the deck plating. On the other hand, if the in-plane motion is determined by transverse waves induced by the relative vertical motion between the frames, then the transverse waves would be of the greatest importance [47]. It can be concluded that all wave types transform at the junctions and participate in vibration energy transmission, although transverse wave is the only type to be considered for interaction with the acoustic domain at the receiving end of the transmission line [48]. Thus, this explains the reason that the structural coupling effects should be considered when handling the offshore platform vibro-acoustics.

Drill Floor Vibration Velocity Amplitude for Horizontal Axis

Location	Occur Node	Horizontal Velocity (mm/s)		Criteria (mm/s RMS)	Ratio
		Zero-Peak	RMS	ISO 10816-3	
Driller Control Room (DCR)	7	0.63	0.45	4.50	9.9%
Local Instrument Room (LIR)	12	2.02	1.43	4.50	31.7%
Drawworks	5	0.20	0.14	4.50	3.2%
Under Drill Floor Structure	28776	0.25	0.18	4.50	4.0%
Drill Floor (EL 31320 ABL)	30549	0.23	0.16	4.50	3.6%
EL 35520 ABL Platform	28069	0.63	0.44	4.50	9.8%
EL 36910 ABL Platform	17820	0.11	0.07	4.50	1.7%
EL 39170 ABL Platform	17526	0.26	0.18	4.50	4.1%
Derrick Foundation	15434	0.81	0.57	4.50	12.7%
Wind Wall	28224	1.50	1.06	4.50	23.5%

Drill Floor Vibration Velocity Amplitude for Vertical Axis

Location	Occur Node	Vertical Velocity (mm/s)		Criteria (mm/s RMS)	Ratio
		Zero-Peak	RMS	ISO 10816-3	
Driller Control Room (DCR)	7	0.13	0.09	4.50	2.0%
Local Instrument Room (LIR)	12	0.27	0.19	4.50	4.3%
Drawworks	5	0.06	0.04	4.50	0.9%
Under Drill Floor Structure	28489	0.47	0.33	4.50	7.4%
Drill Floor (EL 31320 ABL)	18872	0.89	0.63	4.50	13.9%
EL 35520 ABL Platform	27208	0.66	0.47	4.50	10.4%
EL 36910 ABL Platform	29707	0.05	0.04	4.50	0.8%
EL 39170 ABL Platform	18800	0.58	0.41	4.50	9.1%
Derrick Foundation	14656	0.42	0.30	4.50	6.7%
Wind Wall	27333	0.60	0.42	4.50	9.4%

Table 2.1 Forced vibration analysis calculated maximum velocity amplitude in horizontal and vertical axis

2.3 Statistical method – Statistical Energy Analysis (SEA) for vibro-acoustics

The following published paper is used for the contents of this section

[60] X. Ji and C. Chin, "Analysis of acoustic models and statistical energy analysis with direct field for machinery room on offshore platform," Acta Acustica united with Acustica, vol. 101, no. 6, pp.1234-1244, 2015. DOI: 10.3813/AAA.918916

Due to the shortcomings while using FEA at low frequencies, statistical methods such as Statistical Energy Analysis (SEA) are developed to calculate the response of the systems using statistical modal parameters. Consequently, a large structure is divided into subsystems which are expressed using statistical modal parameters. The responses of the system are calculated in terms of total time-average distribution of energy among subsystems instead of exact displacements or

forces. The average response of subsystems using SEA can be more reliable than the FEA since it removes small variation effects in the high frequencies. Since the development of SEA by Lyon [49] and Smith [50], it has been widely and successfully applied to modeling the vibro-acoustics within closed domains such as buildings, aerospace, naval and automobile industries [51-58].

SEA approach is based on the assumptions of a large population of modes, wide-band and uncorrelated excitations, large modal overlap, diffuse field, equipartition of energy, and weak coupling [59]. The main idea is that a complex built-up structure can be divided into subsystems, characterised by their modal densities and internal loss factors. The statistical mode densities for each subsystem and the coupling loss factors (CLFs) control the power fluxes among subsystems. Therefore, there is a lower limit on the solving frequencies when applying the SEA technique. Due to these assumptions, lower frequency limit applies for SEA approach, and spatial averaged response in each subsystem is obtained.

The SEA formulation is based on the power balances of the subsystems. With the power input to the system, a set of equations can be derived such that the only unknowns of the problem are their averaged energies. For a particular subsystem i, this balance is expressed as

$$\Pi_i^{in} = \Pi_i^{diss} + \sum_{\substack{j=1 \\ i \neq j}}^{n} \Pi_{ij} \,, i = 1, \mathrm{K}\,, n, \qquad [2\text{-}19]$$

where Π_i^{in} is the external power entering the subsystem, Π_i^{diss} is the power dissipated in the subsystem and Π_{ij} is the power exchanged between the subsystem i and j. For the particular case of 2 subsystems, an illustrative sketch is shown in figure 2.4. The power dissipated by subsystem i is

$$\Pi_i^{diss} = \omega \eta_{ii} \langle E_i \rangle, i = 1, \mathrm{K}\,, n, \qquad [2\text{-}20]$$

where ω is the angular frequency, η_{ii} and E_i are the internal loss factor and the averaged energy of subsystem i respectively.

The key aspect of the SEA formulation is the assumption that the power Π_{ij} exchanged between subsystems i and j can be expressed in terms of their averaged energies as

$$\Pi_{ij} = \omega\left(\eta_{ij}\langle E_i \rangle - \eta_{ji}\langle E_j \rangle\right) \qquad \text{[2-21]}$$

Using the coupling loss factors η_{ij} and η_{ji}. These factors are assumed to satisfy the consistency relationship

$$\eta_{ij}n_i = \eta_{ji}n_j \qquad \text{[2-22]}$$

where n_i and n_j are the modal density of subsystem i and j. Therefore, for each subsystem, the power balance of equation [2-21] can be rewritten regarding energies of the subsystems as

$$\Pi_i^{in} = \omega\eta_{ii}\langle E_i \rangle + \omega\sum_{\substack{j=1 \\ i \neq j}}^{n}\left(\eta_{ij}\langle E_i \rangle - \eta_{ji}\langle E_j \rangle\right), i = 1, K, n, \qquad \text{[2-23]}$$
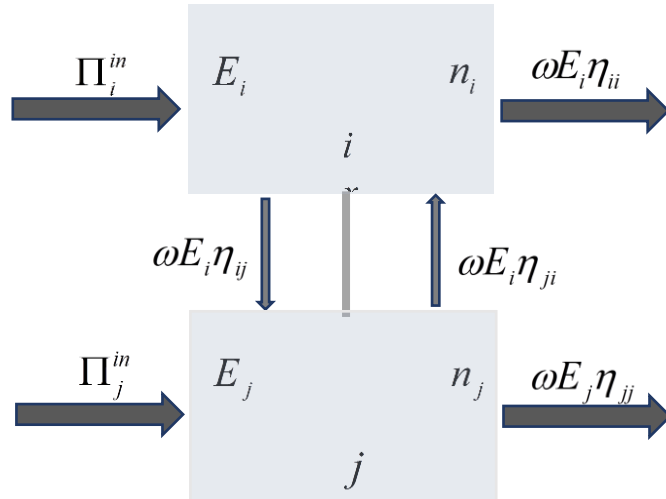
Figure 2.4 A two subsystem SEA model [60]

Solving high frequencies vibro-acoustic problems with the SEA is particularly attractive for the low computational cost. However, its application to real-life systems has severe limitations. The assumption of diffuse field cannot be satisfied if space is treated with highly absorbent materials which reduce the energy from reflections, or space is highly influenced by the direct field component. The SEA requires that the number of modes shall be large enough in a frequency band of interest. For instance, a conservative lower limit for offshore platform is at 125 Hz. Also, SEA can only give the estimate of system responses in an average value and do not predict the distribution of the energy field.

17

Additional procedures are needed to incorporate to obtain the local response. Maxit and Guyader [61] incorporated the modal energy distribution in the SEA formulation to remove the assumption of equipartition of modal energies. They calculate the modal information of subsystems for complex structures using the FEA to get the detail of energy distribution. In this thesis, since estimating the sound level in the compartments is a major concern, SEA-DF method is implemented in the source dominated spaces to obtain the localised sound level in the room. By separating the direct field component from the total energy, we can both comply with the approach assumption and collect the localised sound level values. In this case, the reverberation energy flows in the each subspace are illustrated in the figure 2.5. At steady-state condition, the basic equation [62] for expressing the energy flow relation between the subsystem i and other subsystems j in the SEA model is determined.
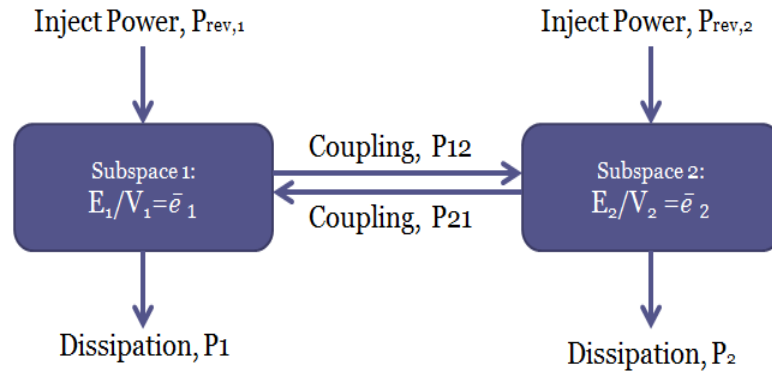
Figure 2.5 Reverberation energy flow between two subspaces **[60]**

The reverberant modal energy in subsystem i, E_i obtained from SEA is then applied to compute the reverberant sound pressure level of an acoustical system

$$L_{p,rev} = 10 \log \frac{\rho_i c_0^2 E_i}{V_i p_{ref}^2} \tag{2-24}$$

The sound field of a direct field dominated room is, therefore, the additive of the reverberant field sound level $L_{p,rev}$ and the direct field sound level $L_{p,rev}$ as

$$L_{p,total} = 10 \log\left(10^{0.1 L_{p,rev}} + 10^{0.1 L_{p,dir}}\right) \tag{2-25}$$

The direct field of equipment can be modelled according to the geometries feature. Three types apply to the equipment onboard [63]: a point source exhibits inverse square $(1/r^2)$ attenuation

18

and can be applied to most small to medium-sized equipment like pumps, compressors, and purifiers; line source demonstrates approximately cylindrical ($1/r$) spreading and adequate for more linear sources like heating, ventilation, and air conditioning duct; lastly, rectangular surface source generates box-like shaped contours for large machinery such as diesel engine, mud pumps and hydraulic power units (HPU).

Due to the dependence on statistical representations of modal properties, the accuracy of SEA relies on the condition that there are a sufficient number of modes within the frequency band of interest. To offshore platforms, this criterion can comply when analysed frequencies above 125 Hz and set the interest bandwidth of octave band. Below this frequency limit where the number of modes in the frequency band of interest is small, the using of average modal density is no more feasible.

2.4 Empirical methods for solving machinery room interior acoustic

The following published paper is used for the contents of this section

[60] X. Ji and C. Chin, "Analysis of acoustic models and statistical energy analysis with direct field for machinery room on offshore platform," *Acta Acustica united with Acustica,* vol. 101, no. 6, pp.1234-1244, 2015. DOI: 10.3813/AAA.918916

Sabine law [64] is the classical room acoustic theory to compute the room sound level. However, it is not suitable to be used in the offshore platform environment due to the precondition of diffuse field theory that requires the sound to be reflected from the enclosure surfaces with equal levels of sound intensity. In fact, this precondition often unable to comply due to the presence of multiple fittings, non-uniform absorption and reflection distribution, and the irregular room shape. Formulas based on curve-fits to experimental data have been used to estimate sound pressure levels in industrial rooms containing noise-producing machinery, including Thompson model [65], Kuttruff model [9], SNAME model [66], Heerema and Hodgson model [67] and Sergeyev model [68]. While such empirical formulas can be accurate and easily applied, they are often limited in their scope of applicability and do not provide the analyst with any physical insight into the specific problem at hand. Due to the similarity of the Type 1machinery rooms and the land based industry rooms, it is worth to evaluate the validity of these empirical formulas for offshore platform machinery rooms' sound level approximation.

L1: Thompson model [65] made a modification to Sabine model based on experimental observation. The Sabine model only considers reverberant and not direct sound. Thompsom model considers several factors such as temperature, barometric pressure, and source directivity within the room. Based on a linear decay phenomenon, it includes the room mean free path, MPF. It also accounts for empty irregularly proportioned factories according to volume V and surface area S. The reverberant field sound pressure level is proposed to be a function of MPF, room mean absorption coefficient $\bar{\alpha}$, source/receiver distance r, and air attenuation m in the space, and sound power level L_w. The effect of room temperature TM and barometric pressure BP are included in the sound pressure level (SPL) as shown:

$$L_p = L_w + 10\log\left[\frac{\exp(-mr)}{4\pi r^2} + \frac{4MFP}{r(\bar{\alpha}S + 4mV)}\right] + 10\log\left(\frac{TM + 460}{527} + \frac{30}{BP}\right) \qquad [2\text{-}26]$$

The value of air attenuation used is presented as shown in Table 2-1.

	Octave Band					
	125	250	500	1000	2000	4000
m	0	0.001	0.003	0.007	0.013	0.023

Table 2.2 Value of the air attenuation m **[65]**

L2: Kuttruff [9] proposed a model for large flat factories containing sound scattering obstacles. The model assumed that the floor was diffusely reflected and its absorption coefficients considered the effect of the fittings on the sound propagation. The absorption effects from side walls are neglected due to the room height is smaller than the lateral dimensions, and the sound reflections from the ceiling were predominant. Thus the sound pressure level is computed as follows:

$$L_p = L_w + 10\log[A(r, H, \bar{\alpha})] \qquad [2\text{-}27]$$

where
$$A(r, H, \bar{\alpha}) = \frac{1}{4\pi r^2 + (1-\bar{\alpha})}\left[\frac{(1 + r^2/H^2)^{-3/2} + b(1-\bar{\alpha})(b^2 + r^2/H^2)^{-3/2}/\bar{\alpha}}{\pi H^2}\right] \qquad [2\text{-}28]$$

Here H is the room height, constant b depends on the average absorption coefficient of the floor and ceiling $\bar{\alpha}$. Here the corresponding values used are shown in table 2.3.

Average absorption coefficient α	Constant b
0.7	1.806
0.6	1.84
0.5	1.903
0.4	2.002
0.3	2.154
0.2	2.425
0.1	3.052

Table 2.3 Value of constant b [9] used in Kuttruff model [9]

L3: SNAME method [66] is often recommended by merchant ship owners to predict the airborne noise using codified methods [69]. SNAME method calculates the sound pressure level of the machinery room airborne noise by solving the direct field and reverberant field independently. The direct field and reverberant field were expressed in the unit of ft. Note that equation [2-33] is used when the source or receiver distance exceeds ten ft.

$$L_{p,dir} = L_w - 20\log_{10} r + 10\log_{10} Q - 1 \qquad [2\text{-}29]$$

$$L_{p,rev} = L_w - 10\log_{10} R_T + 16 \qquad [2\text{-}30]$$

$$L_{p,rev} = L_w - 30\log_{10} r + 10\log_{10} Q + 9 \qquad [2\text{-}31]$$

where L_w is the total sound power level in each octave band due to all noise sources in the compartment. $L_{p,dir}$ and $L_{p,rev}$ are the total octave band sound pressure level in the diffuse field and direct field respectively. Q is the directivity factor and equal to 2, 4, eight depending on the source location in the room. R_T is the room constant which is based on diffuse field theory with a series of corrections including correction for non-boundary surfaces, correction for low frequencies, and correction for large space.

Additionally, SNAME method provides empirical adjustments for merchant ship environment. For example, absorption by both room boundaries and the surface of room contents are considered. For the different room, the soft surface and hard surface of room contents are

represented by the empirical percentage of total room surface area, and room constant with room contents are calculated according.

$$R_{non-boundary} = S_H \alpha_H + S_S \alpha_S \qquad [2\text{-}32]$$

where S_H and S_S are the total hard and soft non-boundary areas which can be calculated by multiplying the total boundary area with area correction factor α_H and α_S in table 2.4. Also, the sound attenuation in the air and sound pressure level at low frequencies are compensated by employing minimum room constant value α_{min}. The empirical absorption coefficients for hard surfaces α_H and soft surfaces α_S and minimum room constant R_{min} are tabulated in table 2.5.

Non-boundary Surface Area Correction Factor	Hard	Soft
Lounge, Washroom, Officer's mess	0	0.1
Crew's mess, Office	0.2	0
Berthing	0	0.2
Main Engine Room	0.5	0.2
Auxiliary Machinery Room	0.4	0.2
Secondary Auxiliary Machinery Room	0.3	0.1

Table 2.4 Non-boundary surface area correction factor for SNAME model [66]

	Octave Band								
	31.5	63	125	250	500	1000	2000	4000	8000
αH	0.10	0.10	0.09	0.05	0.02	0.01	0.01	0.01	0.01
αS	0.10	0.25	0.25	0.40	0.60	0.70	0.70	0.60	0.50
Rmin	654	164	41	10	2	0	0	0	0

Table 2.5 Absorption coefficient for 'Hard' and 'Soft' surfaces and minimum room constant for SNAME model [66]

L4: Heerema and Hodgson [67] developed the empirical model for industrial workrooms in a frequency range of 125 Hz to 4000 Hz using a linear regression analysis of measurement data in 30 industrial workrooms with concrete and brickwork construction, acoustically treated and some other surface type (e.g. drywall, roll-away doors, glazing) and horizontally uniformly distributed fittings [70]. These industrial workrooms are divided into three classes which are assigned with consistent class absorption coefficients between typical industrial workrooms. The frequency

dependent sound pressure level followed a relationship of a slope term s, intercept term I, and source/receiver distance r. Here s and I are calculated based on the given empirical coefficients.

$$L_p = L_w + I + s10\log r \qquad [2\text{-}33]$$

The interception I is calculated according to:

$$I = C_{i0} + C_{i1}\alpha_{eff} + C_{i2}H + C_{i3}\lg(H) + C_{i4}F + C_{i5}\frac{h}{H} + C_{i6}\frac{s}{V} + C_{i7}V + \qquad [2\text{-}34]$$
$$C_{i8}S + C_{i9}\alpha_{eff}LW$$

where the parameters S, V, L, W, H are the room surface area, volume, length, width and height respectively, h is the average fitting height in the room, coefficient C_{i0} to C_{i9} are presented in Table 2.6. The effective absorption coefficient is assumed using the fitting density F and coefficient $C_{\alpha0}$ and $C_{\alpha1}$ presented in table 2.6.

$$\alpha_{eff} = C_{\alpha0} + C_{\alpha1}F \qquad [2\text{-}35]$$

Fitting density was developed by Kuttruff [9]

$$F = \frac{S_f}{4V} \qquad [2\text{-}36]$$

where S_f is the total surface area of the fittings exposed to the sound field. The slope s of the sound-propagation curve used in equation [2-33] is written as:

$$s = C_{s0} + C_{s1}\overline{\alpha} + C_{s2}H + C_{s3}\lg(H) + C_{s4}\frac{1}{F} + C_{s5}\frac{h}{H} + C_{s6}\frac{s}{V} \qquad [2\text{-}37]$$

The parameters C_{s0} to C_{s6} are presented in table 2.6.

L5: Sergeyev [68] developed a sound pressure model based on Bessel function. It applies to parallelepiped rooms with width W, height H of common construction with furnishings and surface area S. The noise sources are considered to be hemispherical radiating. The absorption coefficient $\overline{\alpha}$, in the reverberant field, is determined for a factory making textile and metal.

$$L_p = L_w + 10\log\left[\frac{1}{2\pi r^2} + \frac{(1-\overline{\alpha})(r+W)J(\overline{\alpha},\rho)}{HW(r+H)}\right] \qquad [2\text{-}38]$$

where is the source/receiver distance and Bessel function is written as:

$$J(\bar{\alpha},\rho)=\frac{0.1}{\bar{\alpha}+\rho^2\,\exp[0.65\rho]}$$

<div align="right">[2-39]</div>

in which

$$\rho=-rS\,\ln(1-\bar{\alpha})/4V$$

<div align="right">[2-40]</div>

Parameter	Octave Band					
	125	250	500	1000	2000	4000
$C_{i0}=$	21.4	25.5	27.9	41.1	29	65.9
$C_{i1}=$	-6.32	-2.96	19.4	-16.5	-18.2	-18.3
$C_{i2}=$	5.84	6.58	6.46	8.61	5.59	9.74
$C_{i3}=$	-86.7	-98	-99.8	-127	-85.5	-155
$C_{i4}=$	0	0	-121	48.3	72.2	37.1
$C_{i5}=$	5.03	5	5.13	12.4	0	0
$C_{i6}=$	0	0	0	-9.04	-10.1	-21.4
$C_{i7}=$	-8.33×10^{-5}	-6.25×10^{-5}	5.64×10^{-5}	-1.34×10^{-4}	0	0
$C_{i8}=$	0	0	0	0	-4.87×10^{-4}	-8.40×10^{-4}
$C_{i9}=$	3.10×10^{-3}	2.50×10^{-3}	1.14×10^{-3}	1.82×10^{-3}	0	2.47×10^{-3}
$C_{s0}=$	-91.9	-102	-87.7	-81.9	-60.5	-70.8
$C_{s1}=$	-16.1	-21.9	-29.9	-26.9	-24.9	-19.2
$C_{s2}=$	-12.1	-14.3	-12.5	-12.5	-8.5	-9.2
$C_{s3}=$	196	225	194	187	128	146
$C_{s4}=$	-0.037	-0.028	-0.007	0.032	0.131	0.135
$C_{s5}=$	-5.08	-3.63	-2.33	-9.79	-11.6	-11.88
$C_{s6}=$	15	18.8	17.7	18	15.9	13.2
$C_{\alpha0}=$	0.11	0.017	0.099	0.131	0.14	0.135
$C_{\alpha1}=$	4.52	5.8	4.32	2.79	2.28	1.94

Table 2.6 Coefficients used in Heerema and Hodgson model [67]

2.5 Artificial neural network method (ANN)

The above-mentioned methods are considered as the classical method of determining the room noise levels. These methods require a large number of accurate input parameters to compute accurate results. However, these parameters may be difficult to obtain in the early design stage of an offshore platform. It is therefore desired to have a revolution method that can predict the broadband noise level with good accuracy for the offshore platform in the early design stage. Concerning the common features of the offshore platform from one to another, it will be ideal if compartment noise level can be predicted base on the information collected from previous

projects. It can be realised if the artificial neural network (ANN) is used as the noise prediction tool.

ANN is a learning algorithm that is inspired by the structure and functional aspects of biological neural networks. Computations are structured in terms of an interconnected group of artificial neurons, processing information using a connectionist approach to computation [71]. The ANN modeling consists of several steps including collecting training data, preprocessing the collected data, choosing a learning paradigm, selecting an ANN structure, determining the ANN parameters, training the ANN, and analysing the training errors. The design steps are iterated until the user is satisfied. This method is known to be quite accurate to model various phenomena and has good ability to determine the complex relations among many variables. It is a suitable tool for analysing physical phenomena such as sound in which adequate data related to many variables are complex and not easy to understand [72]. With ANN's impressive capability in dealing with severe non-linearity and uncertainty of a system, the application of ANN method had become quite intensive. ANN has been used for a variety of purposes in acoustics field, including traffic noise prediction[72-73], workroom noise prediction [74], product noise analysis [75], vehicle interior noise prediction [76] and outdoor sound transmission loss analysis [77].

Chapter 3. Analysis of Acoustic Models and Statistical Energy Analysis with Direct Field for Offshore Platform Compartments

3.1. Introduction

The compartment boundaries in the offshore platform are usually covered by various types of fire and thermal insulation which made of mineral wool with excellent sound absorptive capability. When different insulations are used in the compartment, non-uniform absorption distribution problem can arise. In this case, the diffuse field assumption based classical Sabine law [64] is not appropriate.

The offshore platform machinery rooms can be classified into two types [60] when performing noise calculation.

- Type 1 machinery room – The room contains a high level of the noise source. The airborne noise is approximately equal to the total noise level so that the structure-borne transmission can be negligible. Examples of this type in the offshore platform are the engine room and mud pump room.
- Type 2 machinery room – The room is located adjacent or far away from the Type 1 room in which the interior noise source is lower or comparable with the structure-borne noise radiation. Under such condition, both structure-borne and airborne noises need to be considered. Examples of this type in the offshore platform are the pump room and air handling unit (AHU) room.

The airborne dominated Type 1 room is quite similar to the land-based industrial rooms and can be approximated by the land-based industrial room method whereas the Type 2 machinery room influenced by both structure-borne and borne noise is unique. In this chapter, suitable prediction techniques are identified for the two types of machinery spaces, workspaces, and living spaces of the offshore platform. The five empirical acoustic models reviewed in the section 1.2.4 and Statistical Energy Analysis (SEA) with direct field (DF) method are evaluated in the offshore platform machinery rooms. The calculation results of empirical models and SEA-DF are compared and validated by experimental measurements in an engine room and a pump room. Through performing the noise analysis for the jack-up rig, the characteristic of structure-borne noise in the machinery spaces, working spaces, and living spaces are understood. The noise control strategy such as implementing acoustic insulation and damping treatment is investigated

27

by using the SEA. The SEA-DF approach is then applied to predict the noise level throughout the offshore platform. The prediction results are collected and serve as the sample data for the neural network modeling in the next stage

3.2.   Publications

The following section 2.3 and 2.4 used the materials from the following papers published during the period of PhD.

[60] X. Ji and C. Chin, "Analysis of acoustic models and statistical energy analysis with direct field for machinery room on offshore platform," Acta Acustica united with Acustica, vol. 101, no. 6, pp.1234-1244, 2015. DOI: 10.3813/AAA.918916

[78] X. Ji , C. Chin and E. Mesbahi, "The effect of damping treatment for noise control on offshore platforms using statistical energy analysis," in 17th International Conference on Noise and Vibration Engineering, Amsterdam, 2015.

3.3.   Analysis of Empirical formula, Statistical Energy Analysis with Direct Field (SEA-DF) for Machinery Spaces

The experimental measurements were conducted in an engine room on the upper hull and a pump room in the column of a semi-submersible. The measurements were taken by a Type 1 integrated sound level meter. Each sample is measured for approximately 15 seconds to achieve a steady-state reading. The vibration spectrums are measured using the accelerometer in the horizontal, vertical and axial direction. The average acceleration was recorded. The sound power level for each noise source was determined using ISO3744 engineering method with sound pressure levels of the source was taken by the vendor during factory acceptance test (FAT) at 100% nominal load and speed. All the relevant sources information are tabulated in table 3.1

Space	Source Type	Equipment	Octave Band Frequency					
			125	250	500	1000	2000	4000
Engine Room	Sound Power Level (dB)	Engine 1	118	118	119	119	115	115
		Engine 2	118	118	119	119	115	115
		Turbocharger 1	102	104	106	111	116	123
		Turbocharger 2	102	104	106	111	116	123
Pump Room	Sound Power Level (dB)	Cooling Pump 1	92	92	91	89	87	84
		Cooling Pump 2	92	92	91	89	87	84
		Ballast Pump	91	91	90	88	86	83
		Bilge Pump	89	89	88	86	84	81
	Acceleration (m/s²)	Cooling Pump 1	0.84	0.51	0.63	0.94	1.63	2.51
		Cooling Pump 2	0.84	0.51	0.63	0.94	1.63	2.51
		Ballast Pump	0.81	0.44	0.65	0.94	1.66	2.52
		Bilge Pump	0.72	0.36	0.63	0.13	0.63	1.26

Table 3.1 Source information for engine (Type 1) and pump room (Type 2) **[60]**

The involved engine room has a dimension of 15 (L) x 14 (W) x 6.5 (H). The overhead deck is covered by A60 plus thermal insulation (Searox SL640, Marine Firebatts 130, 1x40 mm); Port, Starboard and aft bulkheads are covered by A60 insulation (Searox SL640, Marine Firebatts 130). The forward bulkhead and deck are made of bare steels. Two generator sets located at the room centre are surrounded by other equipment. During the experiment, the two engines were operating at 100% load. There are other noise sources operating, however, comparing their sound power levels provided by the vendors, engine mechanical noise and turbocharger air inlet noise are two dominant contributors and thus other noise contributors are neglected. Four measurement locations are marked as shown in figure 3.1. The measurements were taken at 1.5m above the raised floor which is 3.3 m above bottom deck. On the other hand, pump room dimension is approximately 6.75 (L) $\times$ 6 (W) $\times$ 4 (H). The overhead deck and all four bulkheads are covered by acoustic insulation (SEAROX SL340, MARINE SLAB 80). Four pumps at 100% working load are the main noise sources in the room. Four measurement locations that are 1.5 m above bottom deck and marked in figure 3.2. The measurements taken in engine room (see figure 3.3) and pump room (see figure 3.4) will be compared with the results of empirical acoustic models and SEA-DF method. The accuracy of each method is verified by comparing the relative errors (RE) between the prediction results and measured sound pressure level.
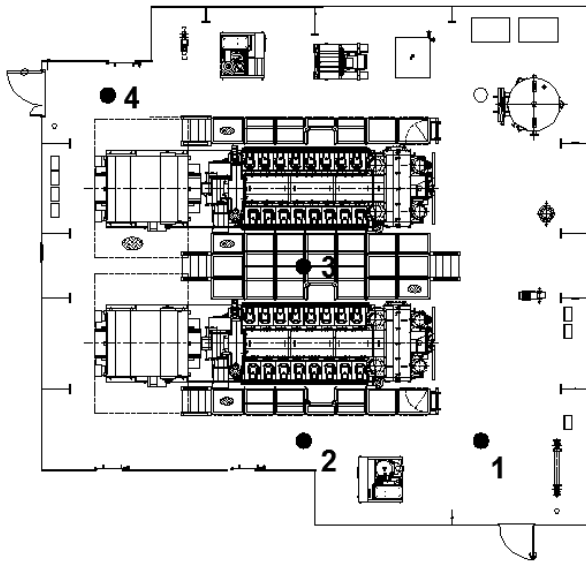
Figure 3.1 Engine room layout showing 4 locations (Type 1) **[60]**
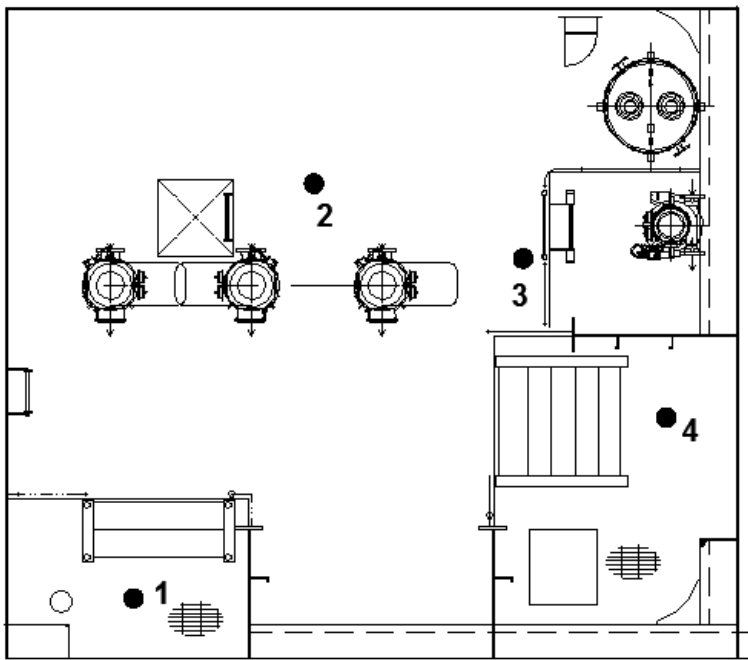
Figure 3.2 Pump room layout showing 4 locations (Type 2) **[60]**
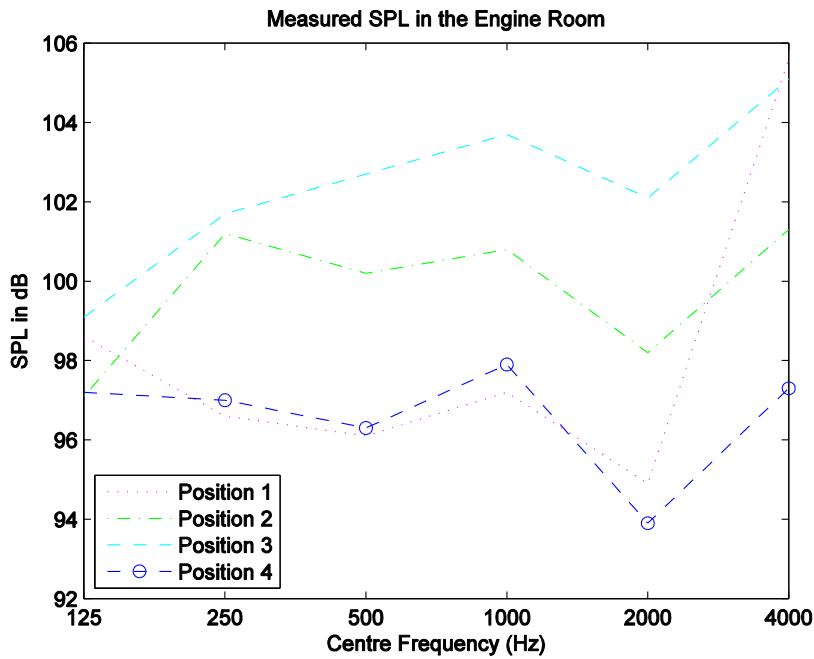
Figure 3.3 Experimental results of SPL for engine room (Type 1) **[60]**
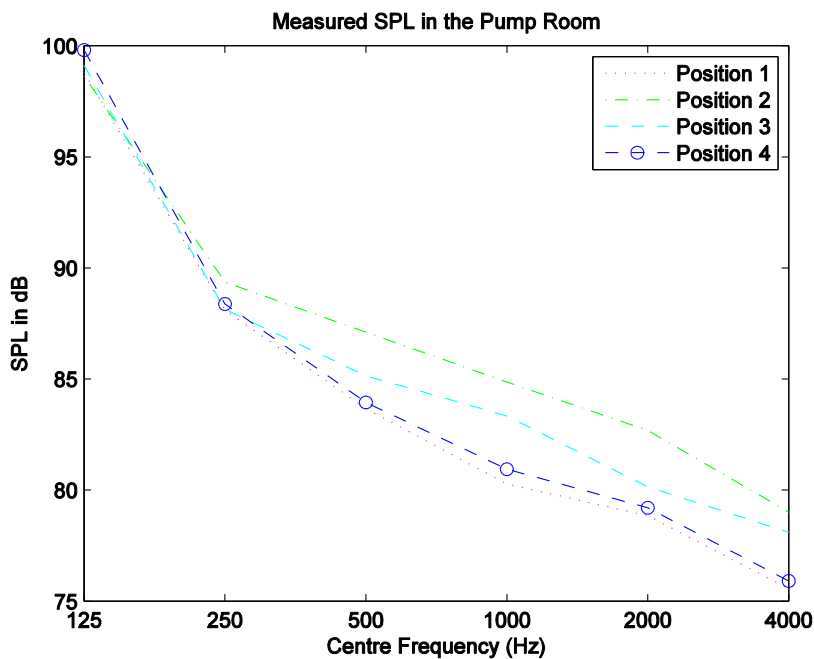
Figure 3.4 Experimental results of SPL for engine room (Type 2) **[60]**

3.3.1. Type 1 Machinery Room - Engine Room

Relevant parameters of the engine room used in each acoustic model are tabulated in table 3.2. The mean absorption coefficient is quite difficult to determine in the noise prediction problem largely due to the massive equipment, pipes and cables within the engine room. If the engine room is to be treated as an ordinary industry room, empirical corrections are required on the acoustic models. Based on the characteristic of each acoustic model, the absorption coefficients involved are computed. A more accurate absorption coefficient value can be

obtained by using reverberation time (T60) in the room. The computed and measured absorption coefficients using T60 are tabulated in table 3.3. The absorption coefficient estimated from T60 measurements shows that there are some room contents that have good absorption at lower frequencies. This seems not being captured by the five acoustic room models as the room contents or furnishing are not completely considered during the computation. The insulation materials on the boundaries perform good absorption at high frequency but poor at a lower frequency. Therefore, the calculated absorption coefficients in L1 to L5 models at 125 Hz is lower than the T60 absorption coefficients.

Engine Room	L	W	H	S	V	MPF	TM	BP	Q	SH	Ss	F	h
L1	15 m	14.25 m	6.5 m	776.25 m²	1491.75 m³	7.69 m	30 °C	1013 Mba					
L2			6.5 m										
L3				8351.21 ft²					2	4175.6 ft²	1670.24 ft²		
L4	15 m	14.25 m	6.5 m	776.25 m2	1491.75 m³							0.09/m	1.5 m
L5		14.25 m	6.5 m	776.25 m3	1491.75 m³								
SEA-DF	15 m	14.25 m	6.5 m										

Table 3.2 Engine room parameters used for acoustic models and SEA-DF [60]

	Engine Room Mean Absorption Coefficient					
	125	250	500	1000	2000	4000
L1	0.03	0.31	0.60	0.57	0.55	0.59
L2	0.03	0.22	0.42	0.40	0.38	0.41
L3	0.08	0.25	0.43	0.42	0.41	0.42
L4	0.03	0.31	0.60	0.57	0.55	0.59
L5	0.03	0.31	0.60	0.57	0.55	0.59
T60	0.24	0.32	0.43	0.43	0.6	0.6

Table 3.3 Room mean absorption coefficient in engine room [60]

The SEA-DF approach uses the T60 absorption value. It treats engines and turbochargers as rectangular source and points source, respectively. The reverberant acoustic powers injected to the SEA subsystem of the engine room are shown in table 3.4. The relative error in all four locations is shown in figure 3.5. Each prediction model is expressed in dB. In the preliminary stage where accurate average absorption coefficient absorptions are not available, the predictions by simple acoustic models are quite conservative as shown in the high relative errors. Under such condition, the Heerema and Hodgson (L4) model exhibit the lowest prediction error for the four locations. The SEA-DF approach using the T60 absorption value in the noise calculation gives a better result. For example, at Location 3 (see figure 3.5) where it is influenced by a strong direct field, modeling the engine as a rectangular source in SEA-DF approach seems to fit well with the L4 and also an L2 model.

Source Type	Equipment	Octave Band Frequency					
		125	250	500	1000	2000	4000
Sound Power Level (dB)	Engine 1	116.8	116.3	116.5	116.5	111	111
	Engine 2	116.8	116.3	116.5	116.5	111	111
	Turbocharger 1	110.8	102.3	103.5	108.5	112	119
	Turbocharger 2	110.8	102.3	103.5	108.5	112	119

Table 3.4 Injected reverberant acoustic power into SEA subsystem of engine room **[60]**
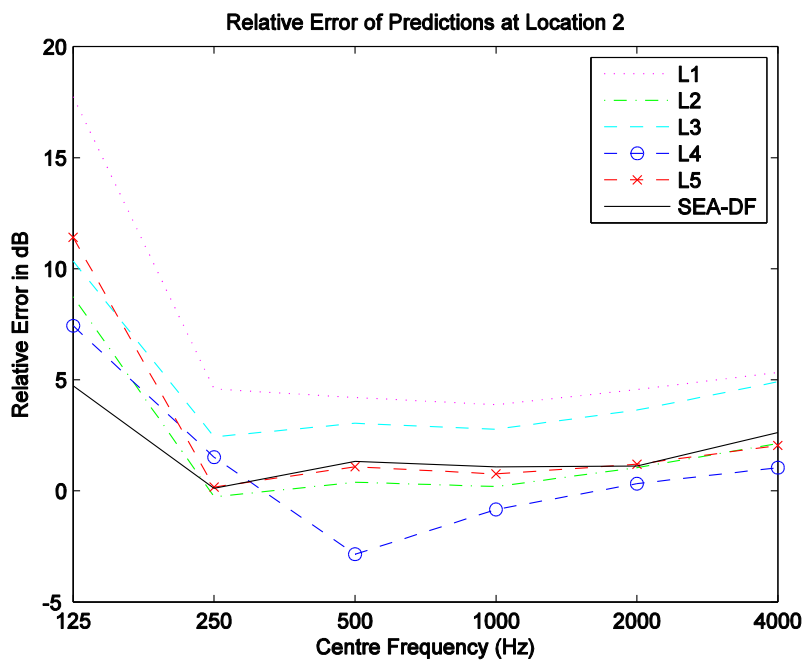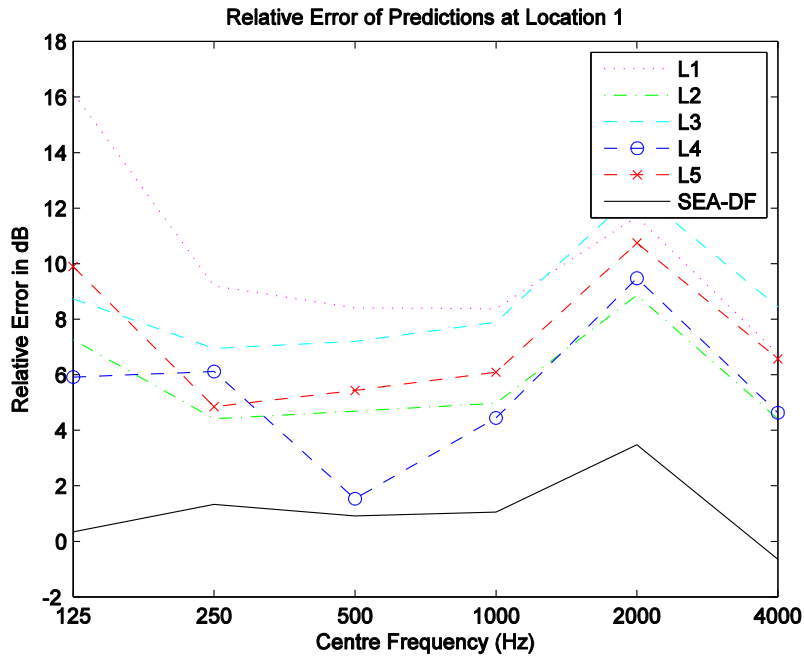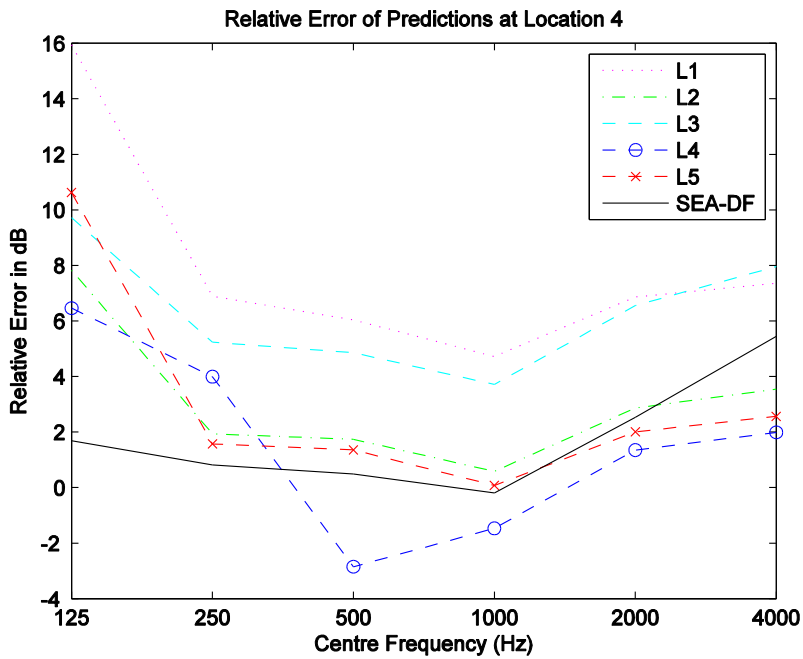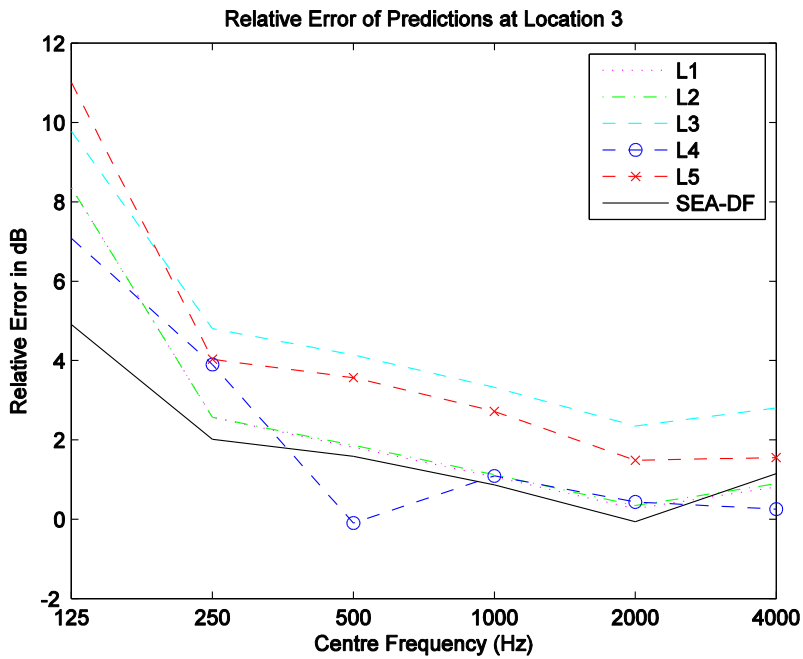
Figure 3.5 Relative error between SEA-DF and simple acoustic models at four locations in engine room **[60]**

In addition, according to the IMO requirement on noise measurement, the A-weighted equivalent sound level, L_{Aeq} shall be taken using spatial averaging method to cater for variation in reading due to irregular operation in the sound field. Hence, the spatial averaging error of L_{Aeq} is compared between the simple acoustic models. The spatial averaged error is calculated for each method. As seen in figure 3.6, the SEA-DF using the measured absorption coefficient achieves the smallest error of 1.4 dB as compared to the lowest error among the

simple acoustic models such as Heerema and Hodgson (L4) model and Kuttruff model (L2) with an error of approximately 1.7 dB and 2.4 dB, respectively.
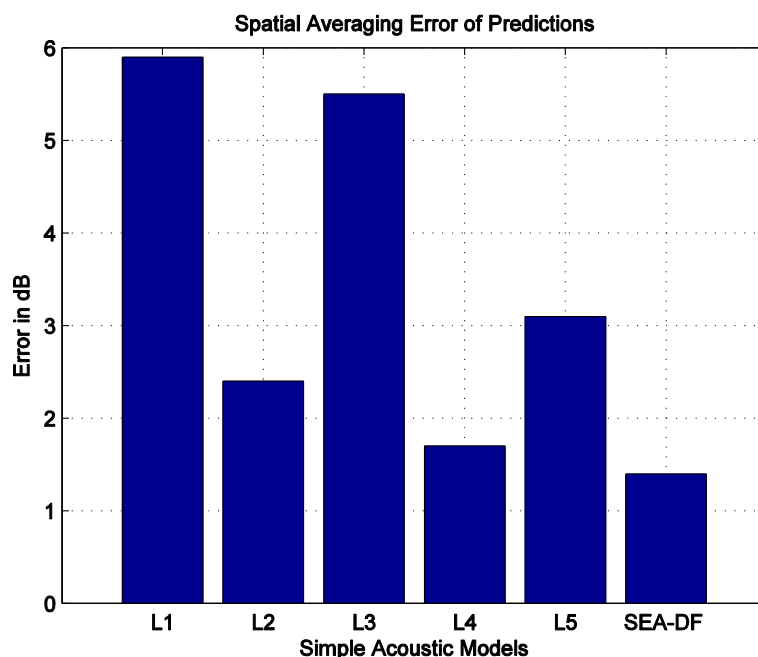
Figure 3.6 Spatial averaging error of five simple acoustic models and SEA-DF for engine room **[60]**

3.3.2.   *Type 2 Machinery Room - Pump Room*

Pump room is classified as Type 2 machinery room. As compared to the Type 1 engine room, it is less occupied with equipment, square and has uniform absorption coefficient. Relevant parameters involved in each model calculation are tabulated in table 3.5. As shown in table 3.6, the room absorption coefficients are determined using the same way as shown previously. In the pump room case study, the values of the absorption coefficient estimation using T60 and the L3 model at Location 3 are quite close. However, it does not imply that L3 model can produce a better prediction of noise in the pump room. As shown in figure 3.7, all the five simple acoustic models give much higher error than the SEA-DF. The differences are mainly due to the absence of a structure-borne component. In contrast, SEA-DF using the absorption coefficient estimated from T60 measurement and point source modeling works well as both airborne and structure-borne transmissions are included in the computation. After removing the direct field components, the reverberant acoustic powers injected into the SEA subsystem of the pump room are shown in table 3.7.

Pump Room	L	W	H	S	V	MPF	TM	BP	Q	S_H	S_S	F	h
L1	6.75 m	6 m	4 m	183 m²	162 m³	3.54 m	30 °C	1013 Mba					
L2			4 m										
L3				1968.78 ft²					2	590.63 ft²	196.88 ft²		
L4	6.75 m	6 m	4 m	183 m²	162 m³							0.11/m	1 m
L5		6 m	4 m	183 m²	162 m³								
SEA-DF	6.75 m	6 m	4 m										

Table 3.5 Pump room parameters involved in each acoustic model and SEA-DF [60]

	Pump Room Mean Absorption Coefficient					
	125	250	500	1000	2000	4000
L1	0.45	0.45	0.57	0.68	0.72	0.72
L2	0.31	0.32	0.39	0.47	0.49	0.49
L3	0.42	0.49	0.50	0.51	0.54	0.58
L4	0.45	0.45	0.57	0.68	0.72	0.72
L5	0.45	0.45	0.57	0.68	0.72	0.72
T60	0.42	0.49	0.51	0.51	0.54	0.58

Table 3.6 Mean absorption coefficient for pump room [60]

Source Type	Equipment	Octave Band Frequency					
		125	250	500	1000	2000	4000
Sound Power Level (dB)	Cooling Pump 1	89.6	89.1	88.0	85.9	83.6	80.2
	Cooling Pump 2	89.6	89.1	88.0	85.9	83.6	80.2
	Ballast Pump	88.6	88.1	87.0	84.9	82.6	79.2
	Bilge Pump	86.6	86.1	85.0	82.9	80.6	77.2

Table 3.7 Injected reverberant acoustic power into SEA subsystem of pump room [60]

Relative Error of Predictions at Location 1

Relative Error of Predictions at Location 2

Relative Error of Predictions at Location 3
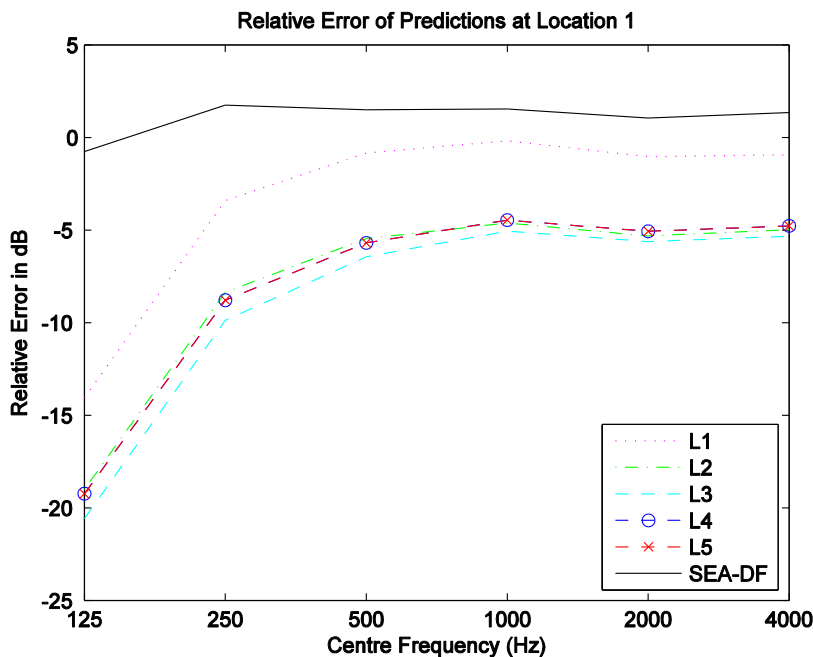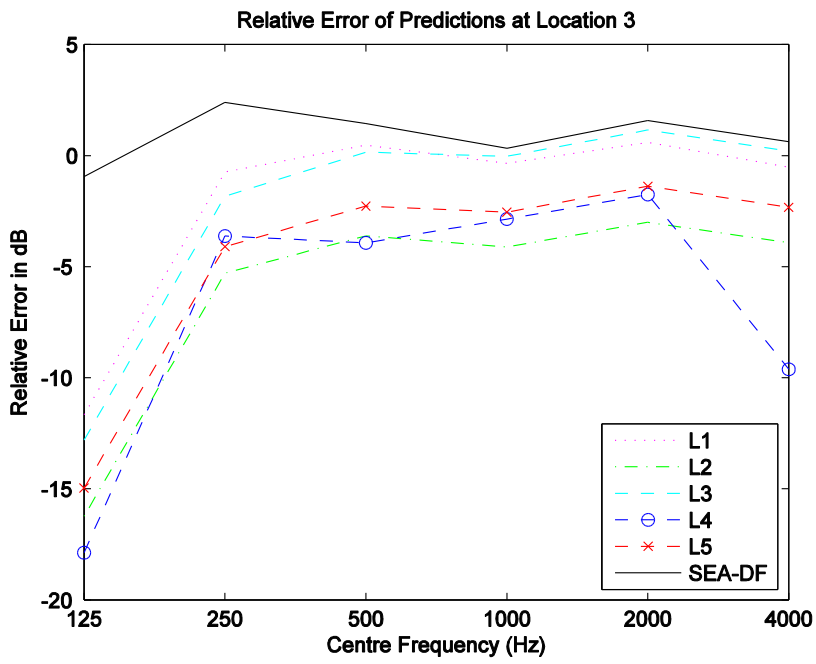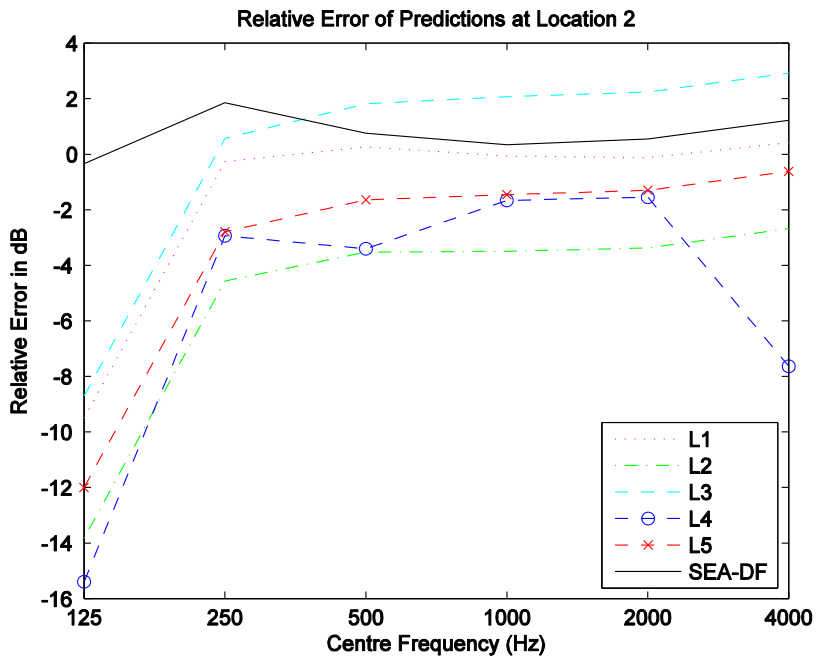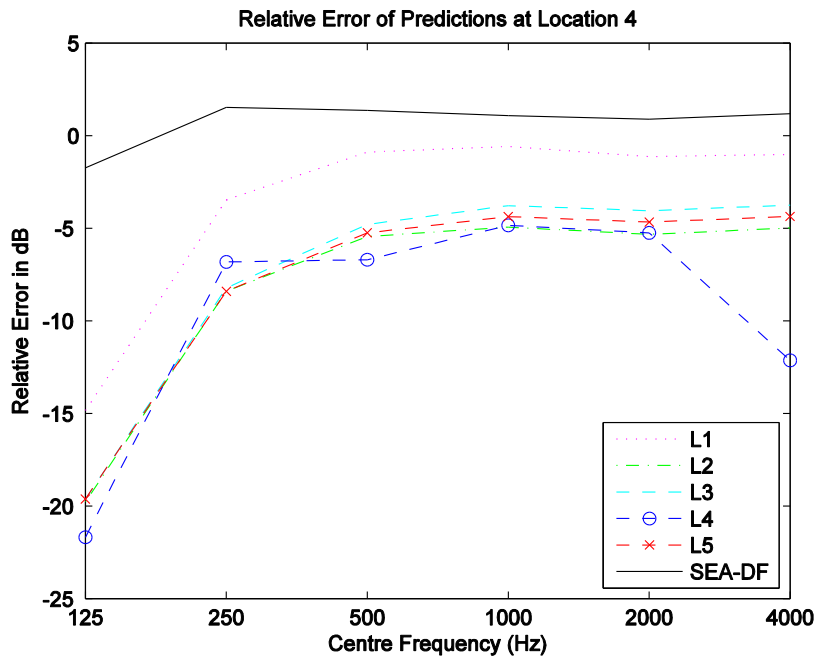
Figure 3.7 Relative error between SEA-DF and acoustic models at four locations in pump room **[60]**

The total vibration energy on the bottom deck contributes a big proportion of the total energy injected into the reverberant field of the pump room subsystem as shown in figure 3.8. The decomposition of SPL spectrum component in the reverberant field is shown in figure 3.9. It can be observed that at a lower frequency, the structure-borne noise is more dominant as compared to the airborne noise. Hence, the result shows that the airborne component and structure-borne component are indeed quite important for the pump room (Type 2).
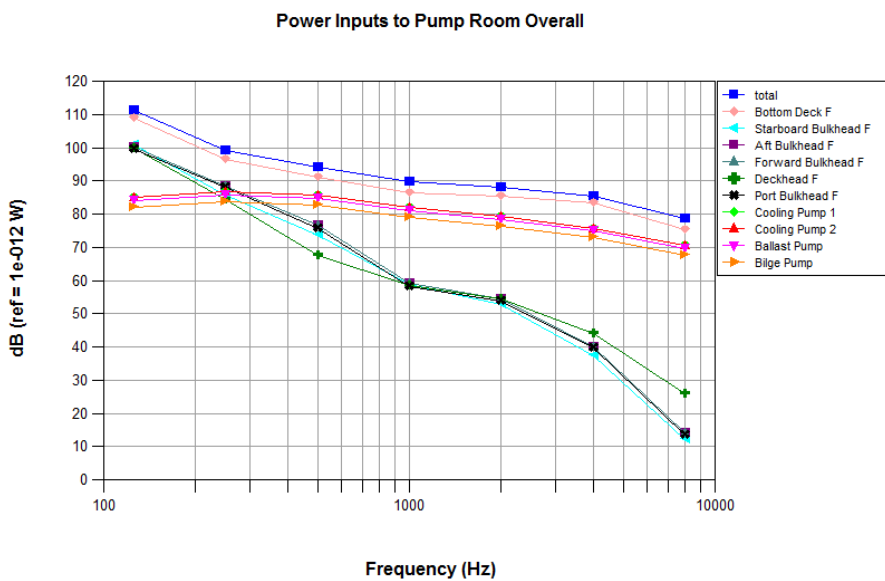
Figure 3.8 Sound power inputs to SEA subsystem of pump room **[60]**
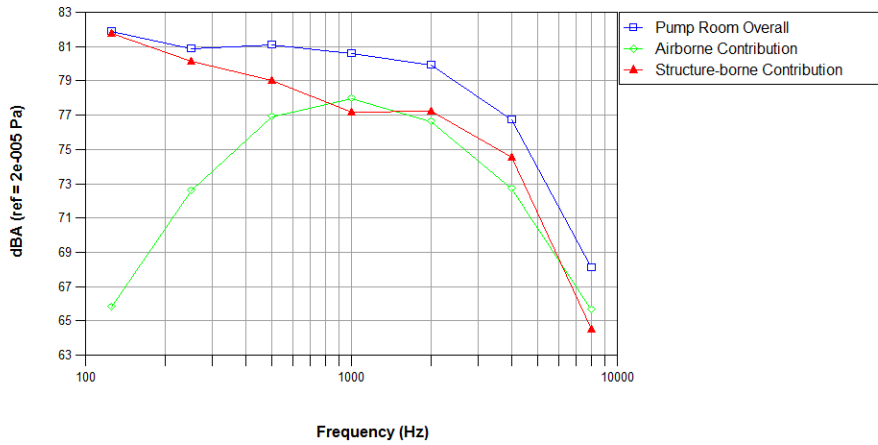
Figure 3.9 SPL of reverberant field in pump room **[60]**

With a maximum prediction error of 2.6 dB as seen in figure 3.10, an error of 0.7 dB on the spatial averaging noise level can be observed. It indicates that the SEA-DF model is capable of performing noise prediction for the Type 2 machinery room.
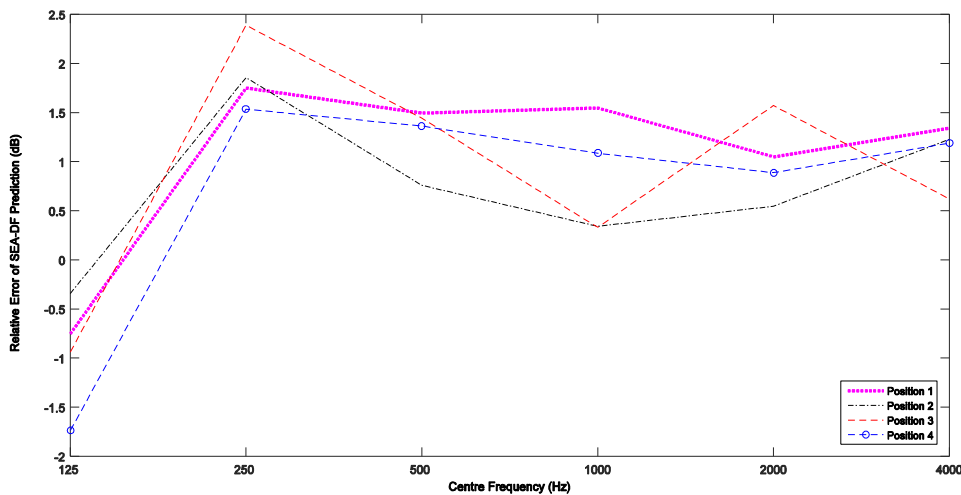
Figure 3.10 SEA-DF noise prediction error of pump room [60]

In the real practice, we noticed that the prediction accuracy of SEA-DF model is largely influenced by the absorption coefficient $\bar{\alpha}_i$. This is due to the fact that $\bar{\alpha}_i$ plays dual impacts in the SEA-DF approach. Firstly, it influences the injected reverberant sound power to the subsystem as a factor of $(1 - \bar{\alpha}_i)$ of the total source power. Secondly, it affects the level of acoustic power dissipated within the subsystem, Moreover, the SPL behaves differently for different $\bar{\alpha}_i$. For instance, figure 3.11 illustrates the change of reverberant noise level in the pump and engine room for different absorption coefficient $\bar{\alpha}_i$ computed at 1000 Hz. While $\bar{\alpha}_i$ increases to 0.2, the noise level has a sharp drop of approximately 15 dB. With further increased in $\bar{\alpha}_i$ to 0.4 results in only a reduction of around 4 dB as compared to the initial 15

39

dB. This implies that higher noise reduction can be achieved in only small absorption coefficient of $\bar{\alpha}_i \leq 0.2$. Hence, it is useful to establish a mean absorption coefficient information (e.g. SPL vs mean absorption coefficient) for different types of machinery room within the offshore platform.

$$SPL_{engine} = -97\bar{\alpha}_i^3 + 150\bar{\alpha}_i^2 - 91\bar{\alpha}_i + 120 \qquad [3\text{-}1]$$

$$SPL_{pump} = -82\bar{\alpha}_i^3 + 140\bar{\alpha}_i^2 - 83\bar{\alpha}_i + 97 \qquad [3\text{-}2]$$

By measuring the reverberation time T60 in these rooms, the absorption coefficient values can be determined by Sabine equation, Eyring equation or Millington Sette for different absorption coefficient and air attenuation conditions. The SPL can then be determined for these rooms. The study also shows that increasing the insulation thickness or area coverage in the room to achieve higher noise absorption (or noise reduction) may not be economically viable on an offshore platform.
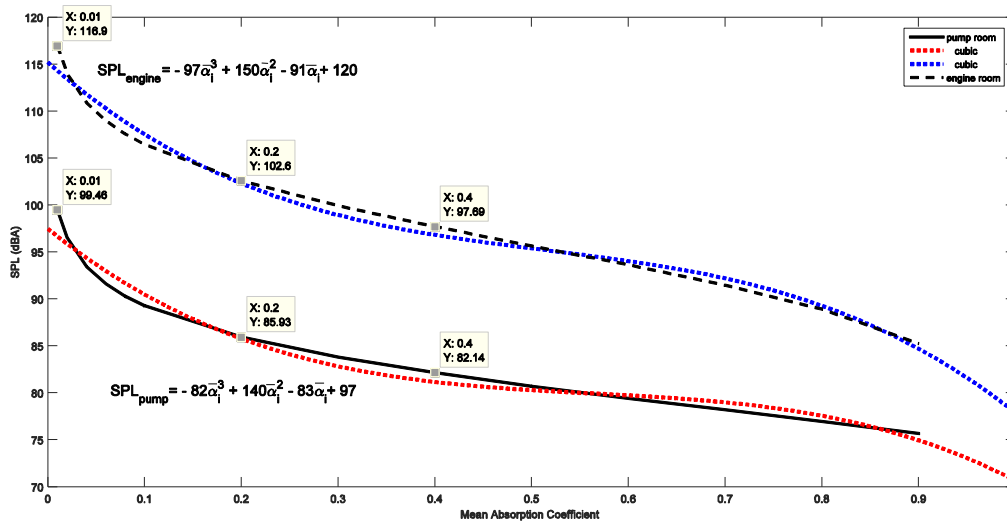
Figure 3.11 Effect of mean absorption coefficient on the SPL in pump and engine room **[60]**

3.3.3. Conclusion

The prediction of offshore platform machinery room noise level by the five empirical acoustic models and the proposed SEA with direct field (SEA-DF) computation approach were validated (at octave band 125 to 4000 Hz) with the measured SPL. In the airborne dominated engine room (Type 1 machinery room), the proposed SEA-DF approach using the measured T60 absorption coefficient gives better noise prediction than the Heerema and Hodgson model (L4) and Kuttruff model (L2). In addition, locations influenced by high direct field, modeling

the engine as a rectangular source in the SEA-DF approach exhibits smaller error (1.4dB) in prediction as compared to L4 and L2 model having 1.7dB and 2.4dB, respectively.

In the pump room (Type 2 machinery room), five acoustic models tend to have a lower relative error due to the absence of the structure-borne component. SEA-DF approach which involves both airborne and structure-borne components exhibits 0.7 dB on the spatial averaging noise level. It shows that the structure-borne noise is quite significant for the pump room. The proposed SEA-DF approach is a useful tool to analyse both the airborne and structure-borne sounds during the design stage.

The sensitivity study indicates that the sound pressure level (SPL) is sensitive when the mean absorption are small. Implementing acoustic insulation would be effective if the room means absorption coefficient is below 0.2. On the other hand, increasing the insulation thickness in the room beyond certain value will not lead to a significant further reduction. This study provides a useful tool to optimise the design of the acoustic insulation in the machinery rooms.

3.4.   Noise Prediction for Working Space and Living Space with Statistical Energy Analysis-Direct Field Method (SEA-DF)

Structure-borne noise is an important component in the working spaces and living spaces where the airborne noise is less dominant. SEA-DF has been validated in section 2.3 on determining the sound field influences by both airborne and structure-borne noise. Therefore, SEA-DF can be a proper tool for computing the noise level in the working and living spaces of an offshore platform.

In the real practice, applying damping treatments such as damping tiles and floating floors/room system are the standard design to reduce the of the vibration energy along the transmission path. As a result, the vibration energy can be minimised before it can build up and radiate as noise in the receiving compartments. Typically, damping tiles are applied to the middle of un-stiffened steel plating of the source room or the room adjacent; while floating floor/room system is usually installed in the living spaces for both mitigating the structure-borne noise radiation and isolating the room space. The configuration of damping tiles and floating floor/room system are shown in the figure 3.12 and figure 3.1 respectively.
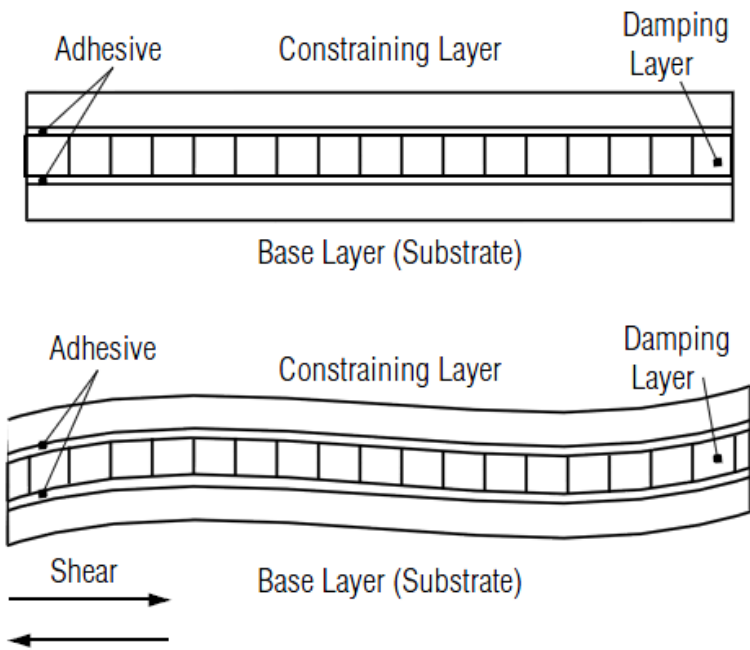
Figure 3.12 Constrained-layer construction (top) and under flex condition (below) [2]

	PRODUCT : PU-D20 CONCRETE SYSTEM
F1	THICKNESS : 1mm (VISCO ELASTIC) 10mm CONCRETE
F2	PRODUCT : VINYL SIZE : 2mtr (W) x 2mm (Thk.)
F3	PRODUCT : EPOXY FLOOR SIZE : 5mm (Thk.)
F4	PRODUCT : VISCO ELASTIC THICKNESS : 1mm
F5	PRODUCT : LATEX THICKNESS : 5mm (Thk.)
F6	PRODUCT : CEMENT THICKNESS : 7mm
F7	PRODUCT : COMPUTER RIASED FLOOR
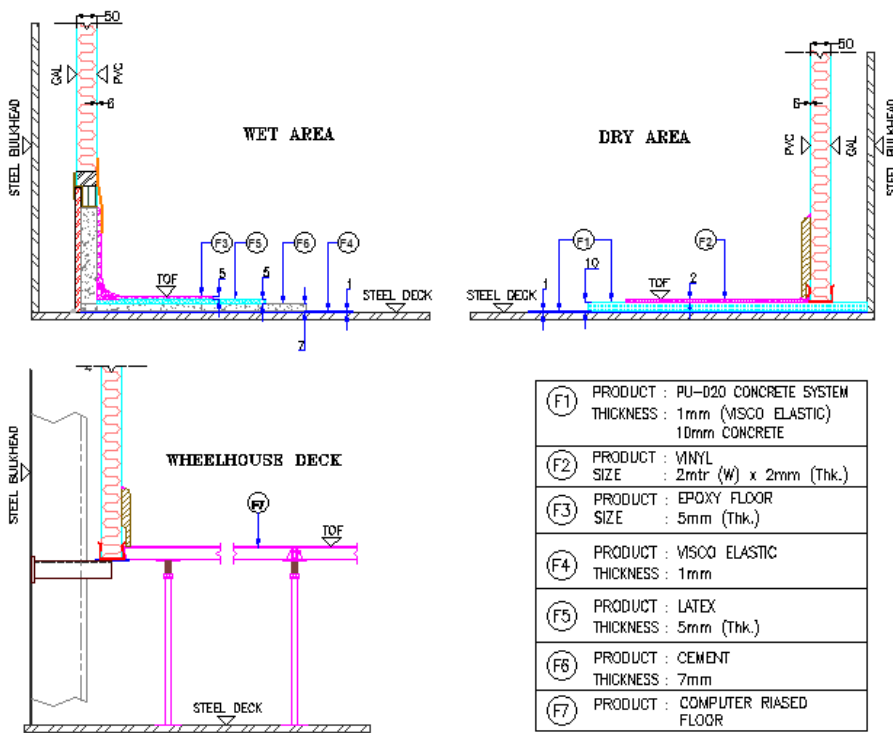
(a) Typical construction of deck covering system for dry areas, wet areas, and control rooms [78]

42

(b) Dry area 'floating room' applied in the cabin [78]

Figure 3.13 Floating room/system construction

In this study, software VA-One SEA module is employed as a tool to predict the nose level in the working and living spaces onboard a jack-up rig and investigate the efficient way of implementing damping treatment.

The SEA model of a full-scale jack-up rig has been built with hull dimension of 88.8m (L) x 115.1m (Breadth) x 12m (Depth). It has five tiers living spaces are located at the forward hull; the major noise sources machinery rooms such as engine rooms, mud pump room are arranged at the aft of the hull. Several compartments are selected for carrying out the effect the damping treatment study, including the port engine room, mud pump room, engine control room (ECR), store, cabins D08A, and the operation control room.

The SEA model is built based on the structural drawings and general arrangements of the rig. Bulkheads and decks are represented by the ribbed plates; air medium is represented by the room cavity. The major airborne and structure-borne noise source data that obtained from vendors are incorporated and described using its sound power level and the vibration level, respectively. The initial calculation considers the condition when no noise control treatment is applied. The full SEA model and the selected compartments are shown in figure 3.14. The calculated sound pressure level throughout the rig are plotted in the figure 3.15. It is seen that

the engine rooms' noise level can reach up to 116 dBA at the initial calculation. The noise level in the mud pump room, ECR, store room are in the range of 95.3 dBA, 80.7dBA, and 82.8 dBA respectively; in the remote cabin D08A and operation room, noise level is 51.2 dBA and 43.8 dBA. The calculation results of selected rooms except the operation control room are all exceeding noise criteria, and therefore, implementing certain noise treatment is necessary to reduce the noise levels and fulfill the regulation requirements. In reality, acoustic insulation and damping treatment are two methods usually used to absorb the acoustic pressure reflection in the compartment and reduce the vibration energy from transmitting, respectively. The sensitivity of acoustic insulation in mitigating the sound pressure level in compartments has been discussed in section 2.3, in this section, only the damping treatments are implemented to illustrate the structure-borne sound transmission characteristic and controlling strategy.

The damping tile with 6mm constraint damping layer and 3mm constraint layer are used in this study. The individual components in the all types of floating room showing in figure 3.13 (a) are modeled are exactly modeled under noise control treatment package of VA-One software. Their predefined physical properties and representation in the software are listed in table 3.8.
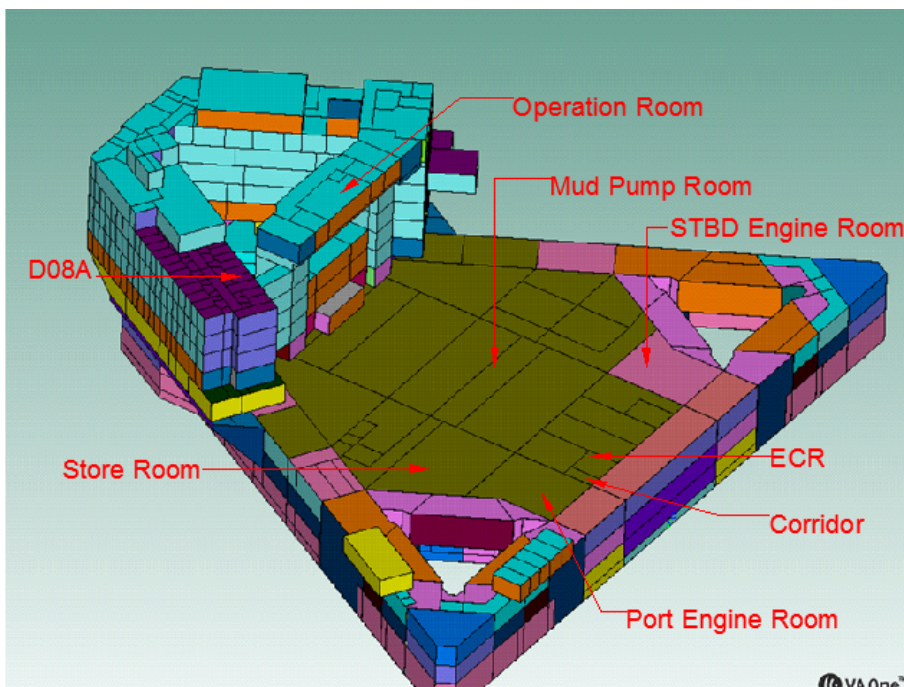
Figure 3.14 Jack-up rig full-size SEA model and the compartment involved [78]
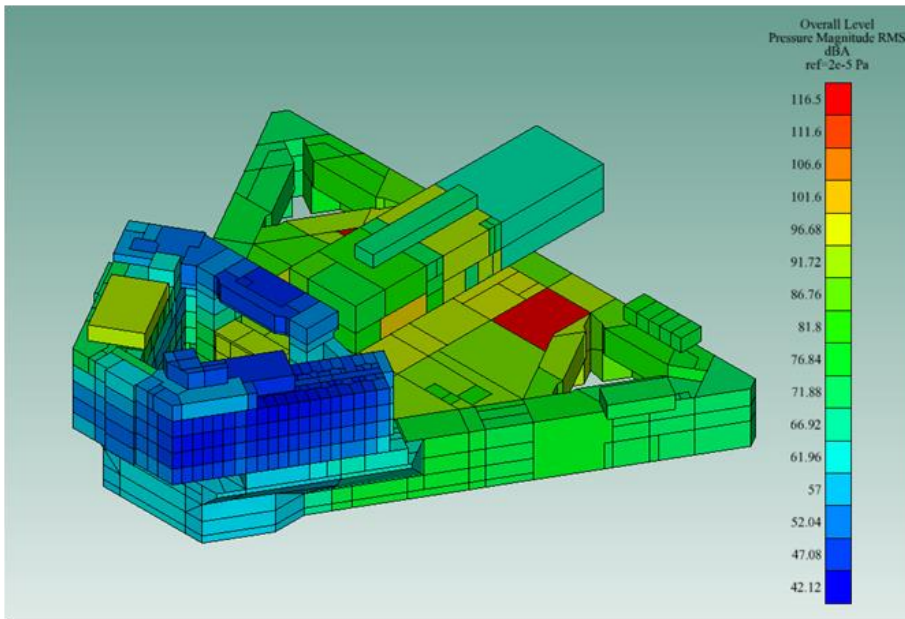
Figure 3.15 sound pressure levels calculated by SEA

Isotropic/Visco-elastic Material	Represent-ation	Density kg/m3	Tensile Modulus Pa	Shear Modulus Pa	Poisson's Ratio	Loss Factor
Steel	Steel	7800	2.1×10^{11}	8×10^{10}	0.3125	
Visco-elastic VNYL Concrete/Cement	Visco-elastic Polymer	1000		1×10^{5}	0.9	50%
	Plywood	700	6×10^{9}	2.4×10^{9}	0.25	
	Concrete	2300	2.5×10^{10}	1×10^{10}	0.25	
Latex	Hard Rubber	1100	2.3×10^{9}	7.72×10^{8}	0.4896	

Fiber Material	Represent-ation	Density kg/m3	Flow Resistivity N.s/m4	Porosity	Tortuosity	Viscous c.l.m
Mineral Wool	Mineral Wool	50	6×10^{4}	0.95	3.2	5.00E-05

Table 3.8 Physical properties and representation of material of the floating room components **[78]**

Due to the precondition of SEA technique on the modal density (minimum three modes in the bandwidth), it is capable of determining the high frequency noise and vibration accurately. By checking the mode counts in each octave band for the model subsystems, the minimum solving frequency for this rig is set at 125Hz. Therefore, the solving frequency range of 125 ~ 8000 Hz is established.

The following six scenarios are created to investigate the structure-borne noise propagation and the effect of damping treatments.

- R0 - Bare steel model
- R1 – 9mm damping tiles applied to all boundaries of engine rooms and mud pump room
- R2 – 9mm damping tiles applied to half bulkheads and bottom deck of engine rooms and mud pump room
- R3 – 9mm damping tiles applied to the bottom deck of engine rooms and mud pump room
- R4 – Install the dry area type floating system (figure 3.13(a)) to all cabins
- R5 – Install the wet area floating system (figure 3.13(a)) to all cabin
- R6 – Install the raised access floor (figure 3.13(a)) in the operation control room

Figure 3.16 to figure 3.21 present the variation of sound pressure level (SPL) in the port engine room, mud pump room, ECR, store room, cabin D08A, and operation control room under the condition of R0 to R3; and table 3.9 tabulates the equivalent under this condition. It is observed that applying damping tiles for the engine room and mud pump room cannot significantly reduce the room noise level (figure 3.16 and figure 3.17) whereas the adjacent ECR and store room (figure 3.18 and figure 3.19) response well. There is a large reduction in the noise level after damping tiles installed in the source rooms. Especially when all boundaries are wrapped by the damping tile illustrated by scenario R1, 3.6dB and 5.2dB reduction on the equivalent SPL are produced in the storeroom and ECR respectively. It is due to the reason that the damping tile dissipates the vibration energies. Meanwhile, it increases the boundary thickness which reduces the airborne noise transmission to the adjacent rooms. Scenario R2 results in moderate SPL reduction and Scenario R3 shows the least effect on the SPL decrease in the ECR and store room. In reality, R2 is adopted although R1 performs best due to economic and weight control reasons. It is also observed that installing of damping tiles in the remote engine room and mud pump room seldom benefits the cabin D08A (figure 3.22) and operation control room (figure 3.23). These living spaces noise level is more influenced by the nearby sources rather than the engine room and mud pump room in the main hull. Therefore, the damping tile installations in these rooms have limited impact in the remote living spaces.
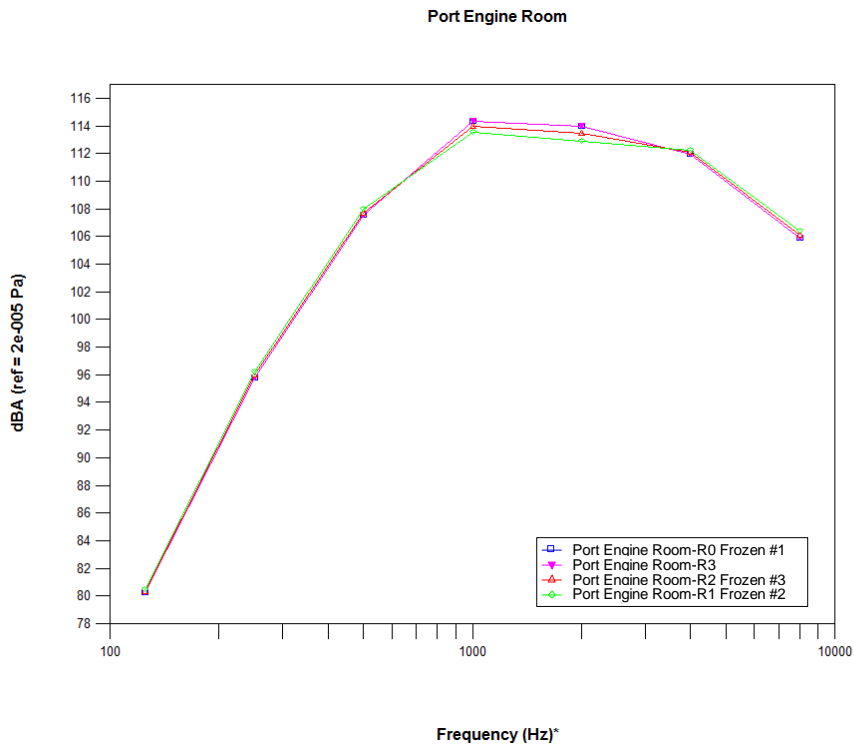
Port Engine Room

Figure 3.16 SPL of port engine room under the condition of R0 to R3 **[78]**
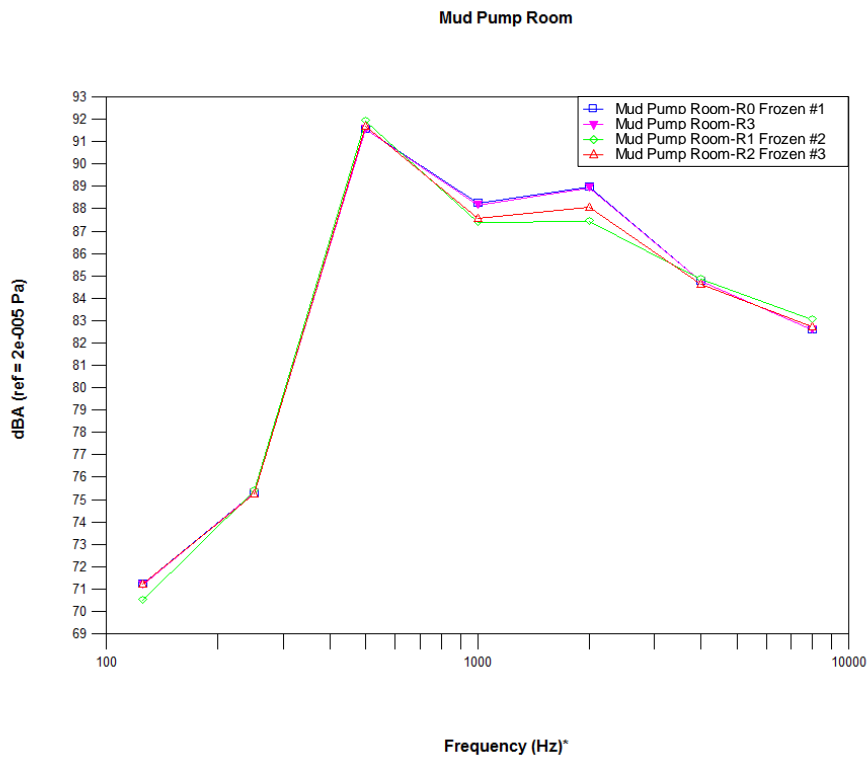
Mud Pump Room

Figure 3.17 SPL of mud pump room under the condition of R0 to R3 [78]
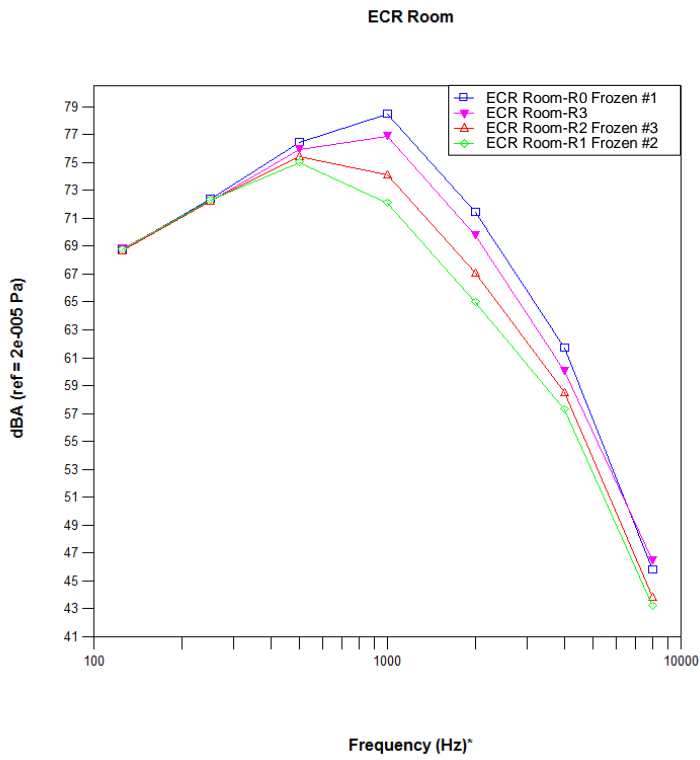
Figure 3.18 SPL of the ECR under the condition of R0 to R3 [78]
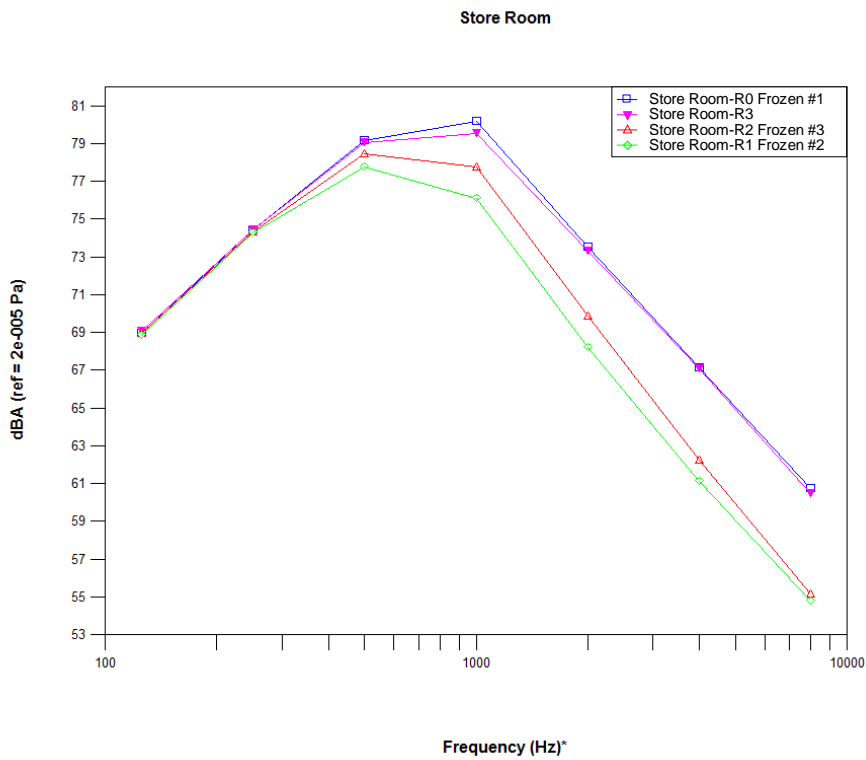
Figure 3.19 SPL of the store room under the condition of R0 to R3 [78]
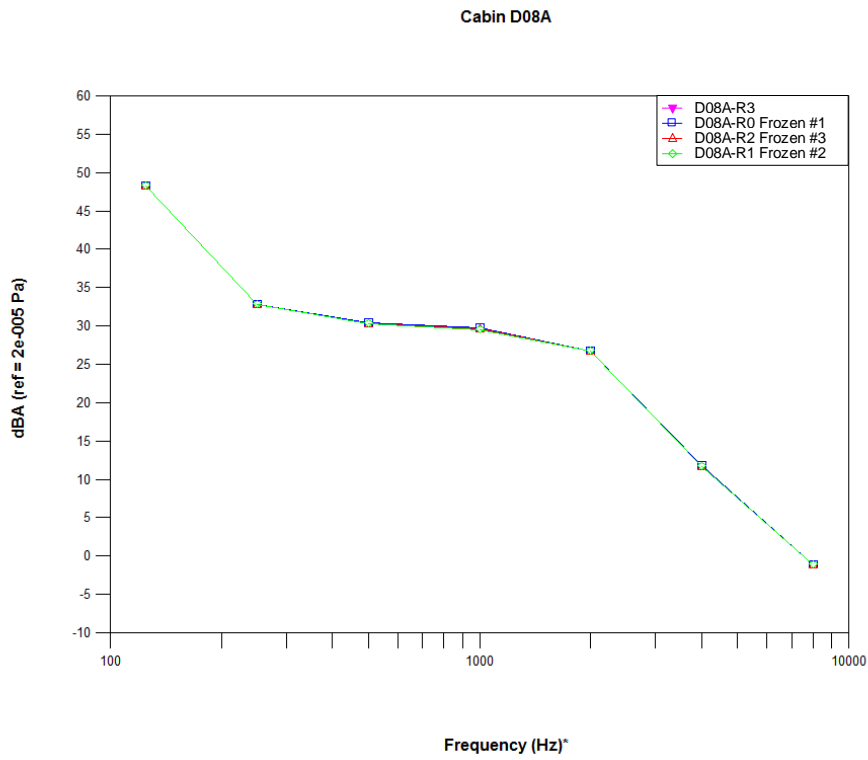
Figure 3.20 SPL of cabin D08A under the condition of R0 to R3 [78]
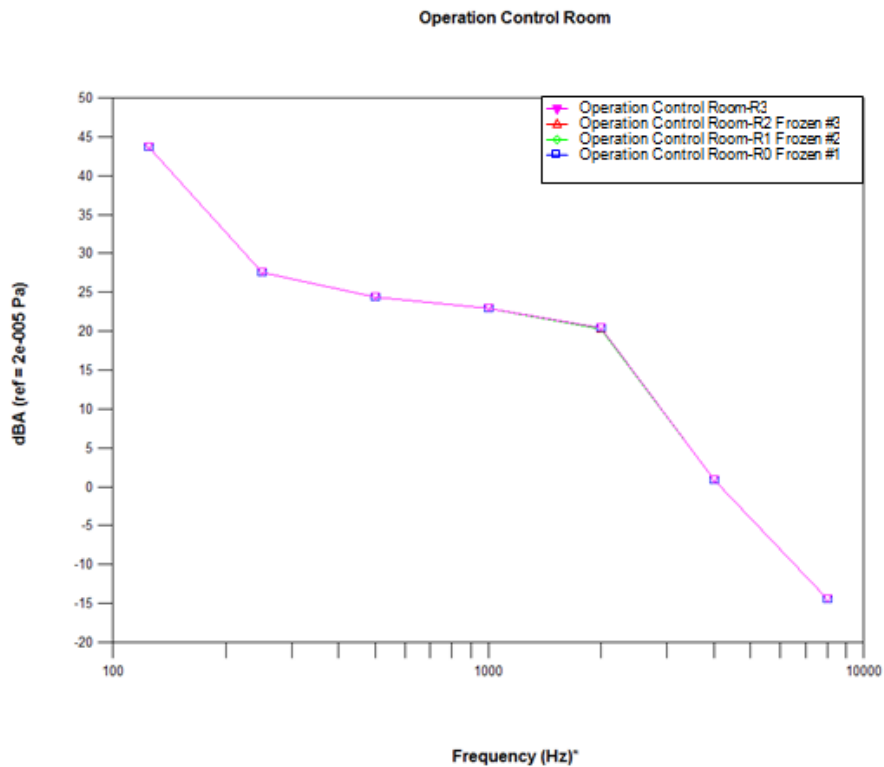
Figure 3.21 SPL of operation control room under the condition of R0 to R3 [78]

	Equivalent Noise Level (dBA)			
Rooms	R0	R1	R2	R3
Port Engine Room	116.5	116.5	116.4	116.3
Mud Pump Room	95.3	95.1	95.1	95.3
Store Room	82.8	79.2	80.2	82.2
ECR	80.7	75.5	77.4	79.1
Cabin D08A	51.2	51.2	51.2	51.2
Operation Control Room	43.8	43.8	43.8	43.8

Table 3.9 Equivalent SPL comparison for the first four conditions [78]

Floating room system apply to the living spaces can be more effective on mitigating the structure-borne noise in the rooms. Figure 3.22 and figure 3.23 compared the cabin D08A and operation control room's noise level before and after the floating room system been installed. It can be seen that SPL at all frequencies are largely reduced after with the effect of floating room system. As seen in table 3.10, it expects a 4 dB reduction for the cabin D08A and operation control room with the performance of the floating rooms system in this case.

	Equivalent Noise Level (dBA)			
Rooms	R0	R4	R5	R6
Cabin D08A	51.17	47.2	47.15	
Operation Control Room	43.83			38.76

Table 3.10 Equivalent SPL comparison for condition R0, R4, R5 and R6 [78]
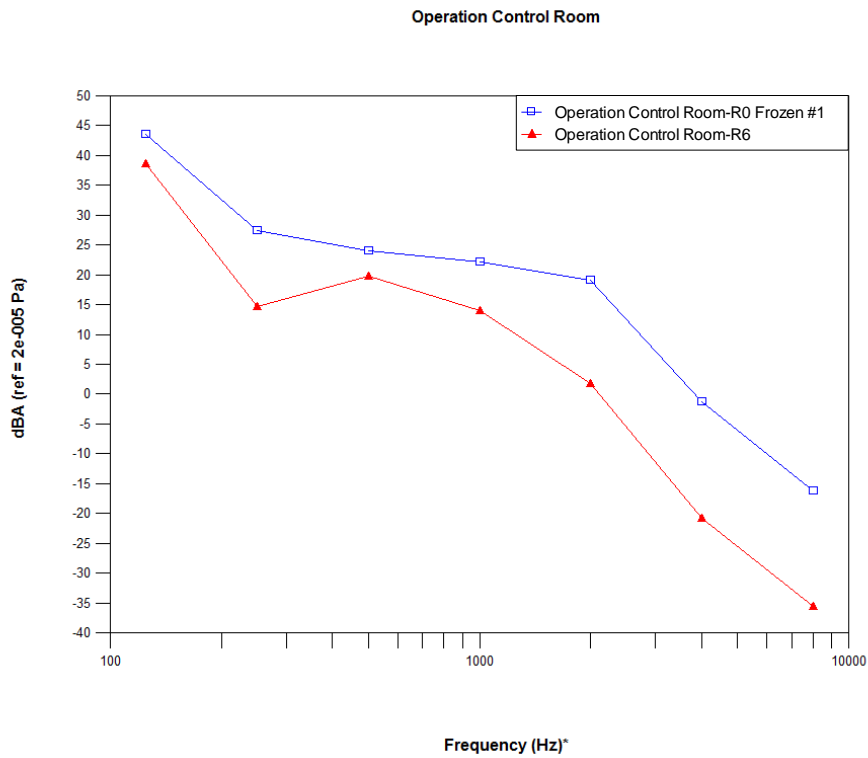
Figure 3.22: SPL of cabin D08A under the conditions of R0, R4, and R5 **[78]**
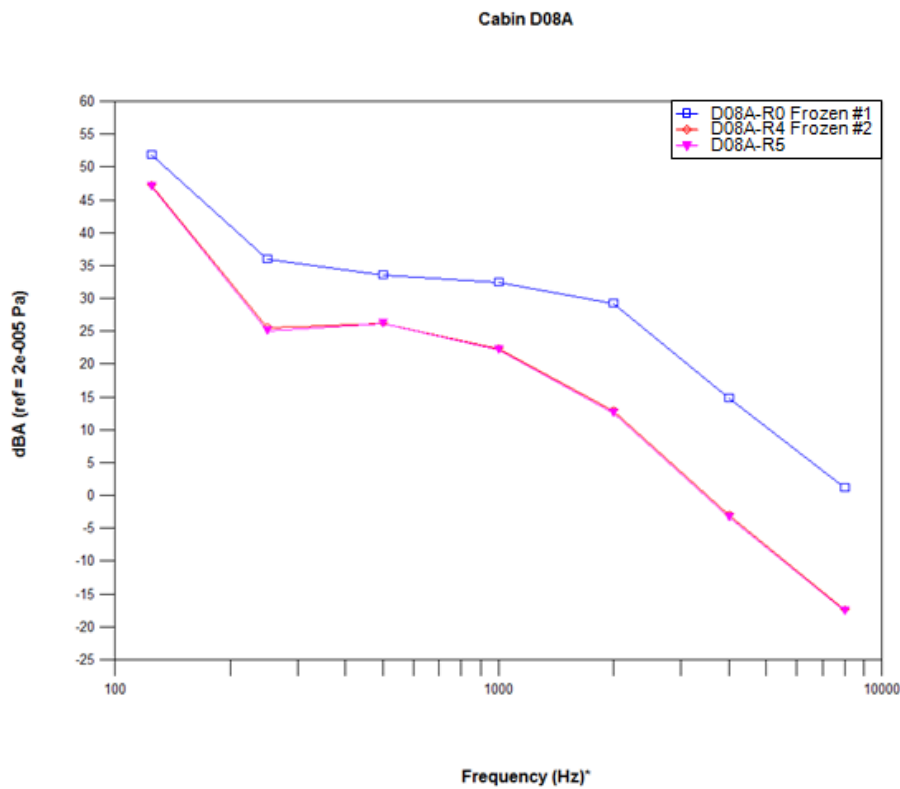
Figure 3.23: SPL of operation control room under the conditions of R0 and R6 **[78]**

Base on the noise analysis in the rig, noise treatment shall be designed for the offshore platform to reduce the noise level in the concerned compartments in order to comply with regulation criteria. In the major source rooms such as engine room and mud pump room, acoustic insulation and damping tiles may reduce the interior noise level and the adjacent

51

working spaces noise level which profoundly influenced by both airborne transmission and structure-borne noise radiation; floating room system is particularly effective in reducing the noise level in the living spaces.

Through performing the noise analysis for the jack-up rig, the characteristic of structure-borne noise in the machinery spaces, working spaces, and living spaces are understood. Although the actual SPL reduction value maybe different with the change of damping tile property or floating room configuration adopted, the study can help engineers make correct choices on different noise control method for different spaces and help develop more efficient and economical noise control solutions for the rig design.

The actual finalised noise control design of the rig is incorporated in the SEA-DF model in the next stage, and perform the noise analysis for the real situation. The ultimate SPLs in each compartment are collected and used as the training samples for developing the neural network model in the Chapter 6.

3.5.   Concluding Remarks

The chapter performs the noise analysis for the machinery spaces, working spaces, and living spaces of an offshore platform. Through validate five empirical SPL formula originated from other application with experimental measurements, it was found that the Heerema and Hodgson (L4) model is capable of computing SPL in the airborne noise dominated Type 1 machinery room with very low errors. The proposed SEA-DF method overcome the shortcomings of the conventional SEA technique that cannot provide localised SPL and give satisfy prediction results for both Type 1 and Type 2 machinery room. This conclusion not only helps engineers to specify correct SPL prediction tool for the different type of machinery room, but also provide them the simplest formula of obtaining the SPL in the Type 1 machinery room.

On the other hand, the conventional SEA method is suitable for computing the noise level in the working space and living space where the direct field is not predominant. Through performing noise analysis for a whole jack-up rig, the structure-borne noise transmission characteristic is understood. In addition, the optimal ways of implementing damping treatment to control structure-borne noise level in the working spaces and living spaces are identified.

Due to a complex of the offshore platform, large numbers of the transmission path exist. Therefore, a full-scale SEA model is needed for predicting the noise level of all compartments at high frequencies. It is noted that time spent on building a full-scale SEA model is

approximately two months, which is sophisticated and time-consuming. Moreover, the SEA model is subjected to change with the changing of rig design at the preliminary stage. It is therefore expected a new prediction tool that can handle the noise prediction task practically and accurately, so that help the design of offshore platform meet the criteria for crews' comfort and protection against high noise level.

Chapter 4.   Analytical Solution of Elastic-restrained coupled plate and Three-dimensional Structural-acoustic Interaction using Chebyshev-Lagrangian method

4.1. Introduction

It has been discussed in the Chapter 2 that the vibro-acoustic of an offshore platform should consider the effects of structural-structural coupling and structural-acoustic interaction. The three-dimensional fully coupled structural-acoustic system has to be solved simultaneously to acquire for the correct dynamic quantities such as vibration displacements and sound pressure levels. Purely analytical methods are deterministic, computationally efficient, and physically insightful. It is usually preferred when a parametric study needs to be performed, by modifying parameters in the analytical model without changing the solution procedure. Moreover, the analytical method does not restrict by the problem-solving frequency as comparing to the FEA and SEA technique. Therefore, researchers have devoted great efforts to develop analytical methods for the vibro-acoustic problem. Typically, the dynamic characteristics of classical panel-cavity model have been extensively studied [12][19-20] [79-88]. An excellent review has been given by Pan et al [89]. Other configurations such as two cavity connected by boundary structures [90], double-panel structure with acoustic cavity [20] [86], multiple plates coupled with liquid [83] have been studied. However, these were based on the assumption that the plates are independent and disconnected. Thus, only the transverse vibration is taken into consideration while modeling the system vibro-acoustics. As point out by Pan and Farag [91], in-plane vibration has to be involved at the rigid coupling edge to satisfy the force and displacement equilibriums for the coupled structures. With the aid of spring technique, figure 4.1 illustrates the relationship between the transverse and in-plane vibration while two plates are coupled. The amount of energy transmission is governed by the connection manners reflected by the coupling stiffness K_{c_ij}, k_{cw_ij}, k_{cu_ij}, and k_{cv_ij} in the rotation and translational directions, respectively. For plates joint perpendicularly, the transverse wave propagation is mainly depend on the moment of rotation stiffness K_{c_ij}.
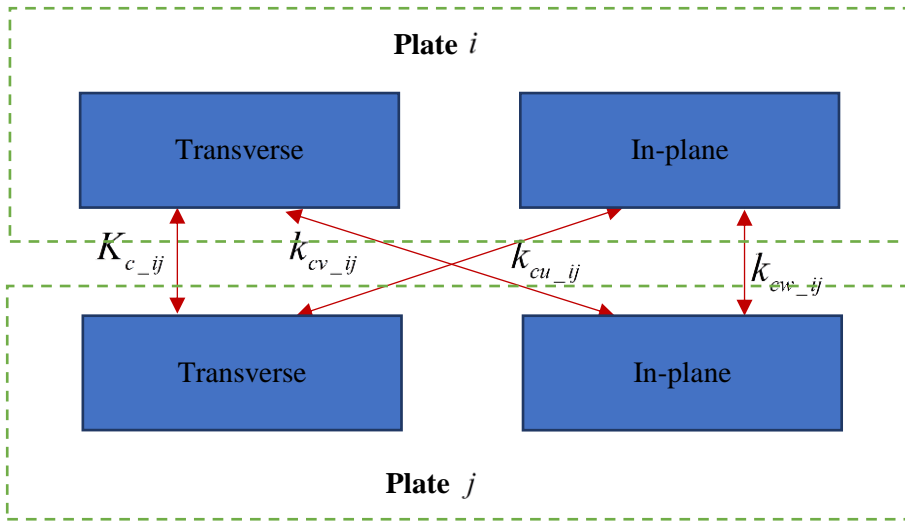
Figure 4.1 Illustration of waveform transfer between coupled plate i and plate j

To the extent of my knowledge, the analytical modeling of the three-dimensional fully coupled structural-acoustic configurations have not been developed, which is a real case in the offshore platform environment. This chapter tends to fulfill the gap and proposed an analytical model based on the Rayleigh-Ritz method for analysing the vibro-acosutics of the three-dimensional fully coupled structural-acoustic problem.

4.2. Theory and Formulations

4.2.1. Description of the three-dimensional fully coupled structural-acoustic model
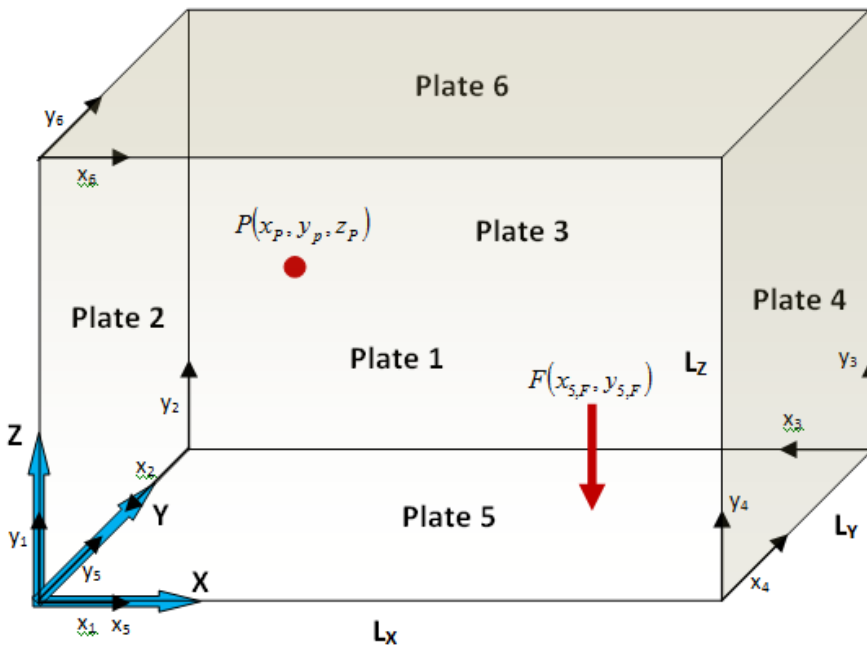
Figure 4.2 Schematic diagram of structural-acoustic coupling of a rectangular room

Concerning figure 4.2, the coupled vibro-acoustic system consisting of a finite-size rectangular acoustic cavity enclosed with six homogeneous and isotropic flat surface, occupying the spatial region $0 < x < L_X$, $0 < y < L_Y$, $0 < z < L_Z$. Room boundaries are numbered as indicated in the figure 4.2. Plate dimensions are denoted as $L_{i,x}, L_{i,y}$ in the Cartesian coordinates. The built-up system with a superposed reference between the global coordinate and the local coordinate of the 'plate #5'plate is investigated aiming illustrate dynamics of acoustic cavity and structures. The general boundary conditions and coupling condition are described by the boundary/ coupling forces and moments that are simulated according to the groups of translational and rotational boundary and coupling springs along each edge. To be specific, assigning boundary springs with stiffness K_w, k_w, k_p, and k_n for in the rotational, transverse, and two in-plane directions, and four groups of coupling springs with stiffness $K_{c\_ij}, k_{cw\_ij}, k_{cu\_ij}$, and k_{cv_ij} along the coupling edge. The assigned stiffness values control the boundary conditions and coupling manner of the structural system corresponding to the equation [2-12] to [2-16], for example, infinite value results in the clamp condition while zero value leads to the free condition. On the structural-acoustic interface, the boundary condition of the cavity satisfies the elastic boundary condition as specified in the equation [2-7], which implies that the velocity continuity on the coupling interface is enforced.

4.2.2. *Energy expressions of a fully coupled structural-cavity system*

The coupled system is theoretically modeled based on the energy principle by separately constructing the energy descriptions of the two components: the structural domain and the cavity domain. For the structure, the Lagrangian function L^S is expressed as follows

$$L^S = \sum_{i=1}^{N_S=6} \left(V_i^S - T_i^S - W_i^F + W_i^{AS} \right) + \sum_{ij} V_{ij}^C \tag{4-1}$$

where $V_i^S = V_i^T + V_i^{In}$ denotes the overall potential energy done due to transverse and in-plane deformation, $T_i^S = T_i^T + T_i^{In}$ is the overall kinetic energy of i th plate, W_i^{AS} and W_i^F are the work done by the interior acoustic pressure loading on the mutual structural-acoustic interface and work done by external force, V_{ij}^C is the potential energy generated by coupling effect and stored in the coupling springs between plate i and j. The specific expressions of the terms given in equation [4-1] can be written as [92] [12]

$$V_i^T = \frac{D_i}{2} \int_0^{L_{i,x}} \int_0^{L_{i,y}} \left[\left(\frac{\partial^2 w_i}{\partial x_i^2} \right)^2 + \left(\frac{\partial^2 w_i}{\partial y_i^2} \right)^2 + 2\upsilon_i \frac{\partial^2 w_i}{\partial x_i^2} \frac{\partial^2 w_i}{\partial y_i^2} + 2(1-\upsilon_i) \left(\frac{\partial^2 w_i}{\partial x_i \partial y_i} \right)^2 \right] dx_i dy_i$$

$$+ \frac{1}{2} \int_0^{L_{i,y}} \left[k_{w\_x_i0} w_i^2 + K_{w\_x_i0} \left(\frac{\partial w_i}{\partial x_i} \right)^2 \right]_{x_i=0} dy_i + \frac{1}{2} \int_0^{L_{i,y}} \left[k_{w\_x_i1} w_i^2 + K_{w\_x_i1} \left(\frac{\partial w_i}{\partial x_i} \right)^2 \right]_{x_i=L_{i,x}} dy_i$$

$$+ \frac{1}{2} \int_0^{L_{i,x}} \left[k_{w\_y_i0} w_i^2 + K_{w\_y_i0} \left(\frac{\partial w_i}{\partial y_i} \right)^2 \right]_{y_i=0} dx_i + \frac{1}{2} \int_0^{L_{i,x}} \left[k_{w\_y_i1} w_i^2 + K_{w\_y_i1} \left(\frac{\partial w_i}{\partial y_i} \right)^2 \right]_{y_i=L_{i,y}} dx_i$$

[4-2]

$$V_i^{In} = \frac{G_i}{2} \int_0^{L_{i,x}} \int_0^{L_{i,y}} \left[\left(\frac{\partial u_i}{\partial x_i} + \frac{\partial v_i}{\partial y_i} \right)^2 - 2(1-\upsilon_i) \frac{\partial u_i}{\partial x_i} \frac{\partial v_i}{\partial y_i} + \frac{(1-\upsilon_i)}{2} \left(\frac{\partial u_i}{\partial y_i} + \frac{\partial v_i}{\partial x_i} \right)^2 \right] dx_i dy_i$$

$$+ \frac{1}{2} \int_0^{L_{i,y}} \left[k_{n\_x_i0} u_i^2 + k_{p\_x_i0} v_i^2 \right]_{x_i=0} dy_i + \frac{1}{2} \int_0^{L_{i,y}} \left[k_{n\_x_i1} u_i^2 + k_{p\_x_i1} v_i^2 \right]_{x_i=L_{i,x}} dy_i$$

$$+ \frac{1}{2} \int_0^{L_{i,x}} \left[k_{n\_y_i0} v_i^2 + k_{p\_y_i0} u_i^2 \right]_{y_i=0} dx_i + \frac{1}{2} \int_0^{L_{i,x}} \left[k_{n\_y_i1} v_i^2 + k_{p\_y_i1} u_i^2 \right]_{y_i=L_{i,y}} dx_i$$

[4-3]

$$T_i^T = \frac{1}{2} \rho_{i,s} h_i \omega^2 \int_0^{L_{i,x}} \int_0^{L_{i,y}} w_i^2 dx_i dy_i$$

[4-4]

$$T_i^{In} = \frac{1}{2} \rho_{i,s} h_i \omega^2 \int_0^{L_{i,x}} \int_0^{L_{i,y}} (u_i^2 + v_i^2) dx_i dy_i$$

[4-5]

$$W_i^{AS} = \frac{1}{2} \int_0^{L_{i,x}} \int_0^{L_{i,y}} w_i p_i dx_i dy_i$$

[4-6]

$$W_i^F = \int_0^{L_{i,x}} \int_0^{L_{i,y}} F_i w_i dx_i dy_i$$

[4-7]

where ω is the angular frequency, w_i, u_i and v_i are the displacement components in the transverse direction and in-plane directions. F_i is the external point force normal to the plate i. $L_{i,x}$ and $L_{i,y}$ are the length and height of the plate i. D_i and G_i are defined as $G_i = E/(1+\upsilon)$ and $D_i = Eh_i^3/12(1-\upsilon^2)$. E, h_i, and υ represents Young's modulus, the thickness and Poisson's ratio of the plate i.

The coupling effects between plates are described by the coupling springs associated with the transverse moment, out-of-plane shear force, in-plane longitudinal force, and in-plane shear force. Three coupling expressions are presented to illustrate he potential energy due to structural coupling along x-, y- and z- directions.

$$V_{15}^C = \frac{1}{2}\int_0^{L_x}\left[\begin{array}{l}K_{c\_15}\left(\left.\frac{\partial w_1}{\partial y_1}\right|_{y_1=0}-\left.\frac{\partial w_5}{\partial y_5}\right|_{y_5=0}\right)^2+k_{cw\_15}\left(\left.w_1\right|_{y_1=0}-\left.v_5\right|_{y_5=0}\right)^2+\\ k_{cu\_15}\left(\left.u_1\right|_{y_1=0}+\left.u_5\right|_{y_5=0}\right)^2+k_{cv\_15}\left(\left.v_1\right|_{y_1=0}-\left.w_5\right|_{y_5=0}\right)^2\end{array}\right]dx_1 \qquad [4\text{-}8]$$

$$V_{25}^C = \frac{1}{2}\int_0^{L_y}\left[\begin{array}{l}K_{c\_25}\left(\left.\frac{\partial w_2}{\partial y_2}\right|_{y_2=0}-\left.\frac{\partial w_5}{\partial x_5}\right|_{x_5=0}\right)^2+k_{cw\_25}\left(\left.w_2\right|_{y_2=0}-\left.u_5\right|_{x_5=0}\right)^2+\\ k_{cu\_25}\left(\left.u_2\right|_{y_2=0}-\left.v_5\right|_{x_5=0}\right)^2+k_{cv\_25}\left(\left.v_2\right|_{y_2=0}-\left.w_5\right|_{x_5=0}\right)^2\end{array}\right]dx_2$$

$$V_{12}^C = \frac{1}{2}\int_0^{L_z}\left[\begin{array}{l}K_{c\_12}\left(\left.\frac{\partial w_1}{\partial x_1}\right|_{x_1=0}-\left.\frac{\partial w_2}{\partial x_2}\right|_{x_2=L_Y}\right)^2+k_{cw\_12}\left(\left.w_1\right|_{x_1=0}+\left.u_2\right|_{x_2=L_Y}\right)^2+\\ k_{cu\_12}\left(\left.u_1\right|_{x_1=0}-\left.w_2\right|_{x_2=L_Y}\right)^2+k_{cv\_12}\left(\left.v_1\right|_{x_1=0}+\left.v_2\right|_{x_2=L_Y}\right)^2\end{array}\right]dy_1$$

Similarly, the Lagrangian function L^A for the acoustic cavity I is constructed by the potential energy, V_I^A the kinetic energy, T_I^A stored in the cavity, the work contributed by the plate's transverse vibration W_i^{SA} and interior acoustic source loading W_P^A as

$$L^A = V_I^A - T_I^A + W_P^A - \sum_{i=1}^{N_S=6} W_i^{SA} \qquad [4\text{-}9]$$

Denoting the density and the acoustic speed in the cavity and sound pressure fluctuation with ρ_0, c_0 and p, respectively, the explicit expressions of the terms in the right side of equation [4-9] are given as follow [89]:

$$V_I^A = \frac{1}{2\rho_0 c_0^2}\int_0^{L_X}\int_0^{L_Y}\int_0^{L_Z} p^2 \, dXdYdZ \qquad [4\text{-}10]$$

$$T_I^A = \frac{1}{2\rho_0\omega^2}\int_0^{L_X}\int_0^{L_Y}\int_0^{L_Z}\left[\left(\frac{\partial p}{\partial X}\right)^2+\left(\frac{\partial p}{\partial Y}\right)^2+\left(\frac{\partial p}{\partial Z}\right)^2\right]dXdYdZ \qquad [4\text{-}11]$$

$$W_P^A = \frac{1}{2}\int_0^{L_X}\int_0^{L_Y}\int_0^{L_Z}\frac{pQ}{j\omega} \, dXdYdZ \qquad [4\text{-}12]$$

Due to the mutual interaction of plate and cavity, the expression for the work, W_i^{SA} share with the same expression with W_i^{AS} as given in equation [4-6]. In the equation [4-12], $j = \sqrt{-1}$ and Q denotes the distribution function of an acoustic source; a point source located at (x_0, y_0, z_0) in the cavity can be expressed as $Q = Q_0\delta(x-x_0)\delta(y-y_0)\delta(z-z_0)$, where Q_0 is the volume velocity amplitude of the

sound source, δ represents the delta function. [93]

At this point, the theoretical model of the coupled plate-cavity structure has been constructed. The general boundary and coupling condition of the plates are considered by the stored energy in the boundary and coupling springs. The coupling between the plate and the cavity is described by their mutual work.

4.2.3. *Chebyshev Polynomial Series Representation of the Displacement and Acoustic Pressure and the Solution Procedure*

In applying the Rayleigh–Ritz approach to free vibration analysis of the structural-acoustic system, each mode shape are approximated by a combination of a finite number of admissible functions [31]. The admissible functions are a set of orthogonal polynomial functions satisfying the geometric and boundary conditions. Since the arbitrary boundary conditions of the plates and cavity have been given during the theoretical modelling, there is no need to explicitly satisfy the boundary conditions for the admissible functions at any given edges. This enables the selections of admissible function with respect to the structural domain and acoustic domain flexible. Additional requirement on the admissible selection includes that it has to be linearly independent in each direction and sufficiently smooth to be differentiable at any point of the considered system. However, while using the Fourier based expansion as admissible function for analysing the structure dynamics [84][94-95], the potential discontinuities existed and the corresponding functional subspace leads to the convergence problem along the boundaries. This defect will become more remarked when the energy transmission between the cavity and the plate, or the structural-acoustic is desired [12]. Extra supplementary terms are added into the Fourier series expression [9-10][12] [92][96-97] to overcome the discontinuous issues. This operation ensures the existence of corresponding functional subspace at the boundary. However, it also increases complexity of formulations and dimensions of system matrices. This shortcoming may be negligible if the considered configuration is simple, however, in some cases it will be exaggerated and inconvenient, for instance, when the considered model is complex.

In recent years, using Chebyshev polynomials of the first kind as the admissible function for structure dynamic becomes popular due to its excellence in the function approximation [11], rapid convergence, and better stability in numerical operation [12]. It has been proven on the cases of stepped beam [98], annular sector plates [99], laminate beams [100], rectangular plates with cutout [101], functionally graded material

[102]. It has also applied to solve the acoustic problem [93] and structural-acoustic interaction [80] [88] [103]. The advantage of using a representation in terms of Chebyshev polynomials include:

- the requirement for periodic boundary conditions can be eliminate
- allowing for more freedom in the choice of approximation regions
- ensure the derivative of the functions at any given edges or surfaces exist and are continuous at any point of the solution domain.

In this thesis, Chebyshev polynomials of the first kind are employed as the admissible functions for modeling structural-acoustic system. The nth Chebyshev polynomial $T_n(x)$ indicates a polynomial in x of degree n is uniformly defined as [104]

$$T_n(x) = \cos(n \arccos x); \; (n = 0,1,2,K \; ; |x| \leq 1) \qquad [4\text{-}13]$$

The recurrence equations of the Chebyshev polynomials can be obtained base on the trigonometric relation $\cos[(n+1)\vartheta] + \cos[(n-1)\vartheta] = 2\cos\vartheta\cos n\vartheta$

$$T_{n+1}(x) = 2xT_n(x) - T_{n-1}(x). \qquad [4\text{-}14]$$

The general form of Chebyshev polynomial can be derived as

$$T_n(x) = \sum_{k=0}^{[n/2]} (-1)^k \frac{n!}{(2k)!(n-2k)!} x^{n-2k}(1-x^2)^k \qquad [4\text{-}15]$$

where $[n/2]$ means the integer part of $n/2$

Note that the Chebyshev polynomials are defined between -1 and 1. Therefore, the plate displacements and acoustic pressure described by the Cartesian coordinates (x_i, y_i) and (X, Y, Z) respectively, shall be mapped into the range [-1, 1]. For example, the plates i are mapped to the domain in $\alpha_i - \beta_i$ using the following coordinate transformations.

$$x_i = \frac{L_{i,x}(\alpha_i + 1)}{2} \; , \; y_i = \frac{L_{i,y}(\beta_i + 1)}{2} \qquad [4\text{-}16]$$

Similarly, real coordinates in a $L_X \times L_Y \times L_Z$ cavity are mapped into domain $\alpha - \beta - \varepsilon$ according to

$$X = \frac{L_X(\alpha + 1)}{2}, Y = \frac{L_Y(\beta + 1)}{2}, Z = \frac{L_Z(\varepsilon + 1)}{2} \qquad [4\text{-}17]$$

Base on the Ritz method, we approximate the displacement functions and pressure functions by a finite linear combination of the double and triplicate Chebyshev

polynomial series as follows.

$$w_i(\alpha_i, \beta_i) = \sum_{m=0}^{M} \sum_{n=0}^{N} A_{i,m,n} T_m(\alpha_i) T_n(\beta_i)$$ [4-18]

$$u_i(\alpha_i, \beta_i) = \sum_{m=0}^{M} \sum_{n=0}^{N} B_{i,m,n} T_m(\alpha_i) T_n(\beta_i)$$ [4-19]

$$v_i(\alpha_i, \beta_i) = \sum_{m=0}^{M} \sum_{n=0}^{N} C_{i,m,n} T_m(\alpha_i) T_n(\beta_i)$$ [4-20]

$$p(\alpha, \beta, \varepsilon) = \sum_{mx=0}^{M_X} \sum_{my=0}^{M_Y} \sum_{mz=0}^{M_Z} E_{mx,my,mz} T_{mx}(\alpha) T_{my}(\beta) T_{mz}(\varepsilon)$$ [4-21]

where $A_{i,m,n}$, $B_{i,m,n}$, $C_{i,m,n}$ and $E_{mx,my,mz}$ are the unknown coefficients of the Chebyshev expansions to be determined. And $T_{\Xi_i}(\chi)$ ($\Xi_i = m_i, n_i, mx, my, mz, \chi = \alpha_i, \beta_i, \alpha, \beta, \varepsilon$) is the one-dimensional Chebyshev polynomial of the first kind. The indices m, n, mx, my, mz indicates the m th, n th, m_x th, m_y th and m_z th order polynomial in the respective directions. A sufficiently large finite number of terms M, N, M_X, M_Y, and M_Z must be considered to obtain a converged solution, and the preferred choice of finite number changes with the problems complexity, the geometry of examined system, the frequency range of interest, etc.

Making the corresponding transformation in the Lagrangian equations yields

$$V_i^T = \frac{D_i L_{i,x} L_{i,y}}{8} \int_{-1}^{1} \int_{-1}^{1} \left[\begin{array}{c} \left(\frac{4\partial^2 w_i}{L_{i,x}^2 \partial \alpha_i^2} \right)^2 + \left(\frac{4\partial^2 w_i}{L_{i,y}^2 \partial \beta_i^2} \right)^2 + 32\upsilon_i \frac{\partial^2 w_i}{L_{i,x}^2 \partial \alpha_i^2} \frac{\partial^2 w_i}{L_{i,y}^2 \partial \beta_i^2} + \\ \frac{16(1-\upsilon_i)}{L_{i,x}^2 L_{i,y}^2} \left(\frac{\partial^2 w_i}{\partial \alpha_i \partial \beta_i} \right)^2 \end{array} \right] d\alpha_i d\beta_i$$ [4-22]

$$+ \frac{L_{i,y}}{4} \int_{-1}^{1} \left[k_{w\_x_i 0} w_i^2 + K_{w\_x_i 0} \left(\frac{2\partial w_i}{L_{i,x} \partial \alpha_i} \right)^2 \right]_{\alpha_i = -1} d\beta_i + \frac{L_{i,y}}{4} \int_{-1}^{1} \left[k_{w\_x_i 1} w_i^2 + K_{w\_x_i 1} \left(\frac{2\partial w_i}{L_{i,x} \partial \alpha_i} \right)^2 \right]_{\alpha_i = 1} d\beta_i$$

$$+ \frac{L_{i,x}}{4} \int_{-1}^{1} \left[k_{w\_y_i 0} w_i^2 + K_{w\_y_i 0} \left(\frac{2\partial w_i}{L_{i,y} \partial \beta_i} \right)^2 \right]_{\beta_i = -1} d\alpha_i + \frac{L_{i,x}}{4} \int_{-1}^{1} \left[k_{w\_y_i 1} w_i^2 + K_{w\_y_i 1} \left(\frac{2\partial w_i}{L_{i,y} \partial \beta_i} \right)^2 \right]_{\beta_i = 1} d\alpha_i$$

$$V_i^{In} = \frac{G_i L_{i,x} L_{i,y}}{8} \int_{-1}^{1}\int_{-1}^{1} \left[\begin{array}{l} \left(\dfrac{2\partial u_i}{L_{i,x}\partial \alpha_i} + \dfrac{2\partial v_i}{L_{i,y}\partial \beta_i} \right)^2 - \dfrac{8(1-\upsilon_i)}{L_{i,x}L_{i,y}} \dfrac{\partial u_i}{\partial \alpha_i}\dfrac{\partial v_i}{\partial \beta_i} + \\[4mm] \dfrac{(1-\upsilon_i)}{2}\left(\dfrac{2\partial u_i}{L_{i,y}\partial \beta_i} + \dfrac{2\partial v_i}{L_{i,x}\partial x_i} \right)^2 \end{array} \right] d\alpha_i d\beta_i$$

[4-23]

$$+ \frac{L_{i,y}}{4}\int_{-1}^{1}\left[k_{n\_x_i 0}u_i^2 + k_{p\_x_i 0}v_i^2\right]_{\alpha_i=-1}d\beta_i + \frac{L_{i,y}}{4}\int_{-1}^{1}\left[k_{n\_x_i 1}u_i^2 + k_{p\_x_i 1}v_i^2\right]_{\alpha_i=1}d\beta_i$$

$$+ \frac{L_{i,x}}{4}\int_{-1}^{1}\left[k_{n\_y_i 0}v_i^2 + k_{p\_y_i 0}u_i^2\right]_{\beta_i=-1}d\alpha_i + + \frac{L_{i,x}}{4}\int_{-1}^{1}\left[k_{n\_y_i 1}v_i^2 + k_{p\_y_i 1}u_i^2\right]_{\beta_i=1}d\alpha_i$$

$$T_i^T = \frac{L_{i,x}L_{i,y}}{8}\rho_{i,s}h_i\omega^2 \int_{-1}^{1}\int_{-1}^{1} w_i^2 d\alpha_i d\beta_i$$

[4-24]

$$T_i^{In} = \frac{L_{i,x}L_{i,y}}{8}\rho_{i,s}h_i\omega^2 \int_{-1}^{1}\int_{-1}^{1}\left(u_i^2 + v_i^2\right)d\alpha_i d\beta_i$$

[4-25]

$$W_1^{AS} = \frac{L_{1,x}L_{1,y}}{4}\int_{-1}^{1}\int_{-1}^{1} w_1(\alpha_1,\beta_1)p(\alpha_1,-1,\beta_1)d\alpha_1 d\beta_1$$

[4-26]

$$W_2^{AS} = \frac{L_{2,x}L_{2,y}}{4}\int_{-1}^{1}\int_{-1}^{1} w_2(\alpha_2,\beta_2)p(-1,\alpha_2,\beta_2)d\alpha_2 d\beta_2$$

$$W_5^{AS} = \frac{L_{5,x}L_{5,y}}{4}\int_{-1}^{1}\int_{-1}^{1} w_5(\alpha_5,\beta_5)p(\alpha_5,\beta_5,-1)d\alpha_5 d\beta_5$$

$$W_5^F = \frac{L_{i,x}L_{i,y}}{4}\int_{-1}^{1}\int_{-1}^{1} F_{5i}\delta w_5 d\alpha_5 d\beta_5$$

[4-27]

$$V_{15}^C = \frac{L_X}{4}\int_{-1}^{1}\left[\begin{array}{l} K_{c\_15}\left(\dfrac{2\partial w_1}{L_{1,y}\partial\beta_1}\Big|_{\beta_1=-1} - \dfrac{2\partial w_5}{L_{5,y}\partial\beta_5}\Big|_{\beta_5=-1} \right)^2 + k_{cw\_15}\left(w_1\big|_{\beta_1=-1} - v_5\big|_{\beta_5=-1}\right)^2 + \\[4mm] k_{cu\_15}\left(u_1\big|_{\beta_1=-1} + u_5\big|_{\beta_5=-1}\right)^2 + k_{cv\_15}\left(v_1\big|_{\beta_1=-1} - w_5\big|_{\beta_5=-1}\right)^2 \end{array} \right]d\alpha_1$$

[4-28]

$$V_{25}^C = \frac{L_Y}{4}\int_{-1}^{1}\left[\begin{array}{l} K_{c\_25}\left(\dfrac{2\partial w_2}{L_{2,y}\partial\beta_2}\Big|_{\beta_2=-1} - \dfrac{2\partial w_5}{L_{5,x}\partial\alpha_5}\Big|_{\alpha_5=-1} \right)^2 + k_{cw\_25}\left(w_2\big|_{\beta_2=-1} - u_5\big|_{\alpha_5=-1}\right)^2 + \\[4mm] k_{cu\_25}\left(u_2\big|_{\beta_2=-1} - v_5\big|_{\alpha_5=-1}\right)^2 + k_{cv\_25}\left(v_2\big|_{\beta_2=-1} - w_5\big|_{\alpha_5=-1}\right)^2 \end{array} \right]d\alpha_2$$

$$V_{12}^C = \frac{L_Z}{4}\int_{-1}^{1}\left[\begin{array}{l} K_{c\_12}\left(\dfrac{2\partial w_1}{L_{1,x}\partial\alpha_1}\Big|_{\alpha_1=-1} - \dfrac{2\partial w_2}{L_{2,x}\partial\alpha_2}\Big|_{\alpha_2=1} \right)^2 + k_{cw\_12}\left(w_1\big|_{\alpha_1=-1} + u_2\big|_{\alpha_2=1}\right)^2 + \\[4mm] k_{cu\_12}\left(u_1\big|_{\alpha_1=-1} - w_2\big|_{\alpha_2=1}\right)^2 + k_{cv\_12}\left(v_1\big|_{\alpha_1=-1} + v_2\big|_{\alpha_2=1}\right)^2 \end{array} \right]d\beta_1$$

$$V_I^A = \frac{L_X L_Y L_Z}{16\rho_0 c_0^2} \int\limits_{-1}^{1}\int\limits_{-1}^{1}\int\limits_{-1}^{1} p^2 \, d\alpha d\beta d\varepsilon \qquad [4\text{-}29]$$

$$T_I^A = \frac{L_X L_Y L_Z}{16\rho_0 \omega^2} \int\limits_{-1}^{1}\int\limits_{-1}^{1}\int\limits_{-1}^{1}\left[\left(\frac{2\partial p}{L_X \partial \alpha}\right)^2 + \left(\frac{2\partial p}{L_Y \partial \beta}\right)^2 + \left(\frac{2\partial p}{L_Z \partial \varepsilon}\right)^2\right] d\alpha d\beta d\varepsilon \qquad [4\text{-}30]$$

$$W_A^P = \frac{L_X L_Y L_Z}{16\rho_0 \omega^2} \int\limits_{-1}^{1}\int\limits_{-1}^{1}\int\limits_{-1}^{1} p(\alpha,\beta,\varepsilon) Q(\alpha,\beta,\varepsilon) \, d\alpha d\beta d\varepsilon \qquad [4\text{-}31]$$

Substituting equation [4-18] to [4-21] in to the Lagrangians, [4-1] and [4-9], and applying the Rayleigh-Ritz procedure against each of the unknown displacement coefficients $A_{i,m,n}$, $B_{i,m,n}$, $C_{i,m,n}$ and pressure unknown coefficient $E_{mx,my,mz}$ equal zero [105],

$$\frac{d}{dt}\left(\frac{d\mathbf{L}}{d\mathbf{H}}\right) - \frac{d\mathbf{L}}{d\mathbf{H}} = 0 \qquad [4\text{-}32]$$

where $\mathbf{H}$ is the unknown coefficient matrix. the characteristic equation of the coupled plates can be derived in a matrix form as

$$\begin{bmatrix} \mathbf{K}_S & \mathbf{C_{SA}}^T \\ 0 & \mathbf{K}_A \end{bmatrix}\begin{bmatrix} \mathbf{\Theta} \\ \mathbf{\Omega} \end{bmatrix} - \omega^2 \begin{bmatrix} \mathbf{M}_S & 0 \\ -\mathbf{C_{SA}} & \mathbf{M}_A \end{bmatrix}\begin{bmatrix} \mathbf{\Theta} \\ \mathbf{\Omega} \end{bmatrix} = \begin{Bmatrix} \mathbf{F} \\ \mathbf{P} \end{Bmatrix} \qquad [4\text{-}33]$$

where subscripts S and A denote that the variables are related to the structure and cavity respectively. $\mathbf{M}$ and $\mathbf{K}$ are the generalised global mass and stiffness matrices. The stiffness matrices of the structure domain $\mathbf{K}_S$ is formed by the transverse component $\mathbf{K}_i^T$, four in-plane components $\mathbf{K}_i^U, \mathbf{K}_i^V, \mathbf{K}_i^{UV}, \mathbf{K}_i^{VU}$, and structural coupling components $\mathbf{K}^C$ as

$$\mathbf{K}_S = \begin{bmatrix} \mathbf{K}_1^T & 0 & 0 & 0 & 0 & 0 & 0 \\ 0 & \mathbf{K}_1^U & \mathbf{K}_1^{UV} & 0 & 0 & 0 & 0 \\ 0 & \mathbf{K}_1^{VU} & \mathbf{K}_1^V & 0 & 0 & 0 & 0 \\ 0 & 0 & 0 & \mathrm{O} & 0 & 0 & 0 \\ 0 & 0 & 0 & 0 & \mathbf{K}_{18}^T & 0 & 0 \\ 0 & 0 & 0 & 0 & 0 & \mathbf{K}_{18}^U & \mathbf{K}_{18}^{UV} \\ 0 & 0 & 0 & 0 & 0 & \mathbf{K}_1^{VU} & \mathbf{K}_{18}^V \end{bmatrix} + \begin{bmatrix} \mathbf{K}_{1-1}^C & \mathbf{K}_{1-2}^C & \mathrm{L} & \mathbf{K}_{1-18}^C \\ \mathbf{K}_{2-1}^C & \mathbf{K}_{2-2}^C & \mathrm{L} & \mathbf{K}_{2-18}^C \\ \mathrm{M} & \mathrm{M} & \mathrm{O} & \mathrm{M} \\ \mathbf{K}_{18-1}^C & \mathbf{K}_{18-2}^C & \mathrm{L} & \mathbf{K}_{18-18}^C \end{bmatrix} \qquad [4\text{-}34]$$

The structure mass matrix $\mathbf{M_S}$ is expressed as

$$\mathbf{M_S} = \mathrm{diag}\{\mathbf{M}_1 \quad \mathbf{M}_1 \quad \mathbf{M}_1 \quad \Lambda \quad \mathbf{M}_6 \quad \mathbf{M}_6 \quad \mathbf{M}_6\} \qquad [4\text{-}35]$$

The structure-acoustic coupling term $\mathbf{C_{SA}}$ is expressed as

64

$$\mathbf{C}_{SA} = \begin{bmatrix} \mathbf{C}_{1-1}^T & \mathbf{0} & \mathbf{0} & \mathbf{C}_{1-4}^T & \mathbf{0} & \mathbf{0} & \mathbf{K} & \mathbf{C}_{16}^T & \mathbf{0} & \mathbf{0} \end{bmatrix}^T \qquad [4\text{-}36]$$

The $\mathbf{\Omega}$ and $\mathbf{\Gamma}$ are the generalised pressure vector and displacement vector. $\mathbf{\Theta}$ is given as: $\mathbf{\Theta} = [\mathbf{a}_1, \mathbf{b}_1, \mathbf{c}_1, \mathbf{a}_2, \mathbf{b}_2, \mathbf{c}_2, ... \mathbf{a}_6, \mathbf{b}_6, \mathbf{c}_6]^T$. The particular expression of coefficient matrix for $\mathbf{a}_i$, $\mathbf{b}_i$, $\mathbf{c}_i$ and $\mathbf{\Omega}$ are given below

$$\mathbf{a_i} = \{A_{i,0,0}, A_{i,0,1}, \mathrm{K} \; A_{i,m,0}, A_{i,m,1}, \mathrm{K} \; A_{i,m,n}, \mathrm{K}, A_{i,M,N}\}^T \qquad [4\text{-}37]$$

$$\mathbf{b_i} = \{B_{i,0,0}, B_{i,0,1}, \mathrm{K} \; B_{i,m,0}, B_{i,m,1}, \mathrm{K} \; B_{i,m,n}, \mathrm{K}, B_{i,M,N}\}^T \qquad [4\text{-}38]$$

$$\mathbf{c_i} = \{C_{i,0,0}, C_{i,0,1}, \mathrm{K} \; C_{i,m,0}, C_{i,m,1}, \mathrm{K} \; C_{i,m,n}, \mathrm{K}, C_{i,M,N}\}^T \qquad [4\text{-}39]$$

$$\mathbf{\Omega} = [E_{0,0,0}, E_{0,0,1}, \mathrm{K}, E_{0,0,MZ}, E_{0,1,0}, \mathrm{K}, E_{0,1,MZ}, \mathrm{K}, E_{0,MY,MZ}, \mathrm{K}, E_{MX,MY,MZ}]^T \qquad [4\text{-}40]$$

The external loading vector $\mathbf{F}$ and $\mathbf{P}$ originated by the point force and interior acoustic excitation respectively. Define

$$[F_i]_{(\xi)} = F \cdot T_m(\alpha_i) \cdot T_n(\beta_i) \qquad [4\text{-}41]$$

$$[P]_{(\eta)} = P \cdot T_{mx}(\alpha) \cdot T_{my}(\beta) \cdot T_{mz}(\gamma) \qquad [4\text{-}42]$$

Define the $g, \bar{g} = 0,1$, $l, \bar{l} = 0,1,2$ and $\eta = mx \cdot my \cdot mz$, $\gamma = \overline{mx} \cdot \overline{mx} \cdot \overline{mz}$, $\xi = m \cdot n$, $\psi = \overline{m} \cdot \overline{n}$

$$\Xi_{I,mx,\overline{mx}}^{g,\bar{g}} = \int_{-1}^{1} \frac{\mathrm{d}^g T_{mx}^g}{L_{I,X}^g \mathrm{d}\alpha_I^g} \cdot \frac{\mathrm{d}^{\bar{g}} T_{mx}^{\bar{g}}}{L_{I,X}^{\bar{g}} \mathrm{d}\alpha_I^{\bar{g}}} d\alpha_I \qquad [4\text{-}43]$$

$$\Psi_{I,my,\overline{my}}^{g,\bar{g}} = \int_{-1}^{1} \frac{\mathrm{d}^g T_{my}^g}{L_{I,Y}^g \mathrm{d}\beta_I^g} \cdot \frac{\mathrm{d}^{\bar{g}} T_{my}^{\bar{g}}}{L_{I,Y}^{\bar{g}} \mathrm{d}\beta_I^{\bar{g}}} d\beta_I$$

$$Y_{I,mz,\overline{mz}}^{g,\bar{g}} = \int_{-1}^{1} \frac{\mathrm{d}^g T_{mz}^g}{L_{I,Z}^g \mathrm{d}\varepsilon_I^g} \cdot \frac{\mathrm{d}^{\bar{g}} T_{mz}^{\bar{g}}}{L_{I,Z}^{\bar{g}} \mathrm{d}\varepsilon_I^{\bar{g}}} d\varepsilon_I$$

$$\varsigma_{i,m,\overline{m}}^{l,\bar{l}} = \int_{-1}^{1} \frac{\mathrm{d}^l T_m^l}{L_{i,x}^l \mathrm{d}\alpha_i^l} \cdot \frac{\mathrm{d}^{\bar{l}} T_{\overline{m}}^{\bar{l}}}{L_{i,x}^{\bar{l}} \mathrm{d}\alpha_i^{\bar{l}}} d\alpha_i \qquad [4\text{-}44]$$

$$\psi_{i,n,\overline{n}}^{l,\bar{l}} = \int_{-1}^{1} \frac{\mathrm{d}^l T_n^l}{L_{i,y}^l \mathrm{d}\beta_i^l} \cdot \frac{\mathrm{d}^{\bar{l}} T_{\overline{n}}^{\bar{l}}}{L_{i,y}^{\bar{l}} \mathrm{d}\beta_i^{\bar{l}}} d\beta_i$$

$$T_{i,m}^{'} = \frac{dT_m(\alpha_i)}{d\alpha_i}$$

The elements of all sub matrices for the cavity, structure, and their coupling effects are written as follows. $[K_A]_{(\eta, \gamma)}$ $[M_A]_{(\eta, \gamma)}$ $[K_i^T]_{(\xi, \psi)}$ $[K_i^U]_{(\xi, \psi)}$ $[K_i^V]_{(\xi, \psi)}$ $[K_i^{UV}]_{(\xi, \psi)}$ $[K_i^{VU}]_{(\xi, \psi)}$ $[K_i^{VU}]_{(\xi, \psi)}$ and $[M_i^S]_{(\xi, \psi)}$ can be calculated according to the following formulae:

$$[K_A]_{(\eta,\gamma)} = -\frac{L_X L_Y L_Z}{2\rho_0}(\Xi^{1,1}_{mx,\overline{mx}}\Psi^{0,0}_{my,\overline{my}}Y^{0,0}_{mz,\overline{mz}} + \Xi^{0,0}_{mx,\overline{mx}}\Psi^{1,1}_{my,\overline{my}}Y^{0,0}_{mz,\overline{mz}} + \Xi^{0,0}_{mx,\overline{mx}}\Psi^{0,0}_{my,\overline{my}}Y^{1,1}_{mz,\overline{mz}})$$

[4-45]

$$[M_A]_{(\eta,\gamma)} = -\frac{L_X L_Y L_Z}{8\rho_0 c_0^2}\Xi^{0,0}_{mx,\overline{mx}}\Psi^{0,0}_{my,\overline{my}}Y^{0,0}_{mz,\overline{mz}}$$

[4-46]

$$\left[K_i^T\right]_{(\lambda,\tau))} = 4D_i L_{i,x} L_{i,y}\left[\begin{array}{l}\psi^{0,0}_{i,n,\overline{n}}\cdot\xi^{2,2}_{i,m,\overline{m}} + \psi^{2,2}_{i,n,\overline{n}}\cdot\xi^{0,0}_{i,m,\overline{m}} + \upsilon_i\cdot\psi^{0,2}_{i,n,\overline{n}}\cdot\xi^{2,0}_{i,m,\overline{m}} + \\ \upsilon_i\cdot\psi^{2,0}_{i,n,\overline{n}}\cdot\xi^{0,2}_{i,m,\overline{m}} + 2(1-\upsilon_i)\cdot\psi^{1,1}_{i,n,\overline{n}}\cdot\xi^{1,1}_{i,m,\overline{m}}\end{array}\right] +$$

[4-47]

$$\psi^{0,0}_{i,n,\overline{n}}\left[\frac{L_{i,y}\cdot k_{w\_x_i0}}{2}T_m(-1)T_{\overline{m}}(-1) + \frac{2L_{i,y}\cdot K_{w\_x_i0}}{L_{i,x}^2}T_{i,m}(-1)'T_{i,\overline{m}}(-1)'\right] +$$

$$\psi^{0,0}_{i,n,\overline{n}}\left[\frac{L_{i,y}\cdot k_{w\_x_i1}}{2}T_m(1)T_{\overline{m}}(1) + \frac{2L_{i,y}\cdot K_{w\_x_i1}}{L_{i,x}^2}T_{i,m}(1)'T_{i,\overline{m}}(1)'\right] +$$

$$\xi^{0,0}_{i,m,\overline{m}}\left[\frac{L_{i,x}\cdot k_{w\_y_i0}}{2}T_n(-1)T_{\overline{n}}(-1) + \frac{2L_{i,x}\cdot K_{w\_y_i0}}{L_{i,y}^2}T_{i,n}(-1)'T_{i,\overline{n}}(-1)'\right] +$$

$$\xi^{0,0}_{i,m,\overline{m}}\left[\frac{L_{i,x}\cdot k_{w\_y_i1}}{2}T_n(1)T_{\overline{n}}(1) + \frac{2L_{i,x}\cdot K_{w\_y_i1}}{L_{i,y}^2}T_{i,n}(1)'T_{i,\overline{n}}(1)'\right]$$

$$\left[K_i^U\right]_{(\lambda,\tau)} = \frac{G_i L_{i,x} L_{i,y}}{4}\left[\xi^{1,1}_{i,m,\overline{m}}\cdot\psi^{0,0}_{i,n,\overline{n}} + \frac{(1-\upsilon_i)}{2}\xi^{0,0}_{i,m,\overline{m}}\cdot\psi^{1,1}_{i,n,\overline{n}}\right] +$$

[4-48]

$$\frac{L_{i,y}\psi^{0,0}_{i,n,\overline{n}}}{2}\left[k_{n\_x_i0}T_m(-1)T_{\overline{m}}(-1) + k_{n\_x_i1}T_{i,m}(1)T_{\overline{m}}(1)\right] +$$

$$\frac{L_{i,x}\xi^{0,0}_{i,m,\overline{m}}}{2}\left[k_{p\_y_i0}T_n(-1)T_{\overline{n}}(-1) + k_{p\_y_i1}T_n(1)T_{\overline{n}}(1)\right]$$

$$\left[K_i^V\right]_{(\lambda,\tau))} = \frac{G_i L_{i,x} L_{i,y}}{4}\left[\xi^{0,0}_{i,m,\overline{m}}\cdot\psi^{1,1}_{i,n,\overline{n}} + \frac{(1-\upsilon_i)}{2}\xi^{1,1}_{i,m,\overline{m}}\cdot\psi^{0,0}_{i,n,\overline{n}}\right] +$$

[4-49]

$$\frac{L_{i,y}\psi^{0,0}_{i,n,\overline{n}}}{2}\left[k_{p\_x_i0}T_m(-1)T_{\overline{m}}(-1) + k_{p\_x_i1}T_m(1)T_{\overline{m}}(1)\right] +$$

$$\frac{L_{i,x}\xi^{0,0}_{i,m,\overline{m}}}{2}\left[k_{n\_y_i0}T_n(-1)T_{\overline{n}}(-1) + k_{n\_y_i1}T_n(1)T_{\overline{n}}(1)\right]$$

$$\left[K_i^{UV}\right]_{(\lambda,\tau)} = \frac{G_i L_{i,x} L_{i,y}}{4}\left[\upsilon_i\xi^{1,0}_{i,m,\overline{m}}\cdot\psi^{0,1}_{i,n,\overline{n}} + \frac{(1-\upsilon_i)}{2}\xi^{0,1}_{i,m,\overline{m}}\cdot\psi^{1,0}_{i,n,\overline{n}}\right]$$

[4-50]

$$\left[K_i^{VU}\right]_{(\lambda,\tau)} = \frac{G_i L_{i,x} L_{i,y}}{4}\left[\upsilon_i\xi^{0,1}_{i,m,\overline{m}}\cdot\psi^{1,0}_{i,n,\overline{n}} + \frac{(1-\upsilon_i)}{2}\xi^{1,0}_{i,m,\overline{m}}\cdot\psi^{0,1}_{i,n,\overline{n}}\right]$$

[4-51]

$$\left[M_i^S\right]_{(\lambda,\tau)} = \frac{\rho_{i,s}h_i L_{i,x} L_{i,y}}{4}\xi^{0,0}_{i,m,\overline{m}}\cdot\psi^{0,0}_{i,n,\overline{n}}$$

[4-52]

The sub-matrices $\left[C^{SA}\right]_{(\eta,\lambda)}$ and $\left[K^C\right]_{(\lambda,\tau)}$ are relating to the plate's orientation. The sub-matrices of the structure-acoustic coupling term $\mathbf{C_{SA}}$ are expressed as

$$\left[C_{1-1}^{SA}\right]_{(\eta,\xi)} = \frac{L_X L_Z}{4} \xi_{1,mx,m}^{0,0} \cdot \gamma_{1,mz,n}^{0,0} \cdot T_{my}(-1), \left[C_{1-4}^{SA}\right]_{(\eta,\xi)} = \frac{L_Y L_Z}{4} \xi_{2,mx,m}^{0,0} \cdot \psi_{2,my,n}^{0,0} \cdot T_{mx}(-1), \qquad [4\text{-}53]$$

$$\left[C_{1-7}^{SA}\right]_{(\eta,\xi)} = \frac{L_X L_Z}{4} \xi_{3,mx,m}^{0,0} \cdot \gamma_{3,mz,n}^{0,0} \cdot T_{my}(1), \left[C_{1-10}^{SA}\right]_{(\eta,\xi)} = \frac{L_Y L_Z}{4} \xi_{4,mx,m}^{0,0} \cdot \psi_{4,my,n}^{0,0} \cdot T_{mx}(1),$$

$$\left[C_{1-13}^{SA}\right]_{(\eta,\xi)} = \frac{L_X L_Z}{4} \xi_{5,mx,m}^{0,0} \cdot \psi_{5,my,n}^{0,0} \cdot T_{mz}(-1), \left[C_{1-16}^{SA}\right]_{(\eta,\xi)} = \frac{L_X L_Z}{4} \xi_{6,mx,m}^{0,0} \cdot \psi_{6,my,n}^{0,0} \cdot T_{mz}(1)$$

The first row of the structural coupling term $\mathbf{K}_{ij}^C$ are presented as

$$\left[K_{1-1}^{C}\right]_{(\lambda,\tau)} = \frac{2L_{Z}K_{c\_12}}{L_{X}^{2}} \cdot T_{1,m}^{'}(-1) \cdot T_{1,\overline{m}}^{'}(-1) \cdot \psi_{1,n,\overline{n}}^{0,0} + \frac{2L_{Z}K_{c\_14}}{L_{X}^{2}} \cdot T_{1,m}^{'}(1) \cdot T_{1,\overline{m}}^{'}(1) \cdot \psi_{1,n,\overline{n}}^{0,0} + \qquad \begin{array}{l}[4\text{-}54\\ ]\end{array}$$

$$\frac{2L_{X}K_{c\_15}}{L_{Z}^{2}} \cdot T_{1,n}^{'}(-1) \cdot T_{1,\overline{n}}^{'}(-1) \cdot \xi_{1,m,\overline{m}}^{0,0} + \frac{2L_{X}K_{c\_16}}{L_{Z}^{2}} \cdot T_{1,n}^{'}(1) \cdot T_{1,\overline{n}}^{'}(1) \cdot \xi_{1,m,\overline{m}}^{0,0} +$$

$$\left[\frac{L_{Z}k_{cw\_12}}{2}T_{m}(-1)T_{\overline{m}}(-1) + \frac{L_{Z}k_{cw\_14}}{2}T_{m}(1)T_{\overline{m}}(1)\right]\psi_{1,n,\overline{n}}^{0,0} +$$

$$\left[\frac{L_{X}k_{cw\_15}}{2}T_{n}(-1)T_{\overline{n}}(-1) + \frac{L_{X}k_{cw\_16}}{2}T_{n}(1)T_{\overline{n}}(1)\right]\xi_{1,m,\overline{m}}^{0,0}$$

$$\left[K_{1-4}^{C}\right]_{(\lambda,\tau)} = -\frac{2L_{Z}K_{c\_12}}{L_{X}L_{Y}} \cdot \left(\frac{dT_{m}(\alpha_{1})}{d\alpha_{1}} \cdot \frac{d^{0}T_{\overline{m}}^{0}(\alpha_{1})}{d\alpha_{1}^{0}}\bigg|_{\alpha_{1}=-1}\right) \cdot \left(\frac{dT_{m}(\alpha_{2})}{d\alpha_{2}} \cdot \frac{d^{0}T_{\overline{m}}^{0}(\alpha_{2})}{d\alpha_{2}^{0}}\bigg|_{\alpha_{2}=1}\right) \cdot$$

$$\psi_{1,n,\overline{n}}^{0,0} \cdot \psi_{2,n,\overline{n}}^{0,0}$$

$$\left[K_{1-5}^{C}\right]_{(\lambda,\tau)} = \frac{L_{Z}L_{cw\_12}}{2}T_{m}(-1) \cdot T_{\overline{m}}(1) \cdot \psi_{1,n,\overline{n}}^{0,0}$$

$$\left[K_{1-10}^{C}\right]_{(\lambda,\tau)} = -\frac{2L_{Z}K_{c\_14}}{L_{X}L_{Y}} \cdot \left(\frac{dT_{m}(\alpha_{1})}{d\alpha_{1}} \cdot \frac{d^{0}T_{\overline{m}}^{0}(\alpha_{1})}{d\alpha_{1}^{0}}\bigg|_{\alpha_{1}=1}\right) \cdot \left(\frac{dT_{m}(\alpha_{4})}{d\alpha_{4}} \cdot \frac{d^{0}T_{\overline{m}}^{0}(\alpha_{4})}{d\alpha_{4}^{0}}\bigg|_{\alpha_{4}=1}\right) \cdot \psi_{1,n,\overline{n}}^{0,0} \cdot \psi_{4,n,\overline{n}}^{0,0}$$

$$\left[K_{1-11}^{C}\right]_{(\lambda,\tau)} = -\frac{L_{Z}L_{cw\_14}}{2}T_{m}(1) \cdot T_{\overline{m}}(-1) \cdot \psi_{1,n,\overline{n}}^{0,0}$$

$$\left[K_{1-13}^{C}\right]_{(\lambda,\tau)} = -\frac{2L_{X}K_{c\_15}}{L_{Z}L_{Y}} \cdot \left(\frac{dT_{n}(\beta_{1})}{d\beta_{1}} \cdot \frac{d^{0}T_{\overline{n}}^{0}(\beta_{1})}{d\beta_{1}^{0}}\bigg|_{\beta_{1}=-1}\right) \cdot \left(\frac{dT_{n}(\beta_{5})}{d\beta_{4}} \cdot \frac{d^{0}T_{\overline{n}}^{0}(\beta_{5})}{d\beta_{5}^{0}}\bigg|_{\beta_{5}=-1}\right)$$

$$\cdot \xi_{1,m,\overline{m}}^{0,0} \cdot \xi_{5,m,\overline{m}}^{0,0}$$

$$\left[K_{1-15}^{C}\right]_{(\lambda,\tau)} = -\frac{L_{X}L_{cw\_15}}{2}T_{n}(-1) \cdot T_{\overline{n}}(-1) \cdot \xi_{1,m,\overline{m}}^{0,0}$$

$$\left[K_{1-16}^{C}\right]_{(\lambda,\tau)} = -\frac{2L_{X}K_{c\_16}}{L_{Z}L_{Y}} \cdot \left(\frac{dT_{n}(\beta_{1})}{d\beta_{1}} \cdot \frac{d^{0}T_{\overline{n}}^{0}(\beta_{1})}{d\beta_{1}^{0}}\bigg|_{\beta_{1}=1}\right) \cdot \left(\frac{dT_{n}(\beta_{6})}{d\beta_{6}} \cdot \frac{d^{0}T_{\overline{n}}^{0}(\beta_{6})}{d\beta_{6}^{0}}\bigg|_{\beta_{6}=-1}\right)$$

$$\cdot \xi_{1,m,\overline{m}}^{0,0} \cdot \xi_{6,m,\overline{m}}^{0,0}$$

$$\left[K_{1-18}^{C}\right]_{(\lambda,\tau)} = -\frac{L_{X}L_{cw\_16}}{2}T_{n}(1) \cdot T_{\overline{n}}(-1) \cdot \xi_{1,m,\overline{m}}^{0,0}$$

The free vibration problem for the structure-acoustic coupled system can be easily solved by assuming harmonic motion and removing the external load **F** and **P** from equation [4-33]. The response of sound pressure and external load can be obtained by solving equation [4-33]

and back-substituting corresponding coefficients into the expression of the sound pressure and plate displacements.

With the theoretical modeling and solution procedure described above, model validation and numerical analysis will be conducted in the following. Firstly, model validation will be performed to demonstrate the reliability and accuracy of the current method in predicting the natural frequencies and responses. With the verified model, studies are easily conducted to evaluate the impact of plate coupling manner and the influences of the medium on the plate displacement and the pressure response. The presented results ignor all zero-natural frequency corresponding to the rigid-body mode of the system.

4.3.   Results and discussions

4.3.1.   Model Verification

The present analytical model is verified by comparing both the free and forced vibration solutions of the rigidly coupled model with the FEM results. The model is composed of six rectangular plates rigidly coupled with the same thickness $h = 2.5mm$. These plates are made of aluminum and have identical material properties: Young's modulus $E = 71\,\mathrm{GPa}$, Poisson's ratio $\upsilon = 0.3$, and density $\rho_s = 2700\mathrm{kg/m^3}$. The air-filled box model occupying the space $L_X \times L_Y \times L_Z = 0.5\mathrm{m} \times 0.4\mathrm{m} \times 0.3\mathrm{m}$. L_Z . The air density and the speed of sound are $\rho_{air} = 1.21\,\mathrm{kg/m^3}$ and $c_0 = 340\,\mathrm{m/s}$. Refer to figure 4.2, Plate #5 is assumed to be clamped at two edges $\left(L_{5,x} = 0, L_{5,x} = L_X\right)$ along $Y - \mathrm{axis}$, while the rest of boundary edges are not constraint. The comparison is conducted in the frequency range up to 500 Hz. The verification finite element model is built with software Hyperwork using a $10mm \times 10mm$ Shell element and a $10mm \times 10mm \times 10mm$ solid elements for the plate and acoustic components, respectively, thus the FEM results are accurate enough to be as a reference. By truncating the series of structural domain and acoustic domain to 12 and 8, respectively, the difference between the current and the FEM results throughout the whole range is acceptable, with the maximum value of about 5 Hz as shown in figure 4.3.
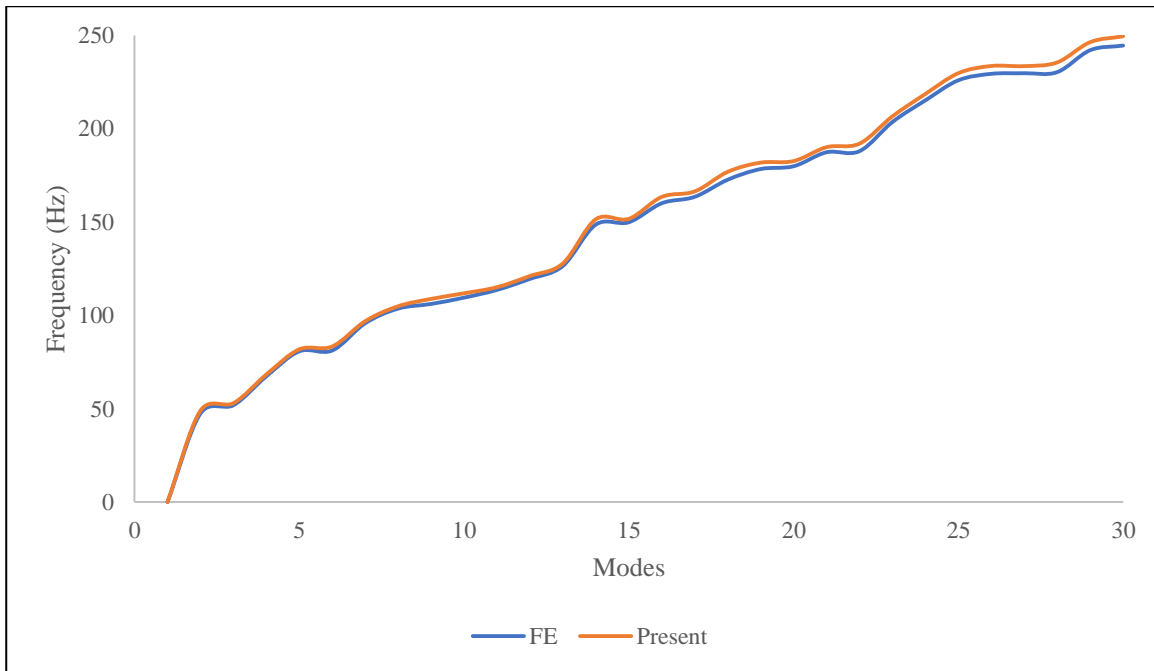
Figure 4.3 Comparison of natural frequencies between the present method and the FEA

The dynamic behavior of the rigidly coupled model is also examined by locating a concentrated point force at the center of plate #5 with unit amplitude of 100N. Since the plate #6 is not directly in contact with the source plate #5, verify the response on the plate #6 can examine both the vibration transmission and structure-acoustic interaction within the system. In addition, a receiver point at the cavity center is selected to verify the pressure response due to the force excitation.

The transverse and in-plane velocity response at the center of plate #6 are plotted in the figure 4.4(a). Although there are 31 natural frequencies within the range of 0 Hz to 250 Hz, only a few of them are excited to form the resonant peaks due to the excitation transmitted from the bottom plate #5. It is observed that these curves match quite well except a little difference occur at some peaks and a bit frequency-shift above 150 Hz. Figure 4.4(b) compares the acoustic pressure response between the present method and FEM calculation. The present results are found to be agreed well with the FEM results throughout the frequency range of interest. In general, the results show that the present method is reliable and capable of handling a system exhibiting coupling between the plate-plate and plate-cavity.
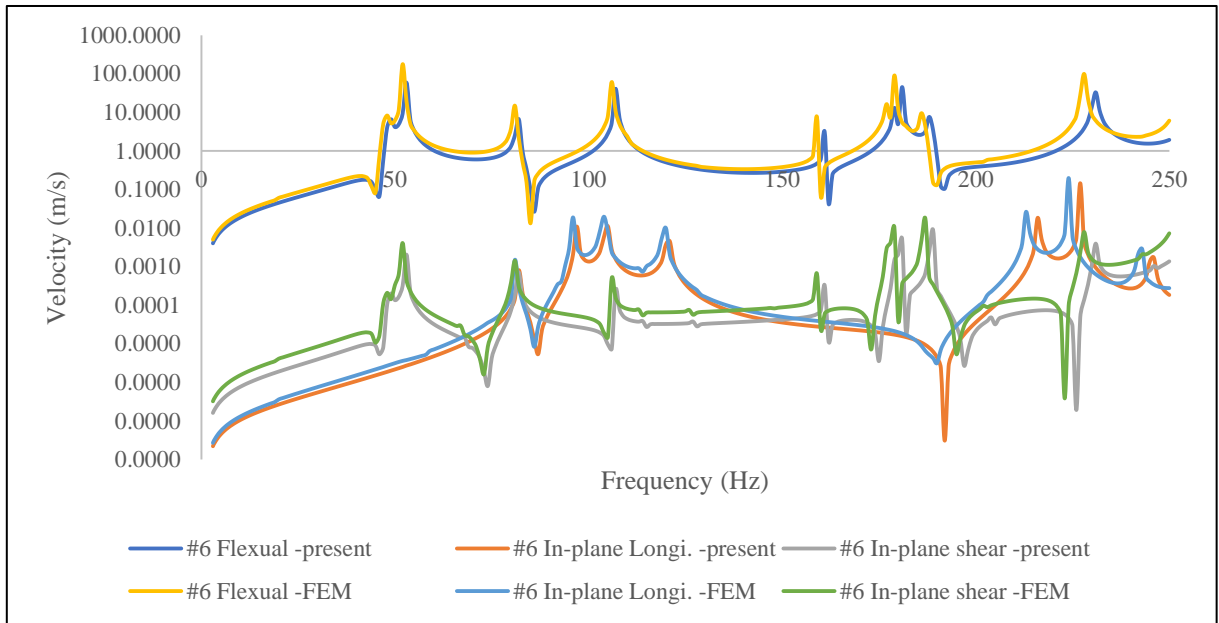
(a) Displacement response at plate #6 center
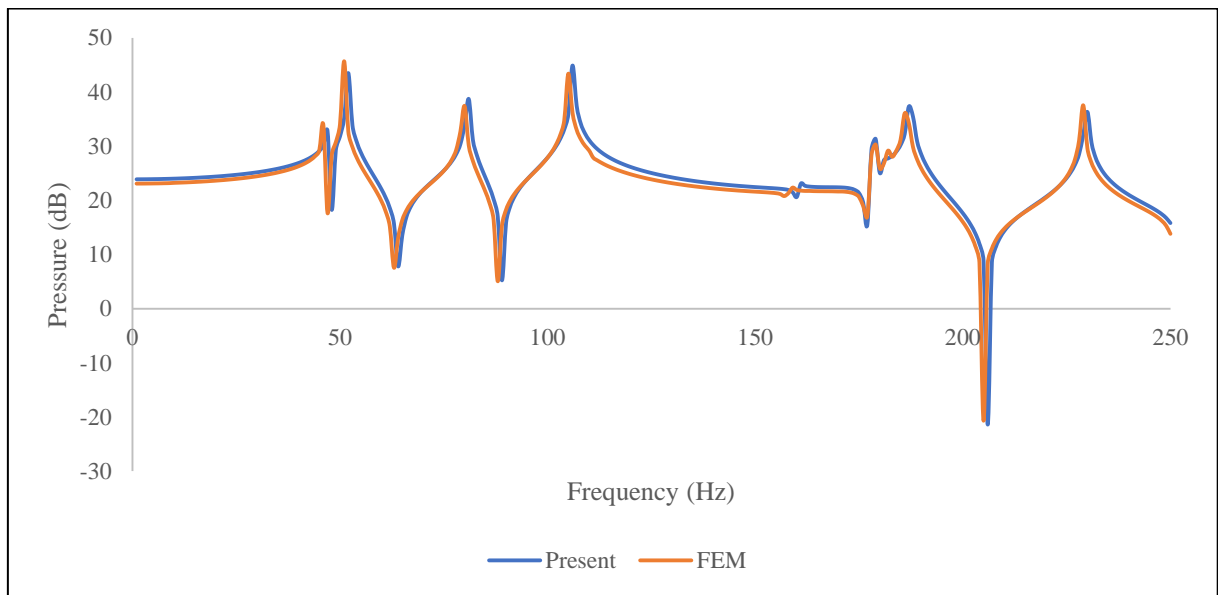
(b) Pressure response at the cavity center

Figure 4.4 Calculated dynamic responses validate with FEA results

4.3.2. The effect of structural coupling

From the viewpoint of structural vibration, the coupling manner can significantly affect the modal properties of structure domain. This model can tell how this manner affecting the overall structural-acoustic system does. Changing the coupling stiffness values to zero disable the connectivity from plate to plate, thus, each boundary plate is only restrained by own boundary springs. By doing this, the rest plates would not be receiving vibration energy from

the source plate, so that the configuration transformed into a model proposed by reference [19].

Figure 4.5(a) illustrates the comparison of the transverse and in-plane velocity responses at plate #6 center for the structural domain under rigid coupling and disconnected conditions within the frequency range 0 Hz to 250 Hz. the velocity amplitudes of plate #6 in all directions are promoted after being rigidly connected with the adjacent plates, expeically the in-plane vibrations. For the reason that, acoustic domain influences plate vibration in transverse direction, whereas the in-plane velocities can only be induced by the vibration energy transmitted from the neighboring plates.

The pressure response comparison at the cavity center is plotted in the figure 4.5(b). Its's interesting to see that the although the peak amplitude does not increase significantly after rigidly connect all plates, more resonance peak appeared within the interest frequency range. This case explains the importance of involving structural couplings for offshore platform vibro-acoustic studies. Mistakes can be made if the coupling effects are eliminated. With present model, some preliminary estimations can be obtained to evaluate the effectiveness of the selected noise control strategy.
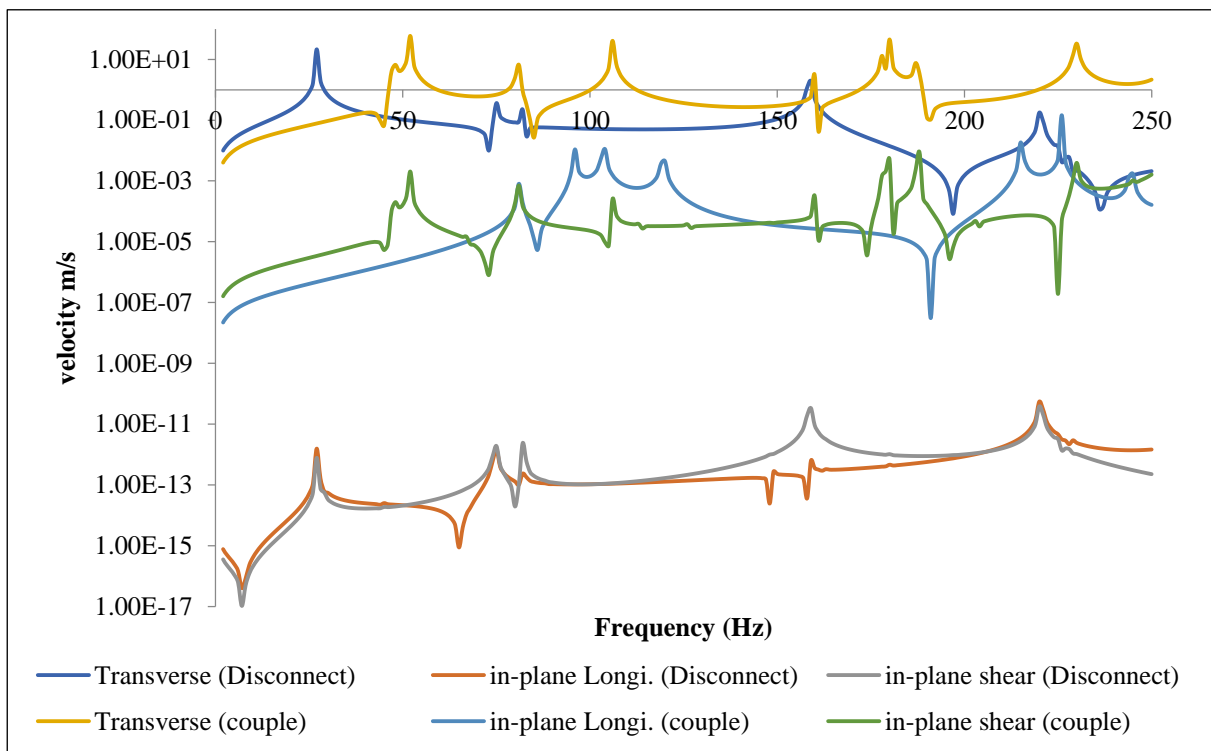
(a) Displacement response at plate #6 center
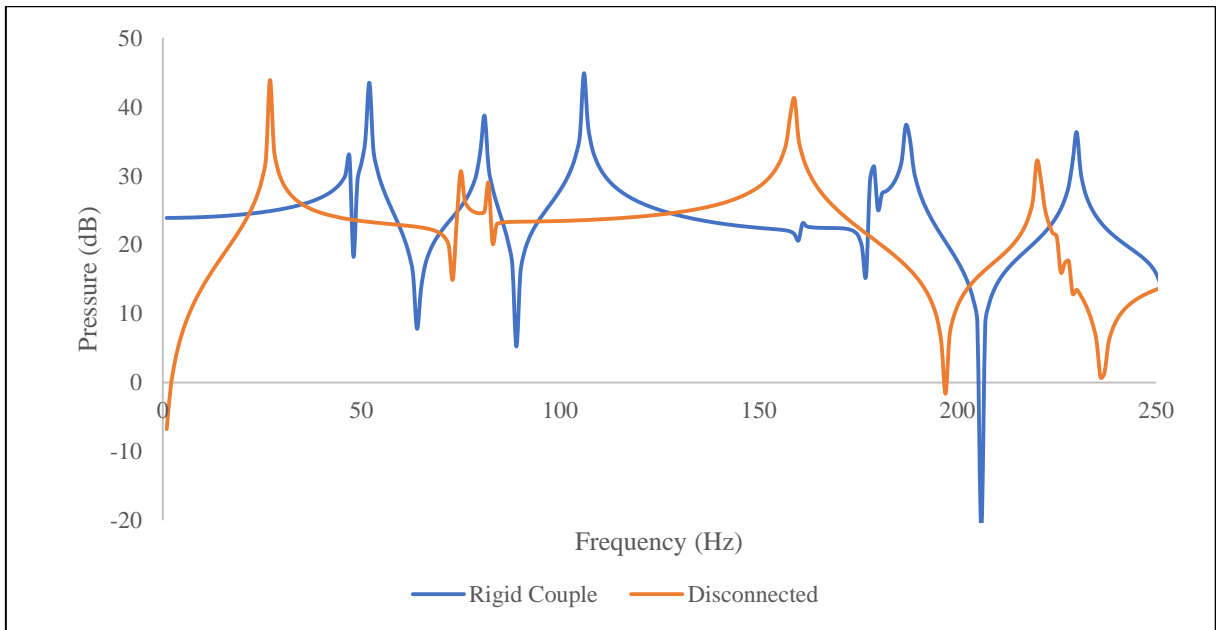
(b) Pressure response at the cavity center

Figure 4.5 Response comparison for rigid coupling and disconnected conditions

4.3.3. *The effect of room geometry*

To accommodate types of machineries, the compartments in offshore platforms often designed to various sizes and geometries. Room geometry and boundary condition determine the acoustic modes of the enclosure [9]. The following parametric study investigates the room modal properties with respect to the change of length/width ratio while the height is fixed. Consider a fixed width and height as $L_Y = 0.4$ and $L_Z = 0.3$, and assign variable length of the room as $L_X = 0.4, 0.6, 0.8, 1\,\mathrm{m}$ respectively, corresponding to length/width ratio of 1, 1.5, 2, and 2.5. Large length/width ratio leads to a more elongated room. Figure 4.6 presents the first 30 natural frequencies for each of the length/aspect ratio cases. It is observed that the natural frequencies of the structure-acoustic system are sensitive to the length/width ratio change. With the increasing on the room length, the natural frequencies decrease, meaning that the square structure-acoustic system have higher natural frequencies than that of elongated shapes. Figure 4.7 presents the pressure responses at the cavity center for each case. These plots illustrated a fact that the increasing of length/width ratio leads to an increasing on the numbers of resonance peak. It is also observed that, with the same excitation and boundary conditions applied, peak pressure amplitude of the four cases can be quite different. For example, within the frequency range, a difference of 16 dB is obtained between the cases with length/width ratio of 2 and 2.5. Using the present model, engineers can easily perform parametric studies related to geometry variation so that optimize the room shape and the source   locations.

73
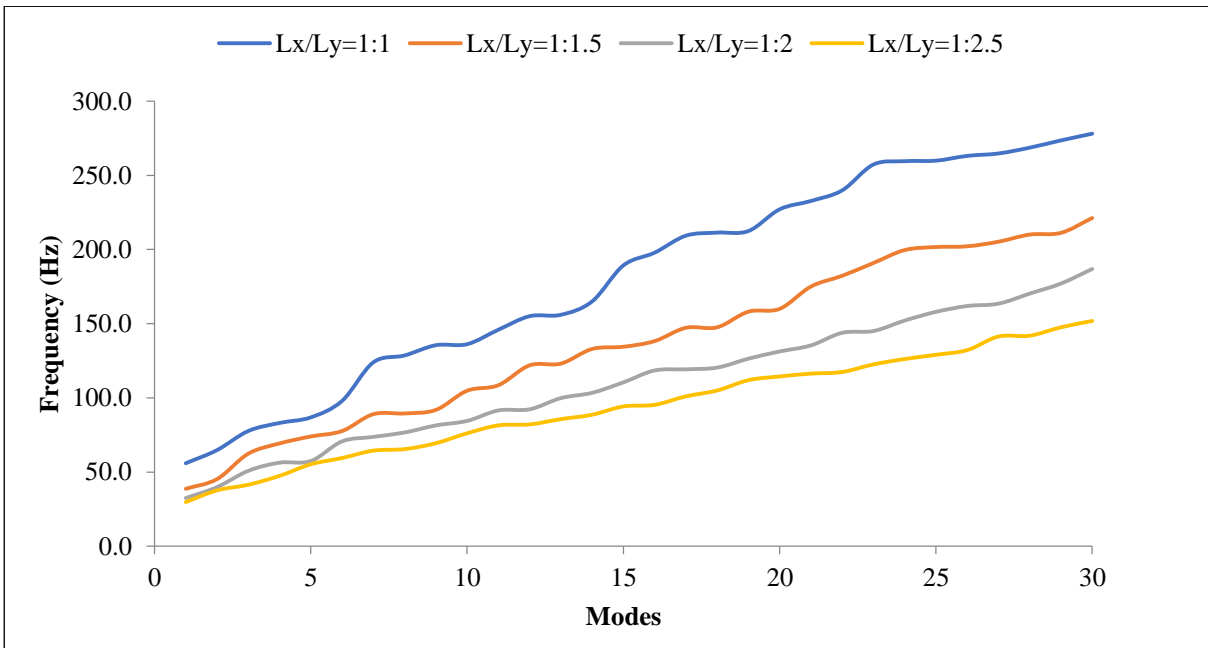
Figure 4.6 First 30 natural frequencies comparison
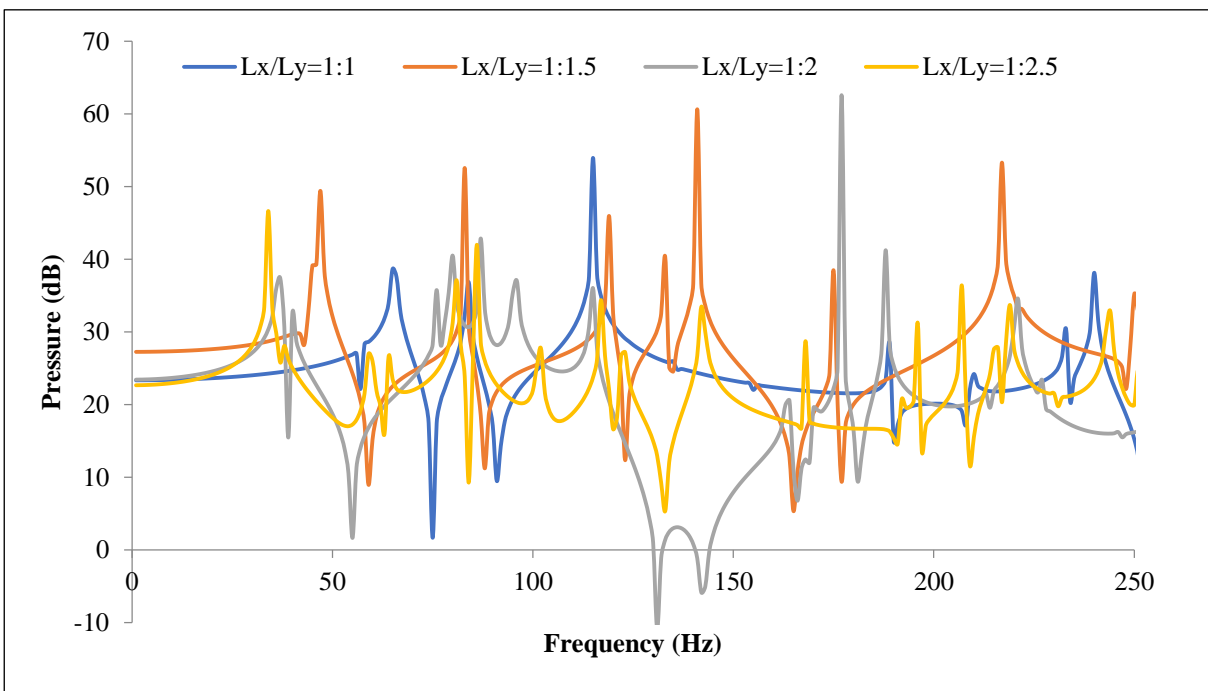
Figure 4.7 Effect of length/width ratio changing on the pressure response

4.3.4. *The effect of fluid loading*

The fluid loading condition can be quantified by a dimensionless parameter [19]

$$\lambda = \frac{\rho_{medium}c_{medium}}{\rho_s h_s \omega} \qquad\qquad \text{[4-55]}$$

The weak coupling exists when $\lambda < 1$ and $\lambda > 1$ for high coupling. As the air medium create a small loading and the coupling between the cavity and structures are weak. While the medium changes to a dense fluid such as water, it leads to a strong coupling of $\lambda > 1$. The previous examples have considered as a weak coupling between the air medium and boundary structures. The validity of the present method applied to high coupling condition will be performed in the following case.

In this case, replace the air medium in the section 3.2.1 by fresh water with density $\rho_{water} = 1000\,\text{kg/m}^3$ and speed of sound $c_{water} = 1480$ m/s. The responses of structure domain and acoustic domain under two mediums are compared. Due to the geometry symmetry, the center point of Plate #1, Plate #2, and Plate #6 are selected for as the receiver point. Figure 4.8 and figure 4.9 illustrate the impact of water medium on the system's dynamic behavior by comparing the variance of natural frequencies and velocity responses within the considered frequency range. It can be seen that the system's natural frequencies are obviously reduced from the air medium to water medium. Also, the the medium change significantly influences the dynamic responses of the system. As shown in figure 4.9, the plots showing the transverse and in-plane velocities at all selected locations are very different with two type of medium. It is also observed that there are same resonant peaks in the velocity response curve and pressure response curve with water medium; however, addition resonant peak are formed in the pressure response curve with air medium. This phenomenon might be attributed to the strong couling between structure and water cavity while weak coupling between structure and air cavity.

With this case study, it shows that present model can capture the interaction effects between the vibrating structures and contiguous fluids on the magnitudes and frequencies of the structural-acoustic interaction system.
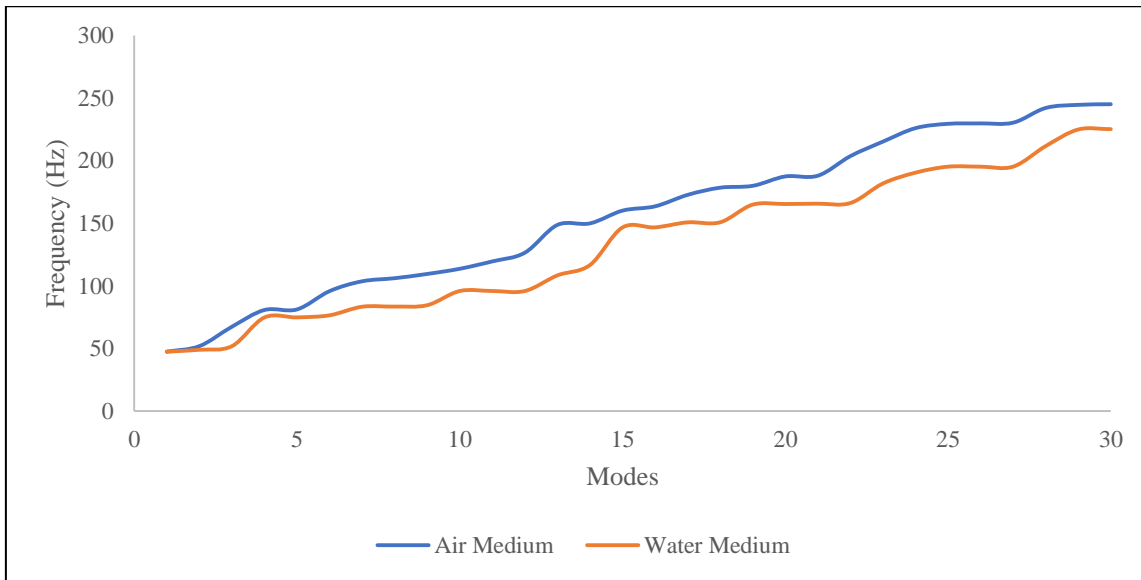
Figure 4.8 Comparison of first 30 natural frequency between air and water medium
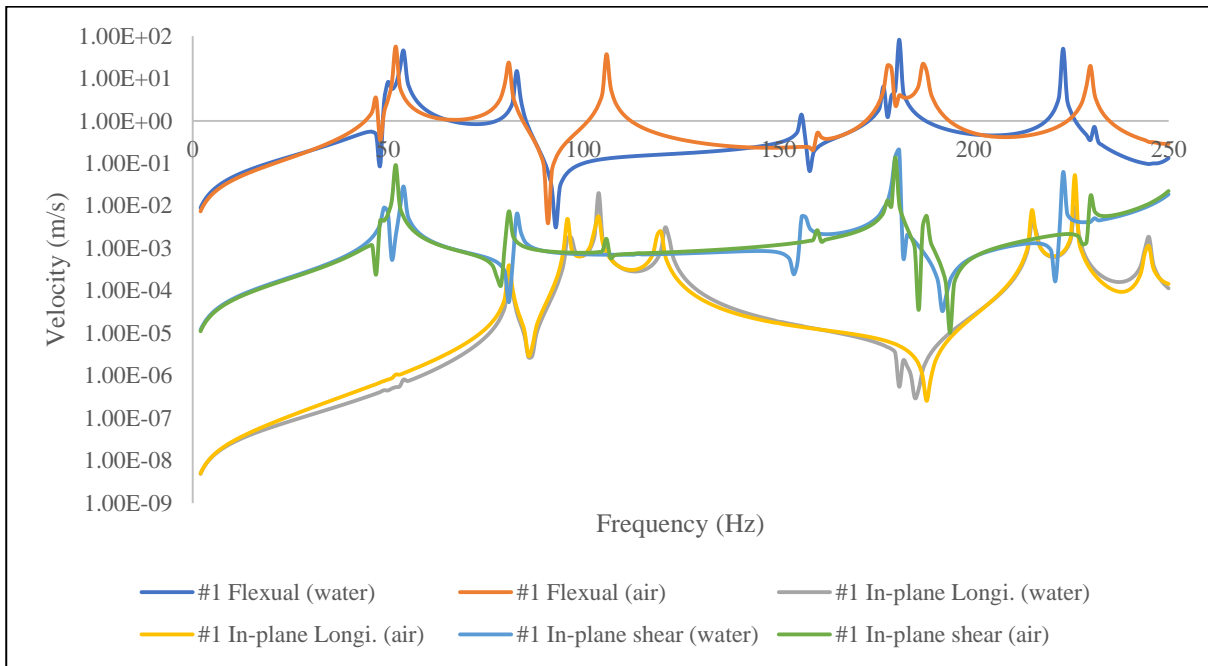
(a) Displacement response at plate #1 center
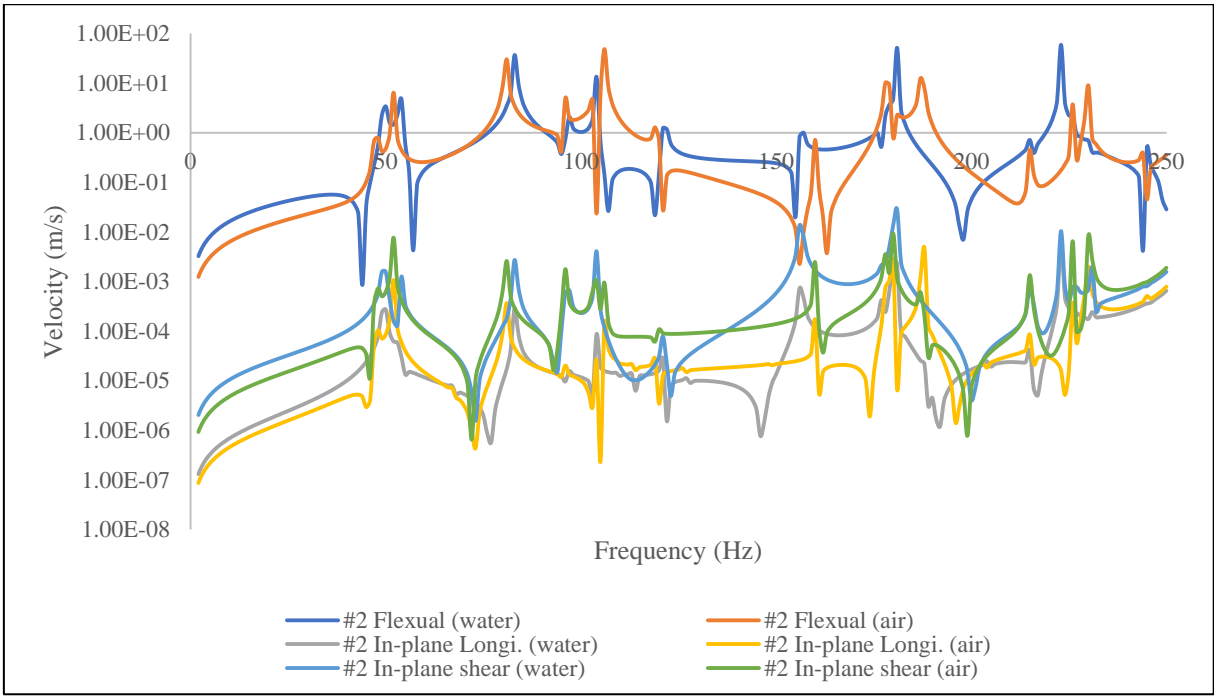
(b) Displacement response at plate #2 center
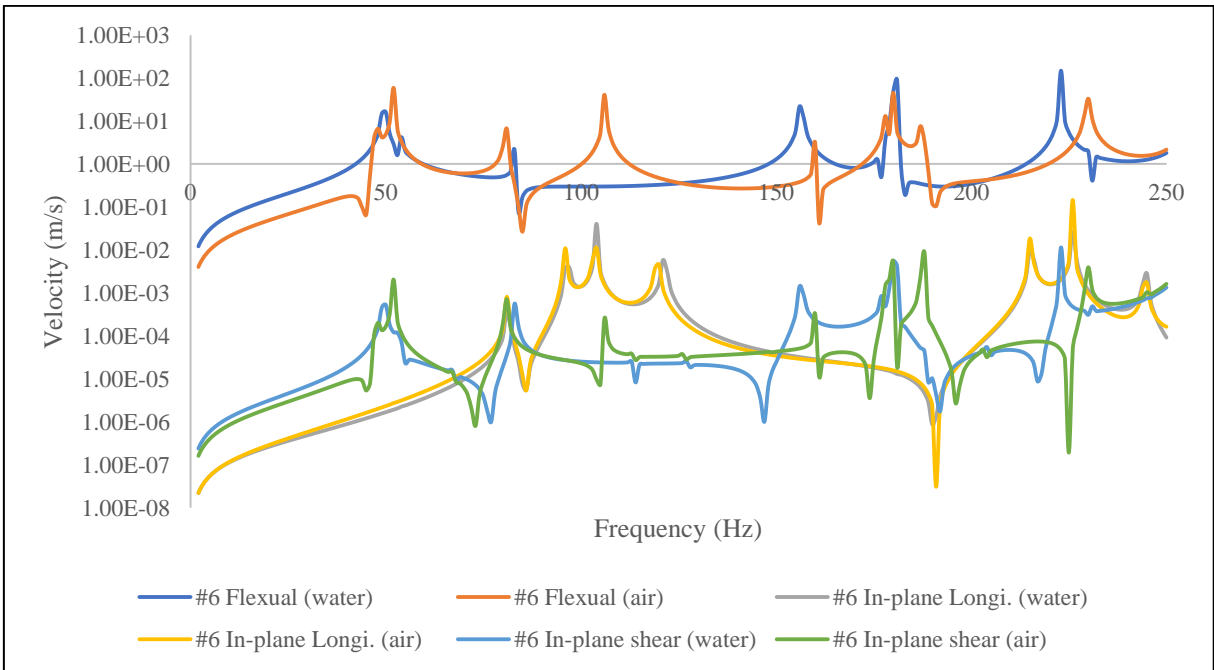
(c) Displacement response at plate #6 center
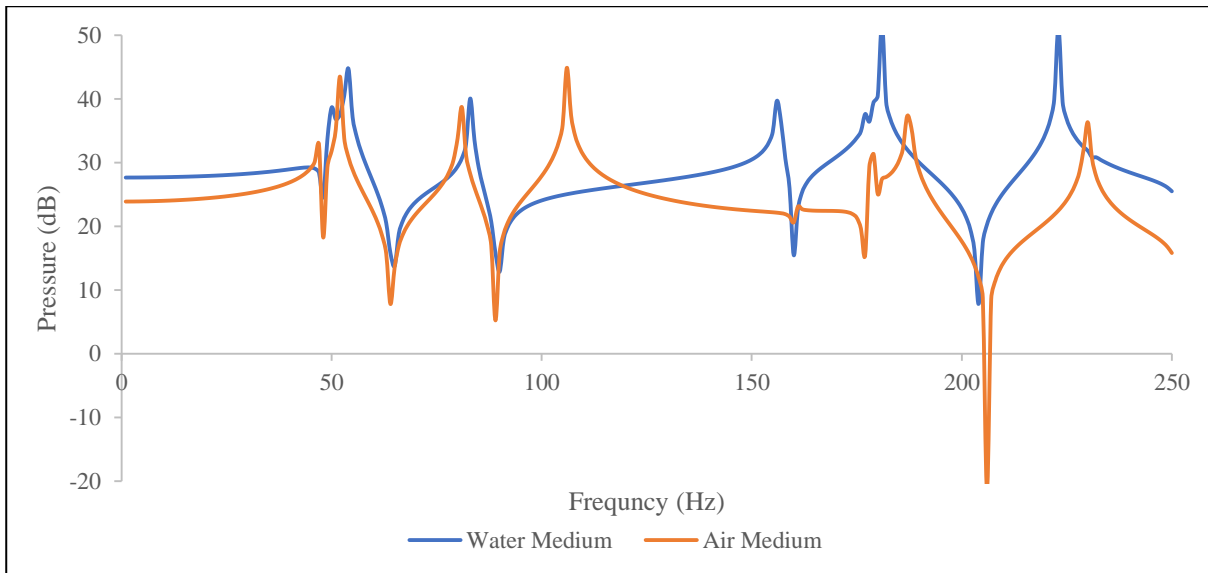
(d) Pressure response at the cavity center

Figure 4.9 Response comparisons for air medium and water medium

4.4. Conclusion

This chapter propose an analytical model for solving dynamic quantities for the three-dimensional fully coupled structural-acoustic system using Rayleigh-Ritz method. The structure-structure coupling effects are included by considering the energy loss due to the boundary force and moments. The influence of structure-acoustic interaction on the cavity and structure are considered through the work done by the interface. The proposed analytical model has been verified by FEM results. Therefore, it enables the structure-acoustic parametric studies to be handled by engineers more quickly without modifying the FE model. In contrast to the Fourier series based and improved Fourier series based admissible functions, Chebyshev polynomials of the first kind reduce the problem matrices dimension and ensure the derivative of the function exist and are continuous at any point of the considered region. As illustrated in section 3.2, the present model can handle parametric studies such as variation of structural boundary and coupling conditions, effect of medium and room geometry studies. It can be used as a simplified evaluation method for offshore platform environment at the design stage.

Due to the rapid convergence, numerical stability, high accuracy solutions can be obtained using Chebyshev polynomial, the present model can be extended to solve structures enclosing an arbitrary number of cavities, by decomposing the structural energy into subsets corresponding to the exterior surfaces and interior surfaces. Chapter 5 illustrates this procedure by solving the vibro-acoustics for a conjugate room case.

78

Chapter 5. Analytical Modelling of Vibro-acoustics Interaction for Conjugate Rooms and Coupled Room

5.1. Introduction

In the previous chapter, the proposed analytical method solved the vibro-acosutics of three-dimensional fully coupled structural-acoustic system under general boundary and coupling condition. This chapter extends the previous model to solve the vibro-acoustics for more complicated configuration; the conjugate rooms. There are large number of conjugate rooms in the offshore platform and it is a common configuration. This chapter aims to extend the method from last chapter, and model the dynamic quantities of the conjugate rooms analytically, i.e. the displacement response of the elastic structure, acoustic pressure in the acoustic field, and the transmission loss of the interior plate. By considering of the structural interaction force and the moment at edges, and structural-acoustic interaction on the interface, the structural and acoustic domains are fully coupled.

Chebyshev-Lagrangian method continuing used to formulate the structural and interior acoustical domains. The displacement components of the structure members and the sound pressure inside the acoustic domain are approximated regarding the two-dimensional and three-dimensional Chebyshev orthogonal polynomials, respectively. Reliability of current method is validated by checking natural frequencies of present methodology against those derived from finite element software. Then, using this model, parametric studies are conducted.

The following published paper is used for the contents of this section

[105] X. Ji and C. S. Chin, "Analytical Modeling of Vibroacoustics Interaction for Conjugate Enclosures," in Inter.noise 2017, Hong Kong, 2017.

5.2. Analytical Modelling of Vibro-acoustics Interaction for Conjugate Enclosures
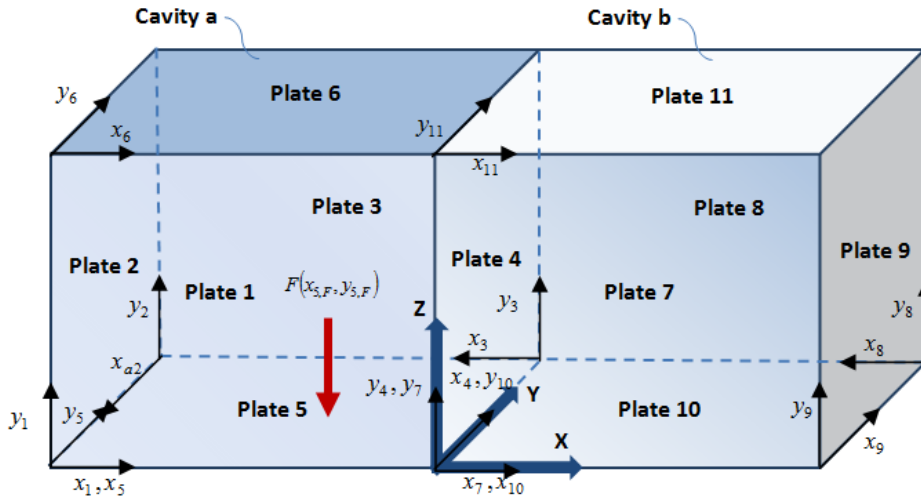
Figure 5.1 Schematic diagram of two conjugate enclosures **[106]**

The system under investigation comprises of two conjugate enclosures which separated by common plate, as shown in figure 5.1. These two spaces enclosed with eleven homogeneous and isotropic flat surface are denoted as a an b. Room boundaries are numbered, and plate dimensions are denoted as $L_{i,x}, L_{i,y}$ respectively in the Cartesian coordinates. The built-up system with a superposed reference between the global coordinate and the local coordinate of the common plate is investigated aiming to illustrate dynamics of acoustic cavity and structures.

Two conjugated enclosures result $N_{s,in} = 1$ number of interior common plate and $N_{s,ex} = 10$ number of exterior plates. The common interior plates separating two enclosures will subject the pressure loading from both enclosures simultaneously, while the exterior plates will be loaded by acoustic pressure from a single enclosure.

A total of 28 interconnected edges existed in this system. Follow the same spring technique used in the Chapter 4, four types of boundary springs are uniformly distributed to restrain the edges elastically for efficiently model the classical boundary conditions, and four types of coupling springs on the coupling edges to define the different coupling manner between plates. Still, K_w, k_w, k_p, and k_n for the rotational spring stiffness, translational spring stiffness, the in-plane linear spring stiffness to the edge, and in the normal direction to the edge, respectively; K_c, k_{cw}, k_{cu}, and k_{cv} for the coupling stiffness of the artificially connected two adjacent plates. Arbitrary set of classical boundary and coupling conditions at the edges of plates can be obtained by an appropriate choice of the stiffness values.

The unknown quantities such as the acoustic pressures in the rooms and the plate displacements can be calculated by expressing energy balance equation for the whole coupled system. This balance equation is obtained by superposing three basic phenomena: (i) the response of a plate excited by pressures acting on its surface; (ii) the response of an acoustic volume excited by the vibrations of a plate on its boundary; (iii) the response of an acoustic volume excited by sources. The continuity condition of structure-acoustic coupling system on the structural-acoustic interface is that the structural transverse velocities have to match with the air particle velocity as stated in equation [2-7].

A Chebyshev orthogonal functional basis defined on the relevant domain can be used to provide expressions for the field functions. The displacements of the ith plate with general elastic boundary restrains could be expanded in the form of double Chebyshev orthogonal polynomials as follows

$$w_i(\alpha_i, \beta_i) = \sum_{m_i=0}^{M} \sum_{n_i=0}^{N} A_{i,m_i,n_i} T_{m_i}(\alpha_i) T_{n_i}(\beta_i)$$

[5-1]

$$u_i(\alpha_i, \beta_i) = \sum_{m_i=0}^{M} \sum_{n_i=0}^{N} B_{i,m_i,n_i} T_{m_i}(\alpha_i) T_{n_i}(\beta_i)$$

[5-2]

$$v_i(\alpha_i, \beta_i) = \sum_{m_i=0}^{M} \sum_{n_i=0}^{N} C_{i,m_i,n_i} T_{m_i}(\alpha_i) T_{n_i}(\beta_i)$$

[5-3]

where A_{i,m_i,n_i}, B_{i,m_i,n_i}, and C_{i,m_i,n_i} are the unknown coefficients of the Chebyshev expansions yet to be determined. Moreover, $T_{m_i}(\alpha_i)$ and $T_{n_i}(\beta_i)$ are the one- dimensional first kind Chebyshev polynomial, M, N are the total employed terms, and the preferred choice of the polynomial numbers changes with the problems complexity, the geometry of examined system, the frequency range of interest.

Similarly, Chebyshev polynomials are adopted as global basis to approximate the sound pressure variable inside cavity as thus avoid meshing the sound field. The sound pressure in two cavities can be written as

$$p_a(\alpha_a, \beta_a, \varepsilon_a) = \sum_{mx=0}^{M_X} \sum_{my=0}^{M_Y} \sum_{mz=0}^{M_Z} E_{a,mx,my,mz} T_{mx}(\alpha_a) T_{my}(\beta_a) T_{mz}(\varepsilon_a)$$

[5-4]

$$p_b(\alpha_b, \beta_b, \varepsilon_b) = \sum_{mx=0}^{M_X} \sum_{my=0}^{M_Y} \sum_{mz=0}^{M_Z} E_{b,mx,my,mz} T_{mx}(\alpha_b) T_{my}(\beta_b) T_{mz}(\varepsilon_b)$$

[5-5]

in which $T_{\Xi_i}(\chi)$ ($\Xi_i = mx, my, mz, \chi = \alpha_a, \beta_a, \varepsilon_a, \alpha_b, \beta_b, \varepsilon_b$) denotes the one- dimensional first

kind Chebyshev polynomial in respect of sound pressure. Ξ_i are the total employed terms. $E_{a,mx,my,mz}$ and $E_{b,mx,my,mz}$ are the unknown coefficients of the Chebyshev expansions for two cavities.

The dynamic behavior of the fully coupled system are determined by the energy principle using Rayleigh-Ritz method. The linear structural model of the structural-acoustic system is firstly established by decomposing the structural energy into subsets corresponding to the exterior surfaces and interior surfaces which yield the general form of functions as

$$L^S = \sum_{i=1}^{11}\left(V_i^S - T_i^S\right) + \sum_{ij}^{28}V_{ij}^C + \sum_{i_{ex}=1}^{10}W_{i_{ex}}^{AS} + W_{i_{in}}^{AS} - W_i^F \qquad \text{[5-6]}$$

where $V_i^S = V_i^T + V_i^{In}$ is the potential energy done due to transverse and in-plane deformation, $T_i^S = T_i^T + T_i^{In}$ is the total kinetic energy of i th plate. W_i^F is the work done by external loads, V_{ij}^C Represents the potential energy due to the structural coupling between plate i and its adjacent plate j . The detail expression of these energy terms can be referred to equation [4-2] to [4-5] and equation [4-7] to [4-8]. $W_{i_{ex}}^{AS}$ is the work done by acoustic loading to the exterior surfaces; $W_{i_{in}}^{AS}$ denotes the additional work done by the resultant acoustic pressure loading from the cavity a and b simultaneously.

$$W_{i_{in}}^{AS} = \frac{1}{2}\int_0^{L_{in,x}}\int_0^{L_{in,y}}w_{i_{in}}\left(p_{i,a} - p_{i,b}\right)dx_{i_{in}}dy_{i_{in}} \qquad \text{[5-7]}$$

$$W_{i_{ex}}^{AS} = \frac{1}{2}\int_0^{L_{ex,x}}\int_0^{L_{ex,y}}w_{i_{ex}}p_i dx_{i_{ex}}dy_{i_{ex}} \qquad \text{[5-8]}$$

Similarly, the energy function for the acoustic domain, L^A is constructed by the sum of potential energy and kinetic energy of individual cavities V_a^A, V_b^A and T_a^A, T_b^A respectively,

$$L^A = V_a^A - T_a^A + V_b^A - T_b^A + \sum_{i_{ex}=1}^{10}W_{i_{ex}}^{AS} + W_{i_{in}}^{AS} \qquad \text{[5-9]}$$

The detail energy expression of the potential energy V_I^A and kinetic energy T_I^A of cavity I can be found in the Chapter 4 equation [4-10] to [4-11].

The definition domain for the Chebyshev polynomials is restricted to the interval [-1, 1], therefore, before substituting displacement expansions and pressure expansions into the Lagrangian equation, mapping the real coordinate in the physical to the range [-1, 1] is needed. The coordinates transformation take place according to equation [4-16] and [4-17].

After making corresponding transformations in the energy expressions, and substituting into the function expression in equation [5-5] and [5-9] with admissible functions [5-1] to [5-5] respectively, the resulting algebraic equation for the vibro-acoustics interaction of two conjugate enclosure can be established by performing the partial differential on unknown coefficients A_{i,m_i,n_i}, B_{i,m_i,n_i}, C_{i,m_i,n_i} and $E_{I,mx,my,mz}$

$$\begin{bmatrix} \mathbf{K}_S & \mathbf{C}_{SA}{}^T \\ \mathbf{0} & \mathbf{K}_A \end{bmatrix} \begin{bmatrix} \mathbf{\Theta} \\ \mathbf{\Omega} \end{bmatrix} - \omega^2 \begin{bmatrix} \mathbf{M}_S & 0 \\ -\mathbf{C}_{SA} & \mathbf{M}_A \end{bmatrix} \begin{bmatrix} \mathbf{\Theta} \\ \mathbf{\Omega} \end{bmatrix} = \begin{Bmatrix} \mathbf{F} \\ \mathbf{0} \end{Bmatrix} \qquad [5\text{-}10]$$

where subscripts S and A denote that the variables are related to the structure and cavity respectively. $\mathbf{M}$ and $\mathbf{K}$ are the generalised global mass and stiffness matrices. The stiffness matrices of the structure domain $\mathbf{K}_S$ is formed by the transverse component $\mathbf{K}_i^T$, four in-plane components $\mathbf{K}_i^U$, $\mathbf{K}_i^V$, $\mathbf{K}_i^{UV}$, $\mathbf{K}_i^{VU}$, and structural coupling components $\mathbf{K}_{ij}^C$ as

$$\mathbf{K}_S = \begin{bmatrix} \mathbf{K}_1^T & \mathbf{0} & \mathbf{0} & \mathbf{0} & \mathbf{0} & \mathbf{0} & \mathbf{0} \\ \mathbf{0} & \mathbf{K}_1^U & \mathbf{K}_1^{UV} & \mathbf{0} & \mathbf{0} & \mathbf{0} & \mathbf{0} \\ & \mathbf{K}_1^{VU} & \mathbf{K}_1^V & \mathbf{0} & \mathbf{0} & \mathbf{0} & \mathbf{0} \\ & & & \mathbf{O} & \mathbf{0} & \mathbf{0} & \mathbf{0} \\ & & & & \mathbf{K}_{3N_p}^T & \mathbf{0} & \mathbf{0} \\ & & & & & \mathbf{K}_{3N_p}^U & \mathbf{K}_{3N_p}^{UV} \\ \textbf{symmetric} & & & & & \mathbf{K}_{3N_p}^{VU} & \mathbf{K}_{3N_p}^V \end{bmatrix} + \begin{bmatrix} \mathbf{K}_{1-1}^C & \mathbf{K}_{1-2}^C & \Lambda & \mathbf{K}_{1-3N_p}^C \\ \mathbf{K}_{2-1}^C & \mathbf{K}_{2-2}^C & \Lambda & \mathbf{K}_{2-3N_p}^C \\ \mathbf{M} & \mathbf{M} & \mathbf{O} & \mathbf{M} \\ \mathbf{K}_{3N_p-1}^C & \mathbf{K}_{3N_p-2}^C & \Lambda & \mathbf{K}_{3N_p-3N_p}^C \end{bmatrix} \qquad [5\text{-}11]$$

where N_P is number of plates in the structural domain.

The stiffness vector of acoustic domain $\mathbf{K}_A$ is expressed as

$$\mathbf{K}_A = \begin{bmatrix} \mathbf{K}_a & \mathbf{0} \\ \mathbf{0} & \mathbf{K}_b \end{bmatrix} \qquad [5\text{-}12]$$

The structure mass matrix $\mathbf{M}_S$ and acoustic mass matrix are expressed as

$$\mathbf{M}_S = \mathrm{diag}\{\mathbf{M}_1 \quad \mathbf{M}_1 \quad \mathbf{M}_1 \quad \Lambda \quad \mathbf{M}_{N_P} \quad \mathbf{M}_{N_P} \quad \mathbf{M}_{N_P}\} \qquad [5\text{-}13]$$

$$\mathbf{M}_A = \begin{bmatrix} \mathbf{M}_a & \mathbf{0} \\ \mathbf{0} & \mathbf{M}_b \end{bmatrix} \qquad [5\text{-}14]$$

The structure-acoustic coupling term $\mathbf{C}_{SA}$ is expressed as

$$\mathbf{C}_{SA} = \begin{bmatrix} \mathbf{C}_{1a}^T & 0 & 0 & \Lambda & \mathbf{C}_{4a}^T & 0 & 0 & \Lambda & \mathbf{C}_{6a}^T & 0 & 0 & 0 & 0 & 0 & \Lambda & 0 & 0 & 0 \\ 0 & 0 & 0 & \Lambda & \mathbf{C}_{4b}^T & 0 & 0 & \Lambda & 0 & 0 & 0 & \mathbf{C}_{7b}^T & 0 & 0 & \Lambda & \mathbf{C}_{11b}^T & 0 & 0 \end{bmatrix}^T$$

$$[5\text{-}15]$$

The $\mathbf{\Omega}$ and $\mathbf{\Theta}$ in the equation [5-10] are the generalised pressure vector and displacement vector, given as: $\mathbf{\Theta} = [\mathbf{a_1}, \mathbf{b_1}, \mathbf{c_1}, \mathbf{a_2}, \mathbf{b_2}, \mathbf{c_2}, K\ \mathbf{a_{11}}, \mathbf{b_{11}}, \mathbf{c_{11}}]^T$, $\mathbf{\Omega} = [\mathbf{e^a}, \mathbf{e^b}]^T$. The particular expression of coefficient matrix for $\mathbf{a_i}, \mathbf{b_i}, \mathbf{c_i}$ and $\mathbf{e^I}$ are given below

$$\mathbf{a_i} = \{A_{i,0,0}, A_{i,0,1}, K\ A_{i,m,0}, A_{i,m,1}, K\ A_{i,m,n}, K, A_{i,M,N}\}^T \tag{5-16}$$

$$\mathbf{b_i} = \{B_{i,0,0}, B_{i,0,1}, K\ B_{i,m,0}, B_{i,m,1}, K\ B_{i,m,n}, K, B_{i,M,N}\}^T \tag{5-17}$$

$$\mathbf{c_i} = \{C_{i,0,0}, C_{i,0,1}, K\ C_{i,m,0}, C_{i,m,1}, K\ C_{i,m,n}, K, C_{i,M,N}\}^T \tag{5-18}$$

$$\mathbf{e^I} = [E^I_{0,0,0}, E^I_{0,0,1}, K, E^I_{0,0,MZ}, E^I_{0,1,0}, K, E^I_{0,1,MZ}, K, E^I_{0,MY,MZ}, K, E^I_{MX,MY,MZ}]^T \tag{5-19}$$

The free vibration problem for the structure-acoustic coupled system can be easily solved by assuming harmonic motion and removing the external load $\mathbf{F}$ from equation [5-10]. The response of sound pressure and external load can be obtained by solving equation [5-10] and back-substituting corresponding coefficients into the expression of the sound pressure and plate displacements.

5.2.1. *Model Verification*

To validate the reliability of the present method for modeling the vibro-acoustics for conjugate enclosures, the modal results are checking against results obtained from FEA. Consider two identical cavities a and b with a dimension of $L_X \times L_Y \times L_Z = \ =0.25\text{m} \times 0.4\text{m} \times 0.3\text{m}$ are coupled through plate #4 on the yz-plane. The material properties of all plates are specified as thickness = 2.5 mm, Poisson's ratio $\upsilon = 0.3$, young's modulus $E = 71 \times 10^9$ Pa, and mass density $\rho_s = 2700\text{kg/m}^3$. The density of and sound speed in the air cavity are $\rho_a = 1.21\text{kg/m}^3$ and $c_0 = 340\text{m/s}$. A dynamic mechanical force of 100N is acting normal to the floor (Plate #5) center ($x_{5,F} = 0.125m$, $y_{5,y} = 0.2m$)

In the current case, the edge $x_5 = 0m$ and $x_{10} = 0.5m$ are assumed to be a constraint in all translation and rotation directions, and all structure members are rigidly connected. The rigid boundary condition and connection manner is realised by setting the stiffness of the corresponding rotational springs, translation springs, coupling springs to infinity which is represented by an enormous number, 10^{12} in the numerical calculations. To validate the accuracy of the present model for mechanical excitation a numerical example is carried out and comparison is made with those obtained from the finite element program Hyperwork using element size of 10 mm shell element and solid element for both the plate and acoustic components, respectively. Figure 5.2 compared the first 30 natural frequencies of the conjugate enclosure system calculated by the

present method and FEM software. A good agreement is observed with the largest difference at 5.3%. In this example, the Chebyshev polynomials are truncated to $M = N = 10$ for structures displacements, and $M_X = M_Y = M_Z = 10$ for the cavity pressures.
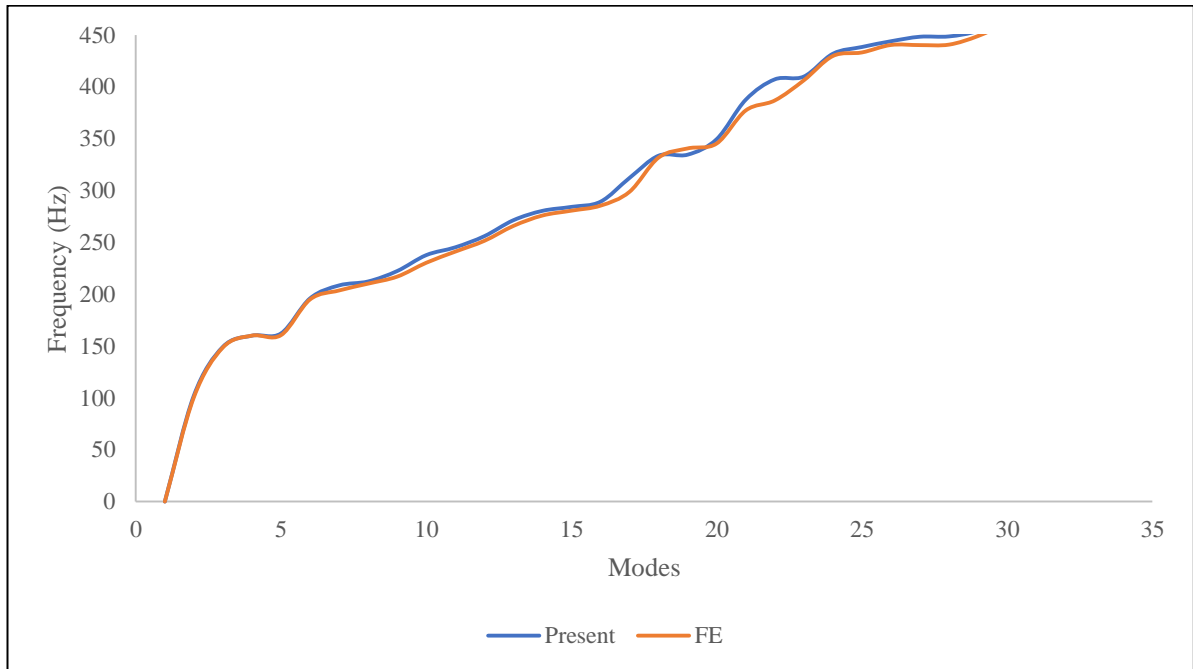
Figure 5.2 Verification of the first 30 natural frequencies calculated by present method and FEA software

5.2.2. *Effect of structural coupling*

Section 3.2.2 discussed the impact of structural coupling manner on the dynamic characteristics of single room system, and compared the dynamic responses for rigidly connected structural domain and disconnected structural which normally proposed in the convention structural cavity interaction studies [83] [12] [85]. Also, different coupling manners of the structural domain induce significant impact on the vibro-acoustic of conjugate rooms. With the analytical model, two scenarios are proposed to illustrate the impacts. Scenario one considers all plates are disconnected and independent while scenario two considers all plates are rigidly connected and participate in the energy transmission in both structural and acoustic domains.

In the framework of present model, scenario one is achieved by setting all coupling spring stiffness to zero, while for the scenario two, very large values of coupling springs are defined to represent rigid connections. The impact of structural coupling manner can be evaluated based on the difference of system natural frequencies and dynamic responses between two scenarios. First, figure 5.3 present the significant difference on the natural frequency between two scenarios. We observed that, the rigid connection from plate to plate increased the system stiffness, thus largely increased the natural frequencies. As a result, the dynamic behaviour of a system formed by the disconnected and coupled structural domain can be very much different which will be illustrated by the following dynamic response comparison.
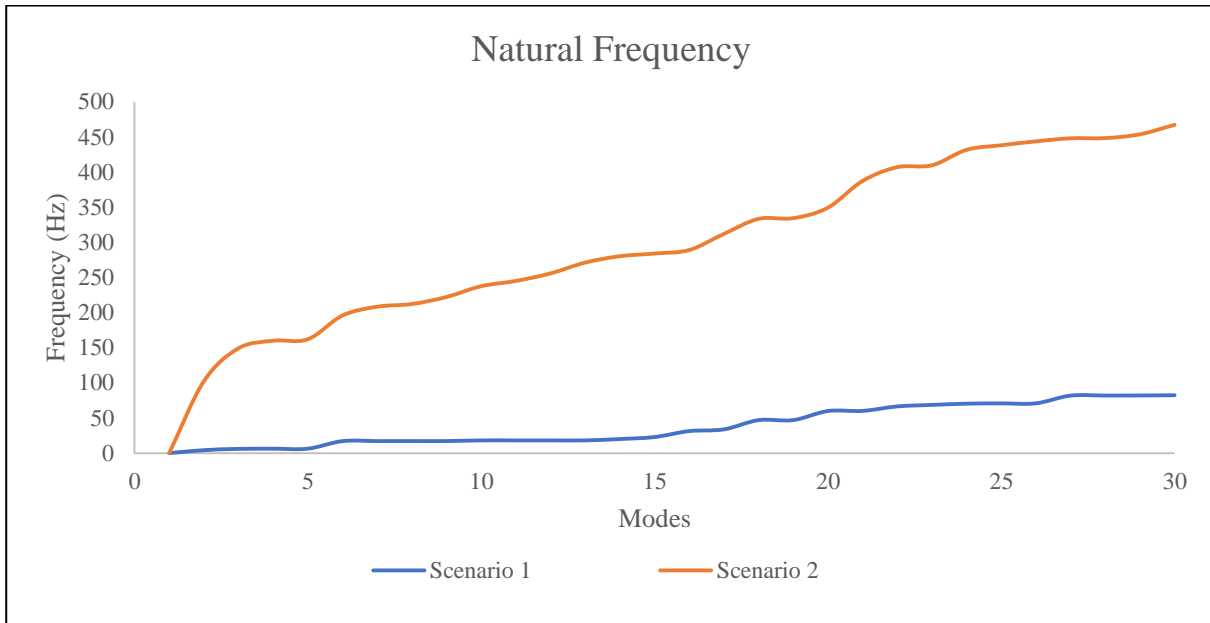
Figure 5.3 First 30 natural frequencies

Five receiver points are selected to compare the response with respect to the change of coupling manner. The local coordinates and belonging subsystems are indicated in the table 5.1. One point each for plate 2, plate 4, plate 11, cavity a, and cavity b.

Receiver	Coordinates			Domain
R1	$x_2 = 0.2$m	$y_2 = 0.15$m		Plate 2
R2	$x_4 = 0.2$m	$y_4 = 0.15$m		Plate 4
R3	$x_{11} = 0.125$m	$y_{11} = 0.2$m		Plate 11
R4			$Z = 0.15$m	Cavity a
	$X = -0.125$m	$Y = 0.2$m		
R5			$Z = 0.15$m	Cavity b
	$X = 0.125$m	$Y = 0.2$m		

Table 5.1 local coordinates of the selected receiver points

The responses are compared in terms transverse and in-plane vibration velocities at receiver R1, R2 and R3, and sound pressure level responses generated at R4 and R5. The comparisons are made for both scenarios up to 250 Hz and the results are present in the figure 5.4 and figure 5.5. It is observed that the vibration velocities at all selected receiver points on different components are following a similar trend: the disconnected structural domain (Scenario 1) resulted in relatively constant transverse velocities which fluctuated within a range. At lower frequencies, the transverse velocities of Scenario 1 are higher than that of Scenario 2. As the frequency increases, the transverse velocities of connected structural domain (Scenario 2) overtake that of disconnected structural domain (Scenario 1). As for the in-plane velocities, Scenario 2 are always much larger than that of Scenario 1. In fact, the in-plane velocities of Scenario 1 are approaching zero.

As illustrated in section 3.1, two factors that influence the transverse vibration are the vibration transmission and fluid-structure interaction. However, the fluid-structure interaction does not impact on the structure in-plane vibrations. Therefore, even though there is no coupling between structures, plates of Scenario 1 still generate vibration in the transverse direction, but obtain very minor in-plane vibrations. In addition, the velocity response plots of Scenario 2 are smoother within the considered frequency range as comparing to the Scenario 1, peak amplitudes are largely reduced.
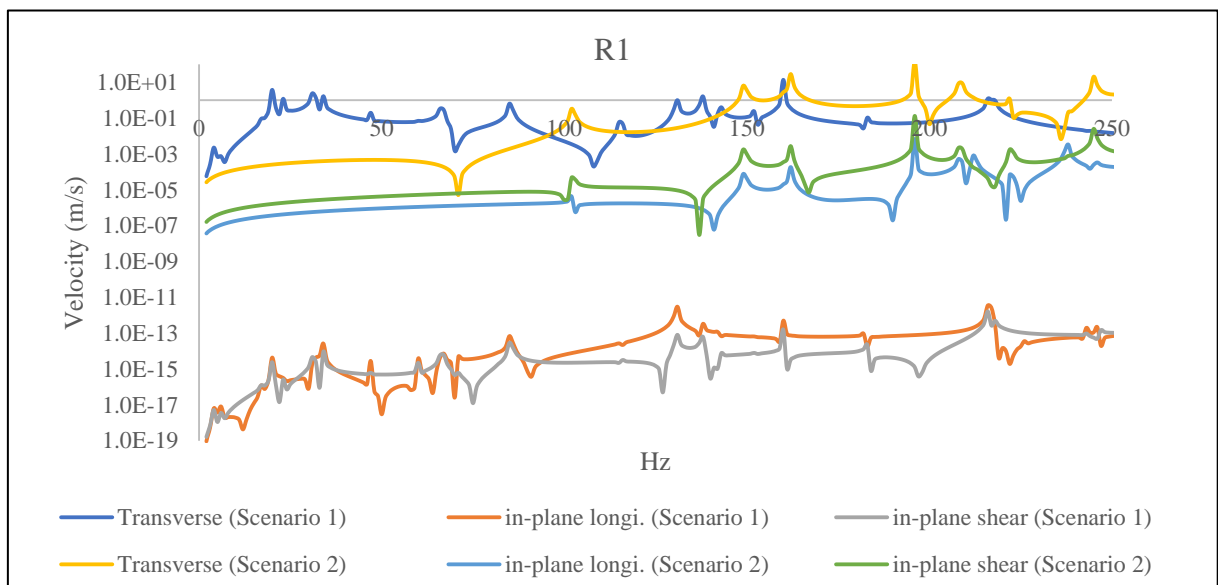
(a) Velocity responses at R1
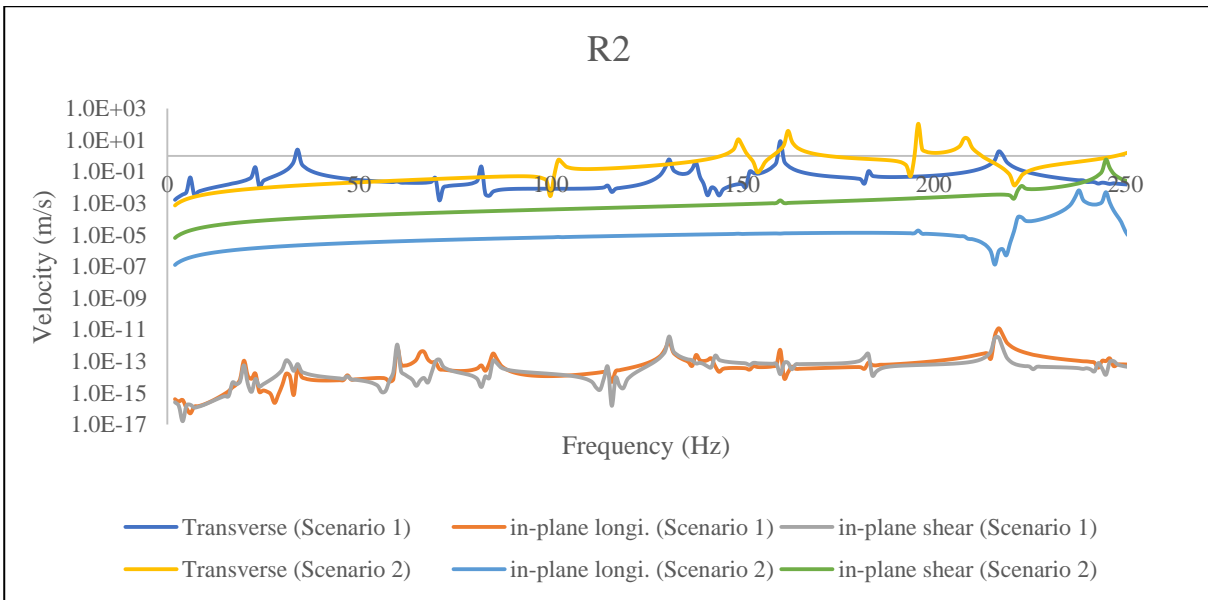
(b) Velocity responses at R2
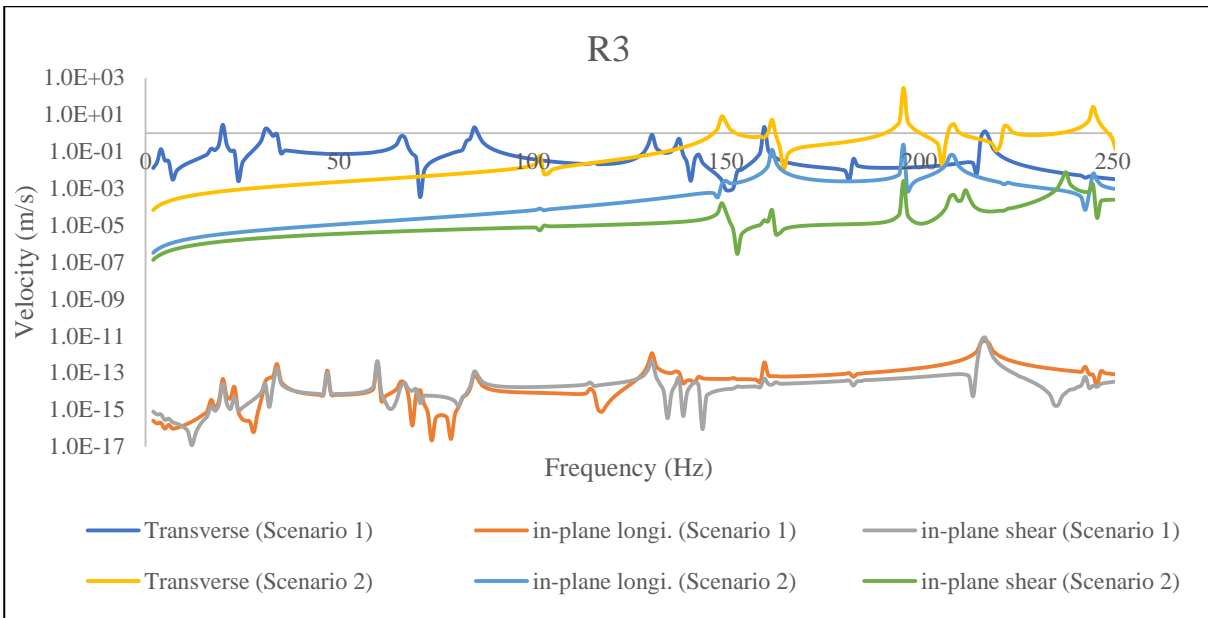
(c) Velocity responses at R3

Figure 5.4 Velocity response comparison between Scenario

Looking at the pressure difference at R4 and R5, $|p_{R4} - p_{R5}|$ resulted from both scenarios shown in figure 5.5, the disconnected structural domain resulted in a maximum of 27 dB pressure difference between two cavities within the considered frequency range. This value is higher than the difference value 16 dB resulted from the scenario two. These comparisons explain how important of taking consideration of structural couplings when analysing the vibro-acosutics of conjugate enclosures in the offshore platform environment. Large calculation error may lead to wrong acoustic design and fail to comply with criteria.
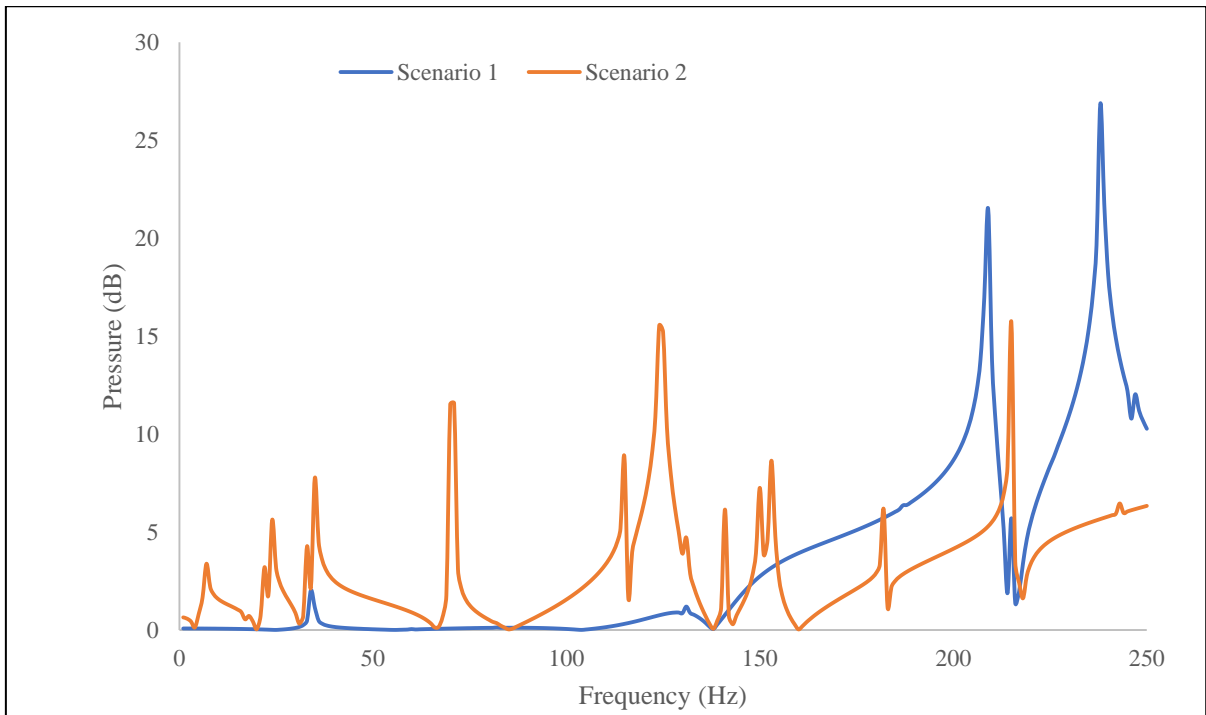
Figure 5.5 Pressure difference between R4 and R5 between scenario 1 and scenario 2

5.2.3. *Determine transmission loss of the interior plate*

Material properties of the common interior plate can largely influence the sound transmission from the source room to the receiver room. This phenomenon is investigating with the proposed conjugated room model.

For two conjugate rooms with the same dimension, filled medium, properties of exterior plates and boundary conditions, the material properties of the interior plate can be the dominant factor that influencing the energy transmission between two cavities. Under this assumption, scenario one transformed to a pure transmission problem which characterised by the parameter Transmission Loss (TL). The attempts to model the low frequency sound transmission are sparse compared to the number of studies on the higher frequency sound transmission [107]. The following study investigate the influence of partition material on the sound transmission between two cavities by using the present model.
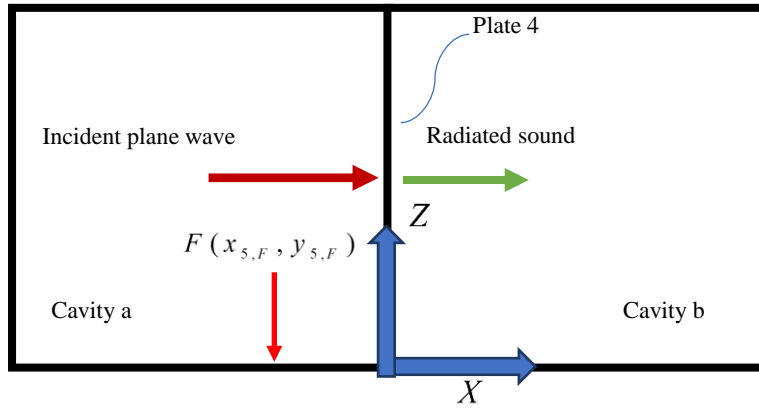
Figure 5.6 Schematic of sound transmission through an elastically restrained plate four between cavity a and b

Figure 5.6 sketches the profile view of the conjugate room shown in figure 5.2. The external force F injection on the plate 5 generate structure-borne noise in the cavity a. Under the condition of scenario one, acoustic pressures in the cavity a are generated by structural-acoustic interaction. The interior plate #4 receives the pressure incidence on the interface with the cavity a and results in transverse vibration at the resonant frequencies. Meanwhile, acoustic pressure response is generated in the cavity b through coupling with plate #4 at the interface.

The sound transmission loss of plate 4 (TL_4) is determined by the following measurement formula [108]

$$TL_4 = 10\log\left|\frac{p_{incident}}{p_{transmit}}\right|^2 \qquad \text{[5-20]}$$

In which $p_{incidence}$ and $p_{transmit}$ are the incidence pressure and transmitted pressure in the cavity a and cavity b respectively.

Table 5.2 present three types of material properties assigned to plate #4 for the transmission loss study up to 250 Hz. No damping or absorptive material are applied to both rooms. Using the present model, calculate the acoustic pressures of two mirror locations on the interface between cavity a and plate 4, and cavity b and plate 4. The corresponding TL determined separately for each material type and variable plate thicknesses are shown in figure 5.7 and figure 5.8 respectively. It is noted that in the considered frequency range, transmission loss of all cases obtained from present method and Mass Law expressed in the equation [5-21], show different performance. The curves calculated by present method exhibit peaks and dips whereas Mass Law curves are rather smooth.

90

$$R_0 = 20\log\left|\frac{\pi f \rho_S h}{\rho_0 c_0}\right|^2 \qquad [5\text{-}21]$$

In fact, sound transmission is dominated by the modal behaviour of rooms and structure at low frequencies. The results from present method show an irregular sound transmission function due to the modal behaviour of the plate #4. However, sound transmission occurs at high frequencies is determined by the mass of the separating wall and non-resonant transmission is dominant where the Mass Law is applicable [109].

Material	$\rho_{4,S}$ [kg/m³]	E [GPa]	h_4 [mm]	υ_4 [-]
Steel	7850	210	2.5	0.3
Aluminium	2700	71	2.5	0.3
Glass	2500	62	2.5	0.28

Table 5.2 Material data used in the parametric studies
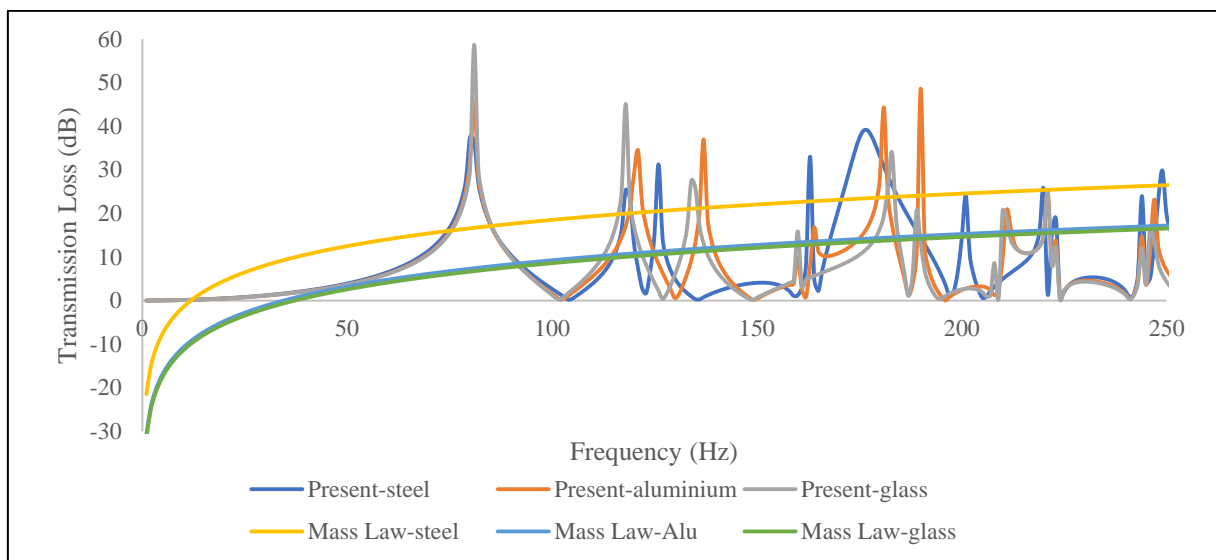
Figure 5.7 Calculated TL for plate 4 in different material properties

91
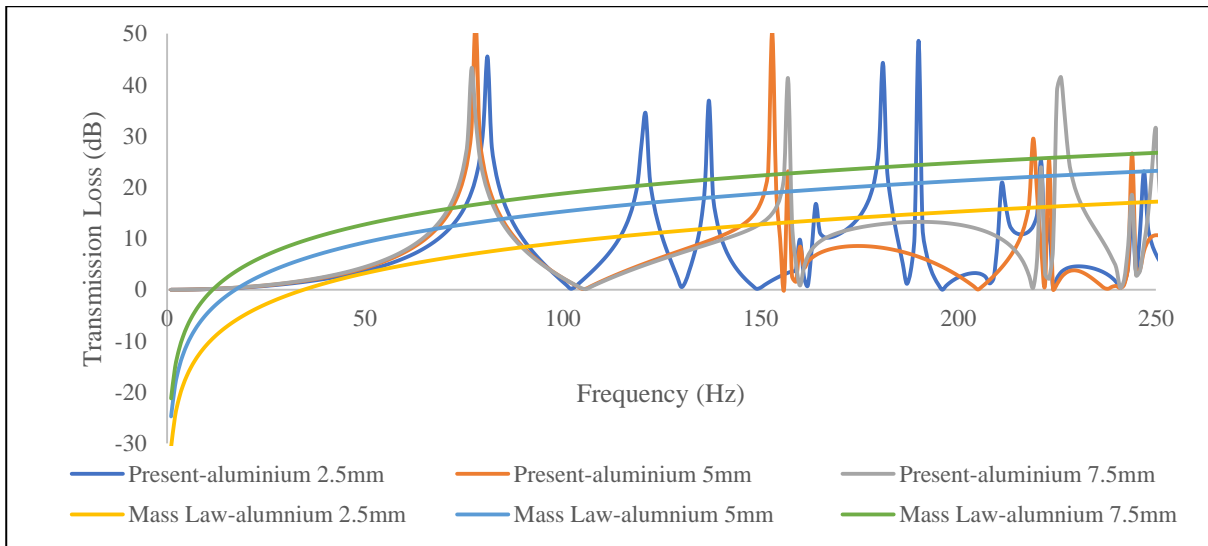
Figure 5.8 Calculated TL for plate 4 with different plate thickness

Comparing to the reference [19] which also models three-dimensional structural-acoustic interaction phenomenon, the proposed model offers some advantages. First, the structural modes and acoustic cavity modes need not to be determined in prior [103]. The proposed technique provides a systematic solution for complex configurations without identifying the modes through the FEA procedure. Secondly, the proposed approach overcomes the limitation for a medium such as air only. Since the continuity condition on the structural-acoustic interface is satisfied, the present approach is capable of handling a wider range of practical problems such as a room or tank conjugation. Thirdly, the mode information obtained from FEA [103] may face frequency limitation due to the high computation cost. However, the accuracy of high-frequency response used in the proposed approach can be improved by increasing the polynomial order. Also, the general boundary condition and coupling provide the flexibility to solve real problems.

5.3. Conclusion

An analytical model has been developed for investigating the vibro-acoustics behavior of conjugate enclosures under general boundary condition. The reliability of the present model is validated by comparison with commercial FEA software results with good agreement achieved. Different coupling manner within the structure domain give significant impact on the modal property and the dynamic response of the structural-acoustic system. Large calculation errors are observed in the case study when the coupling manner is set wrongly. Therefore, the present method avoids the potential error that may cause by the convention panel-cavity model when handling the vibro-acoustics problem of offshore platform conjugate enclosures.

Chapter 6.   Noise Modelling Using Modified Multiple Generalized Regression Neural Network Models with Fuzzy C-Means and Principal Component Analysis

6.1.   Introduction

Noise control is an important aspect which ensures the crew habitability onboard offshore platform. Implementing noise prediction is an effective way to identify the potential noise problem at the early stage of offshore platform design to avoid expensive retrofitting cost in the later stage of modification. Chapter 2 has reviewed the conventional methods applied in identifying the excessive noise in the offshore applications, including empirical formula or the computer-aided design (CAD)-based numerical tools. Chapter 4 and 5 explore the analytical way of modelling the structure-acoustic interaction of the single, conjugate and coupled room in offshore platform environment.

For example, the finite element analysis (FEA) solve acoustic responses numerically; the statistical energy analysis (SEA) determine the sound field based on power flow between subsystems. Using these CAD-based tool are proven to be quite accurate for certain frequency regime, however, applying for large scale system such as the offshore platform are often very time and resource consuming. The use of Chebyshev expansions solutions under Rayleigh-Ritz frame gives accurate results and rapid convergence for the three-dimensional problem analytically. But it still requires extensive formulation on the acoustics room of interest. Empirical formulas require similar noise problem or configuration where they were developed. The accuracy of the results could not be guaranteed [110] if the empirical or /and formulas are applied on different applications as some are unable to meet the required assumptions such as room's shape and sound source.

For the past few decades, neural networks have been used to model complex systems. In machine learning, there are many methods available in the literature. In this chapter, a general regression neural network (GRNN) [111] is adopted for the main reason that it is quite advantageous due to its ability to converge to the underlying function of the data after few training samples and the results are quite consistent. A full knowledge of the system or exact parameters to be modelled is often not required. This makes GRNN a useful tool to perform prediction and comparison of system performance in practice. As a result, the noise engineers can spend more time on the noise analysis instead of creating an accurate CAD model or analytical equations that requires exact values of the model variables in computer-based acoustic simulation.

Many applications including the noise-related applications [112-115] use GRNN. In the current literature, GRNN application on the offshore platform such as a jack-up rig has not been discussed. In addition, the inherent use of steels for room construction in the jack-up rig differs from most of the land-based industrial and acoustic rooms [116-117] that increase the percentage of structure-borne noise than airborne noise. Moreover, the problems of selecting the appropriate inputs from the design variables (e.g., actual position of the noise sources, room dimensions, and other acoustic variables) are often impeded by a lack of exact information during the early design stage of the offshore platform. The relevant inputs used for GRNN training are often quite subjective, and the types of input variables used for training can vary across different noise engineers due to their experience.

Hence, a modified multiple GRNN using fuzzy C-means (FCM) clustering and principal component analysis (PCA) is proposed to predict the noise level on the jack-up rig with the least number of significant inputs. The training and test samples from 125 to 8000 Hz obtained from the computer-based statistical energy analysis (SEA) with direct field (SEA-DF) software approach validated by experimental data [60] will be used. These input data will be preprocessed by FCM and PCA to group the dominant samples together and reduce the dimensionality of the input variables before commencing the training using GRNN. With optimal spread variables obtained for each cluster at different frequencies, multiple GRNN can be fused to form an optimal GRNN. The proposed method enables noise engineers to predict the noise level on any similar offshore platform without repeating the SEA modeling that is often time and resource consuming.

The works in this chapter was published in the following paper. Majority of the works was used to form the section 5.2 to section 5.8.

[118] C. S. Chin, X. Ji , W. L. Woo, T. J. Kwee and W. X. Yang, "Modified multiple generalized regression neural network models using fuzzy C-means with principal component analysis for noise prediction of offshore platform," Neural Computing and Applications, pp. 1-16, 2017, DOI. 10.1007/s00521-017-3143-0.

6.2.　　Proposed Noise Prediction using FCM-PCA-GRNNs

The proposed approach uses a validated SEA-DF model [60] validated in the Chapter 3 to train the FCM-PCA-GRNNs model. The neural networks determine the relationship between the room input variables to the total spatial equivalent sound pressure level (SPL) and average room SPL at different [118] frequencies (e.g. 125 Hz to 8000 Hz). The total equivalent SPL consists of both direct and diffuse field (or reverberant field) where the former is obtained via

MATLAB^{TM}, and later by a commercial SEA modelling software called VA-One^{TM}. It is capable to compute both the airborne and structure-borne noise from mid to high frequencies range [118]. The total equivalent noise level is the logarithmic sum of both the direct field ($L_{p,dir}$) and reverberant ($L_{p,rev}$) component as shown.

$$L_{p,tot} = 10\log\left(10^{0.1L_{p,dir}} + 10^{0.1L_{p,rev}}\right)$$ **[6-1]**

The proposed noise prediction architecture is shown in figure 6.1. The first layer (see the top of figure 6.1) models the reverberant field noise level and direct field noise level using VA-One^{TM} and MATLAB^{TM}, respectively. The experimental validations of the total or equivalent noise levels are performed before the neural networks training. The next layer (see bottom of figure 6.1) requires the total equivalent SPL and the input variables (p-dimensional) from the acoustic and structure features of the offshore platform compartments. The Fuzzy C-Means clustering on the available input data can help to identify a natural group (with reduced l-dimensional in each cluster) from the data set of N=424 samples (for each frequency range 125Hz, 250Hz, 500Hz, 1000Hz, 2000Hz, 4000Hz and 8000Hz) to obtain a concise representation of a system's input-output behaviour. The PCA (with reduced k-dimensional for each cluster) is performed on these clusters, followed by the GRNNs training. The spread parameter σ_0 for each GRNN produces the desired results for the cross validation set, an updated spread parameter $\sigma_i = \sigma_0 + i \times \theta$ (where θ is the learning factor and i is the number of iteration) will be used. The optimisation of spread parameter will terminate when the mean squared error (MSE) of the cross validation set is less than the desired error e_0. The final GRNNs will be built using the optimal spread parameter, followed by testing it with a validation set data. With the FCM-PCA-GRNNs model for each frequency established, it can predict the corresponding total equivalent SPL in any compartments on any similar type of offshore platform.
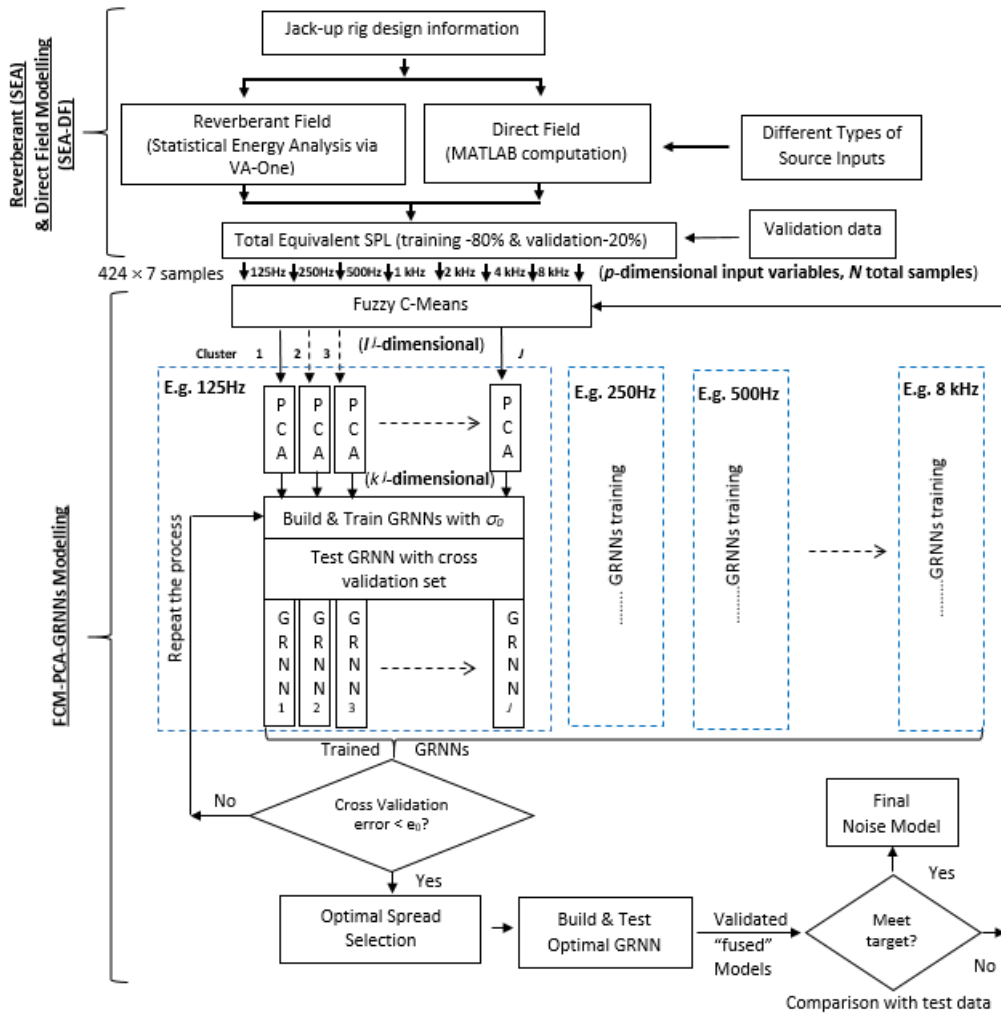
Figure 6.1 Proposed architecture for noise prediction using FCM-PCA-GRNNs **[119]**

6.3.   Selection of input parameters for FCM-PCAGRNNs

The input variable for FCM-PCA-GRNNs training is selected based on two main principles: (1) parameters that describe the acoustics and structure features of the offshore platform, and (2) parameters that influence the response of the sound fields. This information will require a prior understanding of the acoustic problem on the board of the jack-up rig at a different frequency. In addition, the acoustic environment on the jack-up rig is quite complex due to its large number of noise and vibration sources distributed quite closely within a compact space, and the use of wide variety of different materials for wall's construction. Noise is transmitted via an airborne and structure-borne transmission. The airborne noise governs the compartment's sound field where the high noise level machinery is concentrated. In general, the SPL measured in the airborne-dominated compartments can be approximated by the Heerema and Hodgson empirical formula [67] [60]. The formula used to determine the room sound pressure level is directly related to the room geometry, source power level, source–receiver distance, absorption coefficient, and fitting density of the source room. The strong

96

airborne noise in the source room can penetrate through the common bulkheads or decks to influence the noise in the adjacent rooms. The transmitted acoustic energy depends on the incident acoustic energy and transmission loss which is determined by the plate material properties and thickness as shown.

$$L_{adj} = L_{source} - R_0 + 10\log\frac{S_C}{S_{adj}\alpha_{adj}} \qquad \text{[6-2]}$$

where L_{adj} and L_{source} are the SPL of the adjacent room and source room, respectively. R_0 and S_C are the transmission loss and surface area of the common bulkhead/deck, respectively. Here α_{adj} is the mean absorption coefficient of the adjacent room. In some cases where the SPL within the source and the adjacent room are not known, the range of SPL is provided by the regulation namely NORSOK S-002 for eight different room types based on the permitted noise levels on-board of the offshore platform as seen in table 6.1.

On the other hand, the structure-borne sound is directly caused by vibrating machinery-induced mechanical force, or indirectly by the structure excitation due to incident airborne noise. The energy radiated by structures is proportional to the plate's radiation efficiency, surface area, density, sound propagation speed, and the square of plate vibration velocity. The structure-borne sound affected the remote rooms and attenuated as distance increases. The structure-borne SPL can be expressed as.

$$L_{SB} = L_V + 10\log\sigma + 10\log\frac{S\alpha}{4S} \qquad \text{[6-3]}$$

where L_{SB} is the structure-borne SPL, L_V denotes the structure vibration level, σ is the radiation efficiency, S and α are the structure surface area and room absorption coefficient, respectively.

Room Type (1 to 8)	Descriptions	Compartments	Permitted Noise Level (dBA)
1	Unmanned machinery room	Engine room, fire pump room, emergency generator room, thruster room	110
2	Unmanned machinery room	AHU room	90
3	Manned machinery room	Switchboard room, transformer room, drill floor, mud room, mixing area, pipe rack, general process and utility area, pump room, cement room	85
4	Unmanned instrument room	Local instrument room, electrical MCC room	75
5	Store, workshop, instrument room	Mechanical/Electrical workshop, paint store, LQ stores, dish washing	70
6	Living quarter public area	change room, LQ corridor, toliets	60-65
7	Living quarter public area, Lab, local control room	Local control room, lab, gally, mess room, workshop office, Gymnasium, lobby	50-60
8	Cabin, hospital, central control room	Cabin, hospital, wheel house control room	45

Table 6.1 Room types defined for compartment on-board [119]

The acoustic field in the compartments behaves differently. For example, the machinery compartments contain airborne source radiation (e.g., engine room, mud pump room); structure-borne and transmission noise (e.g., workshops, stores); and airborne, structure-borne and transmission noise (e.g., pump room, transformer room). Due to the good isolation strategies and damping treatment, the SPL in the living quarter is usually dominated by the air-conditioning diffuser radiated noise. The mechanical diffusers are typically found in heating, ventilating, and air-conditioning systems (HVAC). Some room adjacent to the

machinery compartments is affected by the transmitted structure-borne noise. As a result, the compartments in the offshore platform can be classified into five general groups:

- Compartments dominated by the airborne noise
- Compartments influenced by the structure-borne and transmission noise
- Compartments influenced by airborne and structure-borne noise
- Compartments influenced by airborne and transmission noise
- Compartments influenced by airborne, structure-borne and transmission noise simultaneously

Based on the above acosutic analysis, several main parameters that determine the spatial and spatial average SPL of the room on the offshore platform can be obtained. These includes the following 13 inputs and two output parameters: (1) total interior source power level; (2) room type; (3) room surface area; (4) room volume; (5) first nearest source sound power level; (6) source/receiver distance from the first source; (7) second nearest source sound power level; (8) source/receiver distance from the second source; (9) room mean absorption coefficient; (10) maximum sound power level of adjacent rooms; (11) panel or insulation thickness; (12) room type of the adjacent room; (13) number of decks to the main deck; (14) spatial SPL; and (15) average spatial SPL.

6.4. Case study on real offshore structure

The hull dimensions of the jack-up rig [9] involved in the study are approximately 88.8 m (length) x 115.1 m (width) x 12 m (height) as seen in figure 6.2 (a). There are four aspects of developing a SEA model shown in figure 3.14: (a) the structure properties and configurations; (b) designed noise control treatment; (c) the source information; and lastly (d) the frequency range. The offshore platform are mainly made of steels modelled by a ribbed plate with the specific properties in the construction drawing. The interior of each compartment in the offshore platform is treated as a 'cavity' which represents one acoustic subsystem of SEA model. These air cavities together with structural subsystem such as six walls around the room are connected to one another by point, line, and surface area junctions which enable the energy flow within the entire SEA model. The sound pressure level, sound power level, and vibration level of equipment are obtained from the vendor during the factory acceptance test (FAT) at 100% of the nominal load. The absorbing effects of the applied insulation layers in all compartments are obtained from reverberation time (T60) measurement. For the damped acoustic spaces, the SEA model is based on the assumption of reverberant energy. It is

important to separate the direct field component from the total energy. At steady-state condition, the final sound power injects to the reverberant field of the subsystem is as follows.

$$P_{rev}^{i} = (1 - \overline{\alpha}_{i})P_{in}^{i} \qquad [6\text{-}4]$$

where the reverberant sound power in subspace i denoted by P_{in}^{i} is reduced by a factor of $(1 - \overline{\alpha}_{i})$. Here $\overline{\alpha}_{i}$ is the mean absorption of the subspace i.

The frequency range is set from 125 to 8000 Hz after examining the number of modes present in each subsystem within the compartment. After solving the SEA energy balance equation of the jack-up rig, the reverberant SPL in each compartment is obtained. Due to the space limitation in the offshore platform compartments, equipment is distributed quite closely. The direct sound radiation from the equipment can also affect the equivalent SPL. Thus, the correct noise model of the equipment is crucial for the equivalent SPL. According to the literature [12], the marine equipment can be modeled by three types of the noise source. A point source has inverse square $\left(1/r^{2}\right)$ attenuation for small- and medium-sized equipments such as compressors, pumps, and purifiers; a rectangular surface source will generate box-like shaped contours like large machinery such as main diesel generator, mud pumps, and hydraulic pumping unit (HPU). In this study, both the reverberant and direct sound transmissions in the room are considered. The direct sound contribution from the adjacent rooms is neglected. The direct field component will be computed before adding to the reverberant field to obtain the total equivalent SPL using (1). A total number of 424 input and output samples at the seven frequencies are obtained from different rooms on the jack-up rig as shown in figure 6.2. For clarity, the input and output range of these samples are tabulated in table 6.2. Note that the abovementioned thirteen input variables (see row 1–13) and two outputs (see last two rows) are used.

Figure 6.2 jack-up rig involved in the study

6.5.   Data pre-processing using FCM-PCA

As discussed in Section 5.4, the sound transmission path in various compartments is different. By pre-processing the collected samples via data clustering can help to group samples into clusters of similar characteristics. The FCM algorithm [120-122] creates groups according to the distance between the data points and the cluster centers. Let x_i be input parameters at each frequency, e.g., 125, 250,…, 8000 Hz. The input variables of n-dimensional are denoted by $X_i = (x_{i1}, x_{i2},...x_{ip}) \in \Re^P$, $\forall i = 1,2,K,N$ forms the corresponding columns in the data matrix $X = \{X_1, X_2,...,X_N\}^T \in \Re^{N \times n}$ where N is the number of samples for each frequency as shown in figure 6.3.

No.	Input Variables and Outputs	125 Hz		250 Hz		500 Hz		1000 Hz		2000 Hz		4000 Hz		8000 Hz	
		Max.	Min.	Max.	Min.	Max.	Min.	Max.	Min.	Max.	Min.	Max.	Min.	Max.	Min.
	Inputs														
1	Total interior sound power level, (dBA)	104.6	0.0	115.2	0.0	122.0	0.0	128.0	0.0	123.0	0.0	122.0	0.0	114.0	0.0
2	Room Type	8.0	1.0	8.0	1.0	8.0	1.0	8.0	1.0	8.0	1.0	8.0	1.0	8.0	1.0
3	Room Surface Area (m2)	2052.0	39.2	2052.0	39.2	2052.0	39.2	2052.0	39.2	2052.0	39.2	2052.0	39.2	2052.0	39.2
4	Room volume, V (m3)	2160.0	16.2	2160.0	16.2	2160.0	16.2	2160.0	16.2	2160.0	16.2	2160.0	16.2	2160.0	16.2
5	First nearest source sound power levels (dBA)	101.0	0.0	112.0	0.0	119.0	0.0	125.0	0.0	120.0	0.0	119.0	0.0	111.0	0.0
6	Source/receiver distance from the first source (m)	20.0	0.0	20.0	0.0	20.0	0.0	20.0	0.0	20.0	0.0	20.0	0.0	20.0	0.0
7	Second nearest source sound power levels (dBA)	101.0	0.0	112.0	0.0	119.0	0.0	125.0	0.0	120.0	0.0	119.0	0.0	111.0	0.0
8	Source/receiver distance from the second source (m)	20.2	0.0	20.2	0.0	20.2	0.0	20.2	0.0	20.2	0.0	20.2	0.0	20.2	0.0
9	Room Mean Absorption Coefficient	0.3	0.0	0.6	0.0	0.7	0.0	0.6	0.0	0.6	0.0	0.5	0.0	0.5	0.0
10	Max Sound Power Level of adjacent room, (dBA)	104.6	0.0	115.2	0.0	122.0	0.0	128.0	0.0	123.0	0.0	122.0	0.0	114.0	0.0
11	Room Type of Adjacent Room	8.0	1.0	8.0	1.0	8.0	1.0	8.0	1.0	8.0	1.0	75.0	1.0	8.0	1.0
12	Panel/ Insulation Thickness Between Adjacent Room (mm)	75.0	0.0	75.0	0.0	75.0	0.0	75.0	0.0	75.0	0.0	75.0	0.0	75.0	0.0
13	Number of Decks to Main Deck	6.0	-2.0	6.0	-2.0	6.0	-2.0	6.0	-2.0	6.0	-2.0	6.0	-2.0	6.0	-2.0
	Outputs														
14	Spatial l SPL, (dBA)	90.5	20.4	97.2	21.0	103.3	16.2	109.4	12.9	104.5	9.9	103.9	0.0	95.9	0.0
15	Spatial Averaging SPL, (dBA)	89.8	20.4	96.5	21.0	101.6	16.2	108.0	12.9	103.0	9.9	102.6	0.0	94.6	0.0

Table 6.2 Input and output range for each input parameter [119]
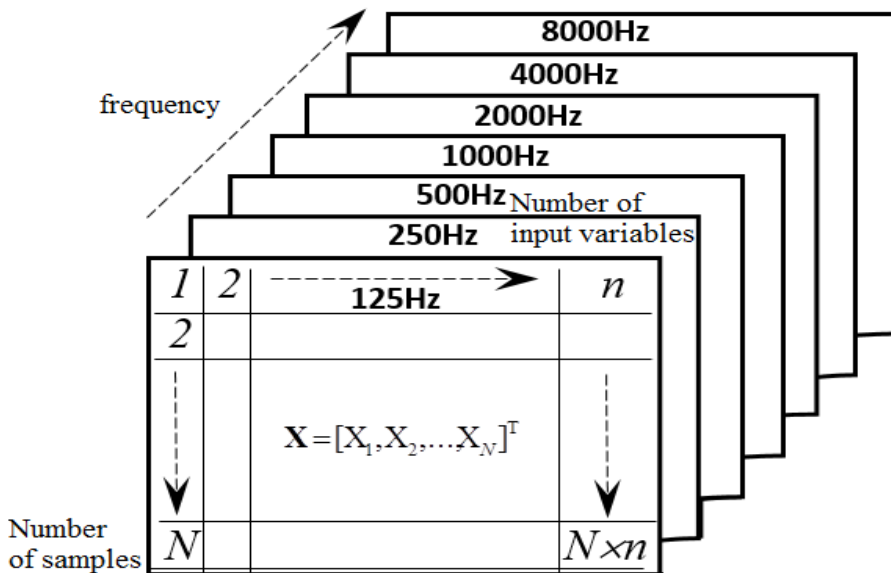

Figure 6.3 Input data matrix in three-dimensional [119]

The FCM algorithm partition the data $\mathbf{X}$ into jth clusters(denotes as $\mathbf{X}^j$) for each frequency. A fuzzy partition is represented as a matrix $\mathbf{U}$, with elements of $u_{ji} - [0,1]$, gives the membership degree in the partition. The fuzzy partitioning is carried out through an iterative

optimization of the objective function in Equation [6-7], with the update of membership for each frequency as

$$\mu_{ji} = \frac{\left(1/d^2(x_i, v_j)\right)^{1/(m-1)}}{\sum_{j=1}^{J}\left(1/d^2(x_i, v_j)\right)^{1/(m-1)}} \qquad \textbf{[6-5]}$$

and cluster centres

$$v_j = \frac{\sum_{i=1}^{N}(\mu_{ji})^m x_i}{\sum_{i=1}^{N}(\mu_{ji})^m}, \forall j = 1,2,\text{K } J \qquad \textbf{[6-6]}$$

where v_j represents the jth cluster centre, m is the fuzziness index, and $m \in (1,\infty)$ determine the fuzziness of the clusters. The number of the cluster center is denoted by J. The Euclidean distance between ith data and jth cluster's center is $d(x_i, v_j) = \|x_i - v_j\|$, and μ_{ji} accounts for the membership of ith data to j^{th} cluster center.

The main objective of the FCM algorithm is to minimise the objective function $J(\mathbf{X};\mathbf{U},\mathbf{V})$ on $\mathbf{U}$ and $\mathbf{V}$.

$$J(\mathbf{X};\mathbf{U},\mathbf{V}) = \sum_{j=1}^{J}\sum_{i=1}^{N}\mu_{ji}^m d(x_i, v_j)^2, \qquad 2 \le J < N \qquad \textbf{[6-7]}$$

where $\mathbf{V} = (v_1, v_2, \text{K}, v_J)$ is the cluster prototype that have to be determined and $\mathbf{U}$ is the fuzzy partition that must satisfies the following constraints:

$$\sum_{j=1}^{J}\mu_{ji} = 1, \forall i \quad \text{and} \quad 0 < \sum_{i=1}^{N}\mu_{ji} = \text{N}, \forall j \qquad \textbf{[6-8]}$$

The fuzzy cluster is obtained through an iterative optimisation of equation [6-7] according to the unsupervised optimal fuzzy clustering.

After setting the number of clusters $J = 5$ and the maximum number of iterations as 200, the FCM algorithm is applied to all frequency samples. The clustering results are presented in figure 6.4 a–g in the form of parallel coordinates plot to visualise and analyse multivariate data having different range and SI unit. The values of the thirteen input variables are polylines with vertices on the vertical axes. The numbers in the X-axis represent the thirteen input variables as seen in table 6.2. The position of the vertex on the ith axis corresponds to the ith coordinate of the sample [123]. For example, there exists a higher value in the sixth and eighth input within cluster 5. These high values can be contributed by the possible noise [124]

within samples collected. The sound samples which are close to the cluster centers are considered as normal samples. However, they are assigned with very low or zero membership in the cluster group. As a result, the PCA is used to reduce the dimensionality through finding the high relevance input variables for each cluster at a particular frequency.
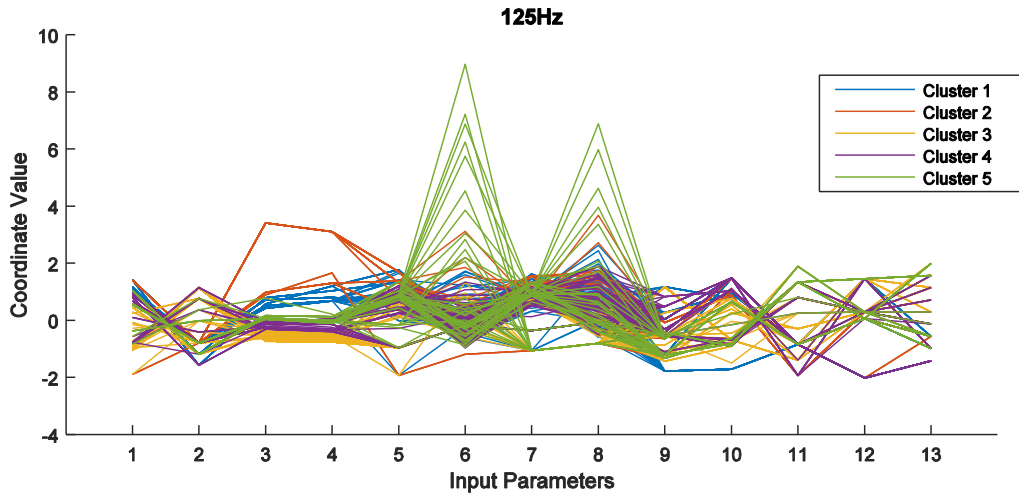
(a) 125 Hz [119]
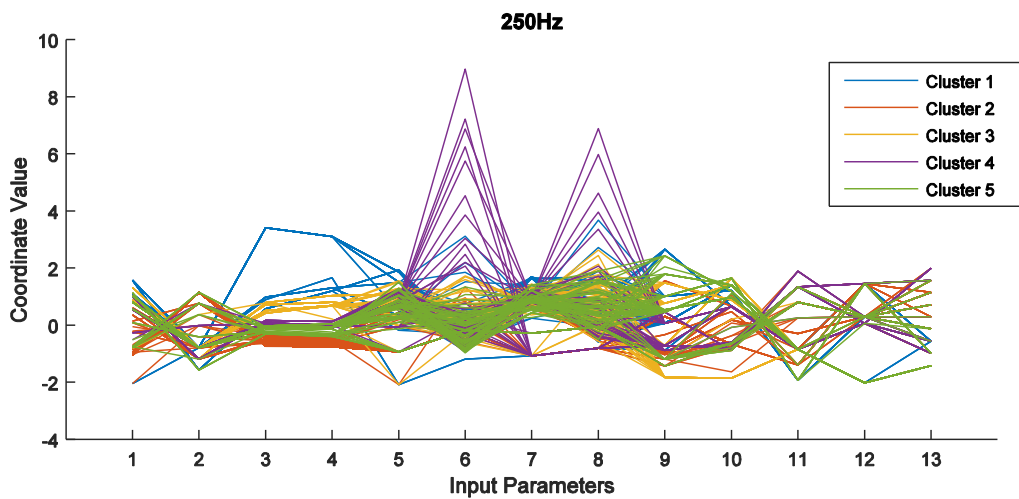
(b) 250 Hz [119]
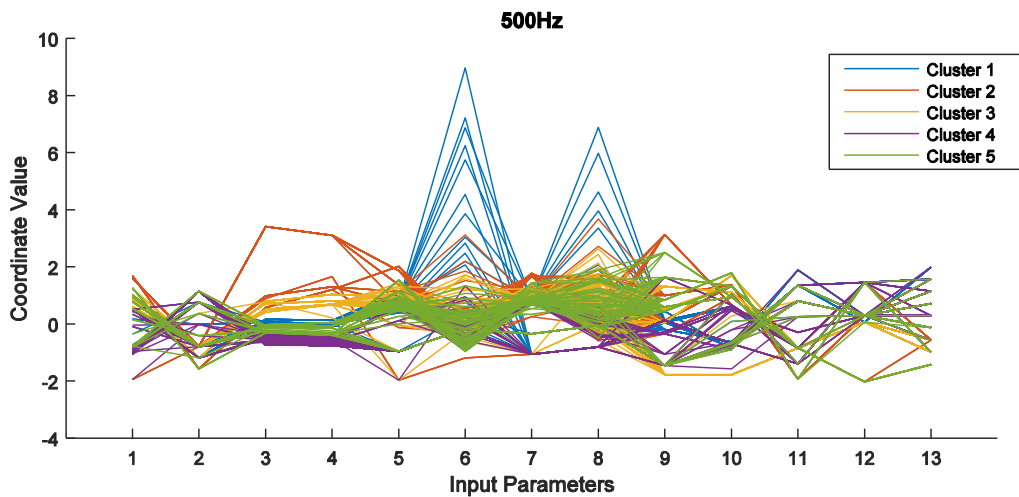
(c) 500 Hz [119]
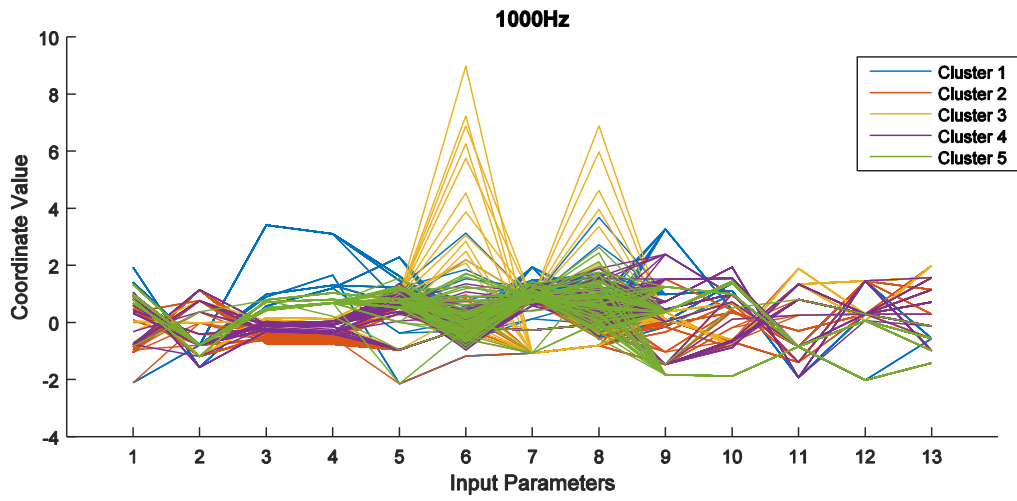
(d) 1000 Hz [119]
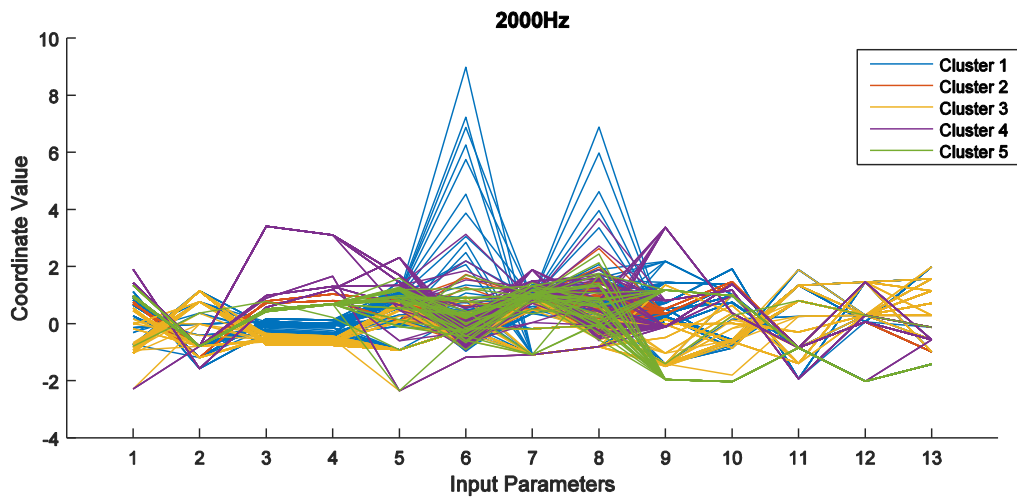
(e) 2000 Hz [119]
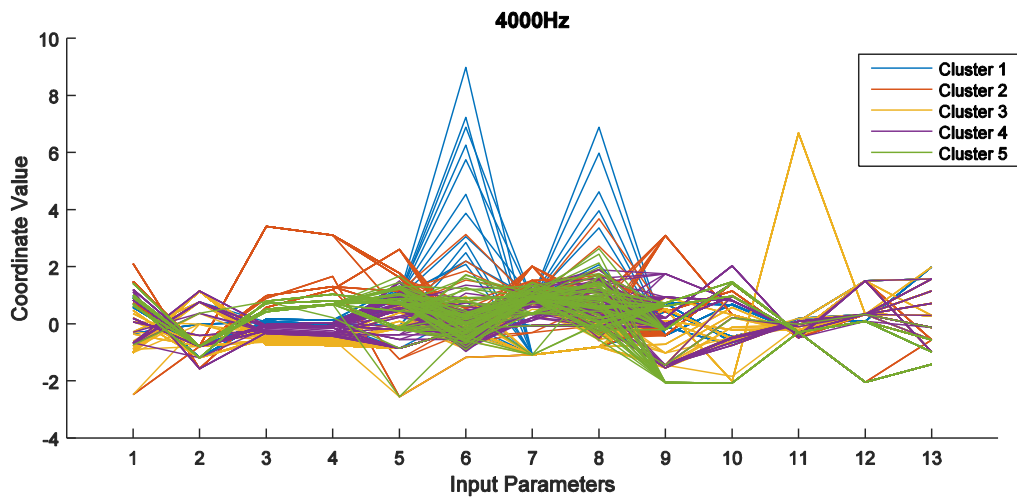
(f) 4000 Hz [119]
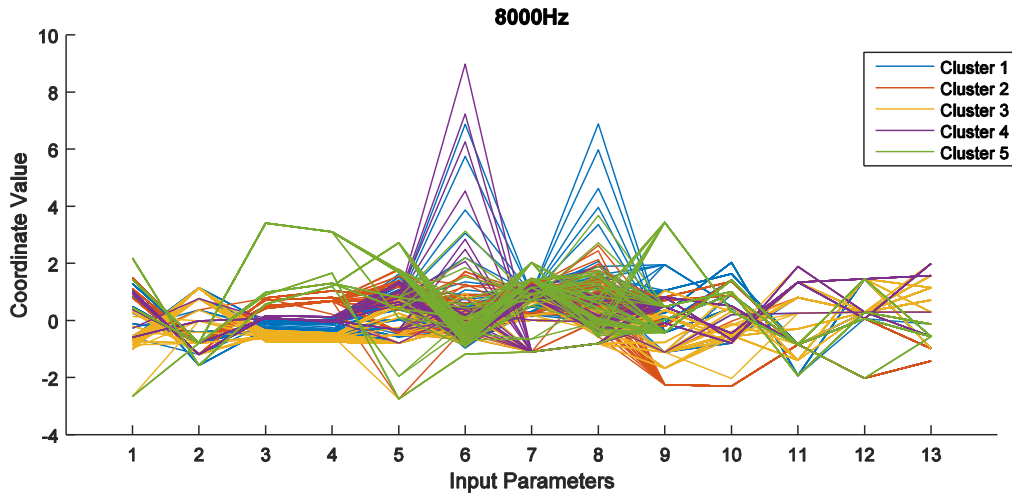
(g) 8000 Hz [119]

Figure 6.4 data distribution after FCM at each frequency

The correlations of input variables to the outputs are quite different in each cluster. The input variable selection is implemented on the data matrix $\mathbf{X}$ in jth cluster (denotes as $\mathbf{X}^j$) for each frequency to reduce the input dimension. Note that the superscript " j " will be used to define jth cluster and subscript "i" refers to the index for each sample. PCA uses the singular value decomposition (SVD) to rank the input variables in descending order of importance to least important. The most important variables are given a higher priority than the less significant ones.

Briefly, the first step in the PCA algorithm is to normalise the components such that they have unity variance and zero means. It is followed by an orthogonalisation method to determine the normalised principal components. The PCA operates on each cluster at particular frequency as follows.

- Subtract the mean of each data point in the data set $\mathbf{X}^j$ to produce a data set of zero means of a cluster $j = 1, 2, \text{K } J$ denotes as

$$\mathbf{X}^j - \overline{\mathbf{X}}^j \qquad \text{[6-9]}$$

where the mean, X_i^j is the input samples, N^j is the number of samples in the jth cluster.

Compute the square covariance matrix $\mathbf{\Omega}^j$ of size $l \times l$ for jth cluster where l is the number of reduced input variables.

- Perform singular value decomposition (SVD) on the covariance matrix $\mathbf{\Omega}^j$.

106

$$\boldsymbol{\Omega}^j = \overline{\mathbf{U}}^j \mathbf{S}^j \overline{\mathbf{V}}^{jT} \tag{6-10}$$

where $\overline{\mathbf{U}}^j$ is a $l \times l$ matrix with columns being orthonormal eigenvectors or left singular vectors of $\boldsymbol{\Omega}^j \boldsymbol{\Omega}^{jT}$, $\overline{\mathbf{V}}^{jT}$ is a $l \times l$ matrix with columns being orthonormal eigenvectors or right singular vectors of $\boldsymbol{\Omega}^{jT} \boldsymbol{\Omega}^j$ and $\mathbf{S}^j = \mathrm{diag}(s_1, \mathrm{K}, s_l)$ is a $l \times l$ diagonal matrix with only non-zero element. It is also the singular values or the square roots of eigenvalues from $\overline{\mathbf{U}}^j$ or $\overline{\mathbf{V}}^j$ positioned in descending order.

- Apply $\mathbf{U}^j, \mathbf{S}^j$, and $\mathbf{V}^j$ to determine the inverse square root of the covariance matrix.

$$\boldsymbol{\Omega}^{j-1/2} = \sum_{i=1}^{h} \frac{1}{\sqrt{\mathbf{S}_i^j}} \mathbf{U}_i^j \mathbf{V}_i^{jT} \tag{6-11}$$

where h is the number of eigenvectors for eigenvalues in $\mathbf{S}^j$

- Multiply the SVD-computed inverse square root covariance matrix as shown to obtain the reduced dimensional data set.

$$\boldsymbol{\Omega}^{j-1/2}\left(\mathbf{X}^j - \overline{\mathbf{X}}^j\right) \tag{6-12}$$

Based on the acoustic field behavior in Section 5.4, the samples are grouped into five clusters at different center frequencies using the FCM. The PCA is then applied to each cluster to determine the number of principal components. In this study, the cumulative percentage of variance criteria is applied to determine the number of principal components. According to this criterion, principal components are chosen based on their cumulative proportion of variance higher than a prescribed threshold value of 95%. The leverage scores for each dimension are obtained by calculating their two norms. Figure 6.5 shows the norm for the thirteen input parameters at each frequency. The different heights shown on the respective bar charts reflect the dominant input parameters used for each cluster. The dominant input parameters are only retained in each cluster thus reduces the problem dimension and eliminates the relativity between the input parameters.
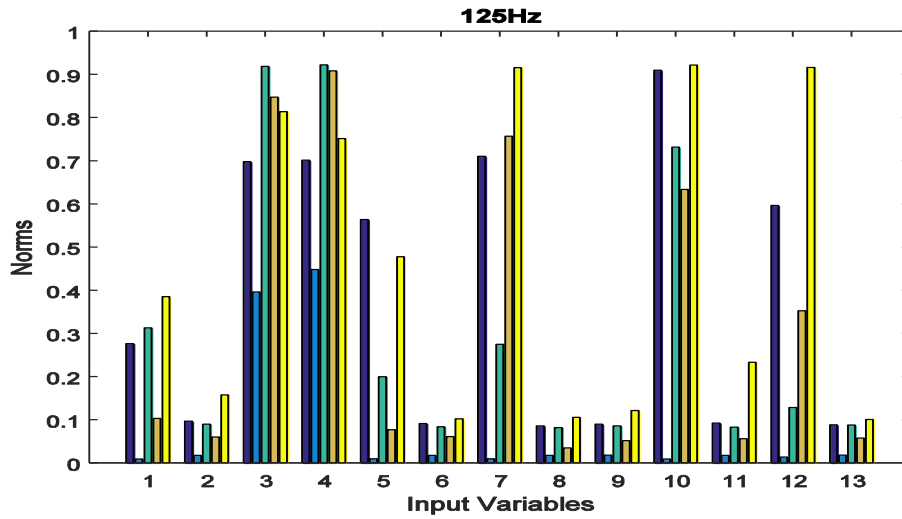
(a) 2-norm distribution for input parameter across each cluster group at 125 Hz [119]
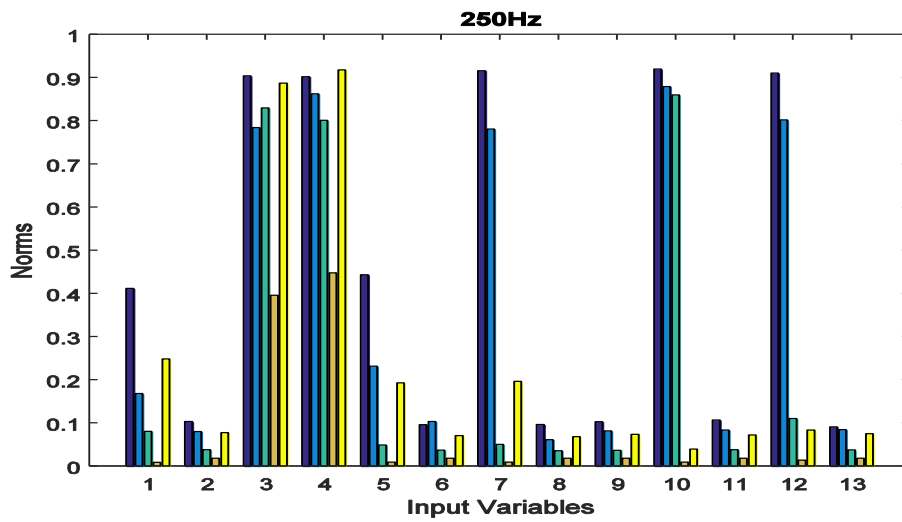
(b) 2-norm distribution for input parameter across each cluster group at 250 Hz [119]
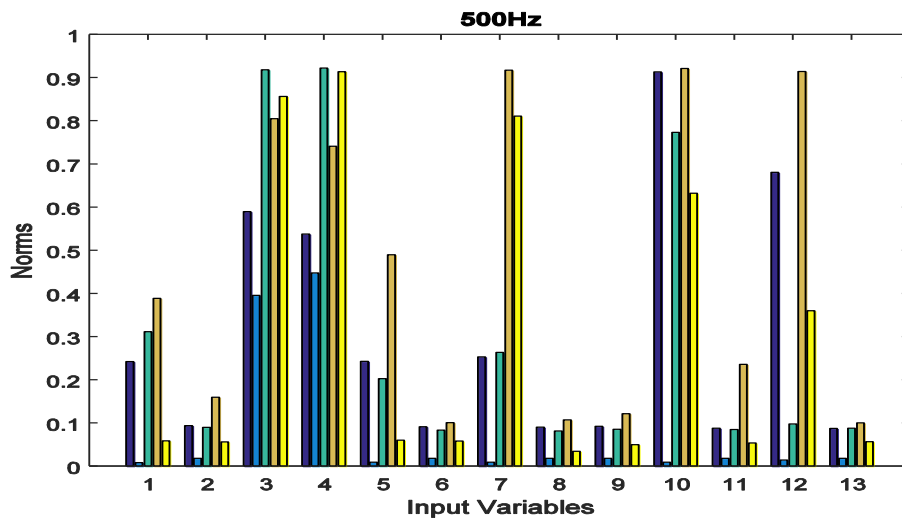
(c) 2-norm distribution for input parameter across each cluster group at 500 Hz [119]
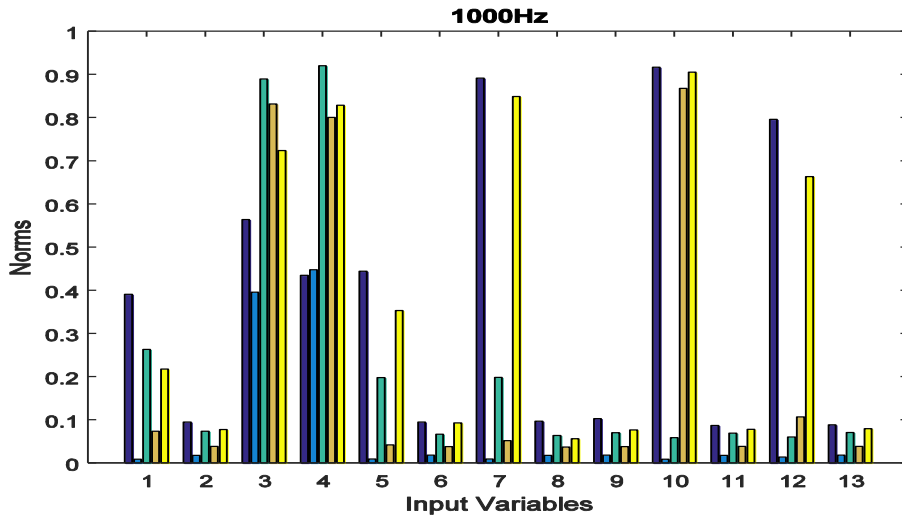
(d) 2-norm distribution for input parameter across each cluster group at 1000 Hz [119]
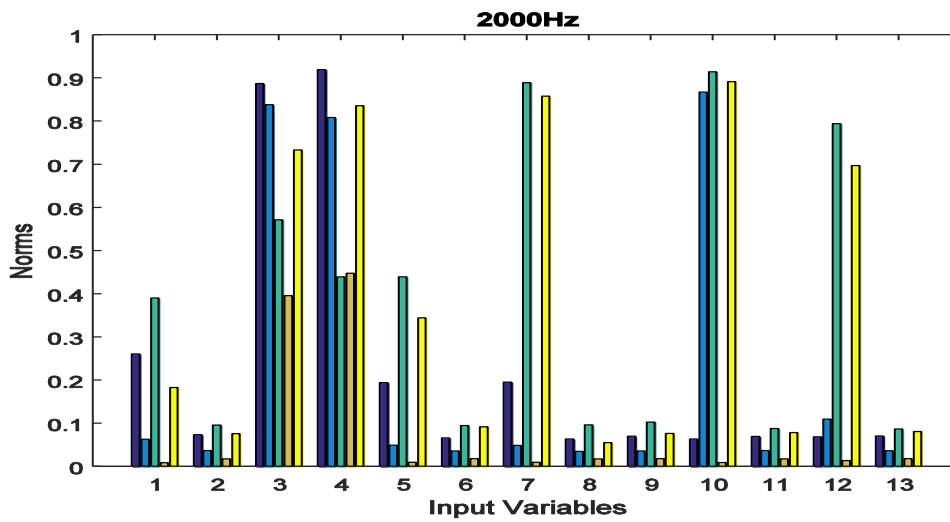
(e) 2-norm distribution for input parameter across each cluster group at 2000 Hz [119]
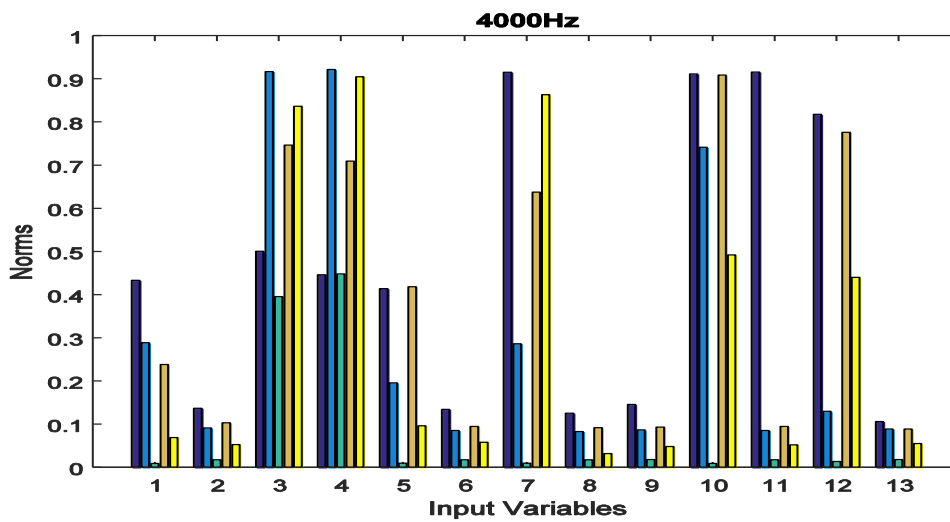
(f) 2-norm distribution for input parameter across each cluster group at 4000 Hz [119]
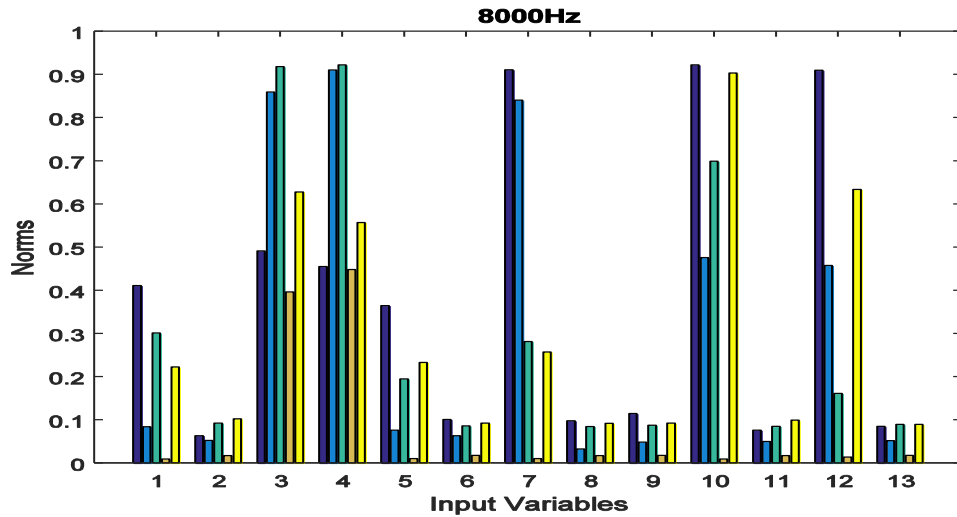
(g) 2-norm distribution for input parameter across each cluster group at 8000 Hz [119]

Figure 6.5 Leverage scores of each input parameter for each cluster group at different frequencies (cluster 1: dark blue, cluster 2: blue, cluster 3: cyan, cluster 4: Orange, and cluster 5: yellow) **[119]**

As shown in figure 6.5, the significant principal components are identified. The principal components below the predetermined threshold value are removed. The remaining input variables should contain the most dominant variables for GRNN training. Table 6.3 summarises the result of figure 6.5, and ''x'' refers to variable removed while ''o'' refers to the dominant variables to retain for GRNN training. For example, the seven remaining input variables for cluster 1 at 125 Hz are the total sound power level, room surface area, room volume, nearest source#1 sound power level, nearest source#2 sound power level, maximum sound power level of adjacent room, and panel/insulation thickness between adjacent rooms. Due to the unsupervised characteristics of the FCM and application of PCA, the importance of the input variables (or a number of dominant parameters) in each cluster varies across the frequencies. Note that the reduced sample size used for the GRNN's training is different in each cluster for the frequencies.

6.6. Model of multiple GRNN after FCM-PCA

The GRNN (see figure 6.6) is one type of radial basis function (RBF) networks based on the kernel regression [111] and is a robust regression tool for its strong nonlinear mapping capability and high training speed. Also, it overcomes the shortcoming of back propagation neural network which needs a large number of training samples. It is suitable for a problem with limited training samples, and GRNN has been proved to be a useful tool to perform prediction and comparison in many fields [115][125-126]. Briefly, the structure of GRNN is composed of four layers: an input layer, a pattern layer, summation layer, and output layer.

110

The first input layer consists of reduced input variables from FCM PCA pre-process that connected to the second pattern layer. The neurons in the pattern layer can memorise the relationship between the neuron of entry and the proper response of pattern layer. The two summations S_s and S_w in the summation layer compute the arithmetic sum of the pattern outputs with the interconnection weight equals to one and compute the weighted sum of the pattern layer outputs with the interconnection weight, respectively. The neurons in the summation layer are then summed and fed into the output layer. The number of the neurons in the output layer equals to the dimension of the output vector. Since there are five clusters in each frequency, there are a total number of thirty-five GRNN predictors for the seven frequencies.
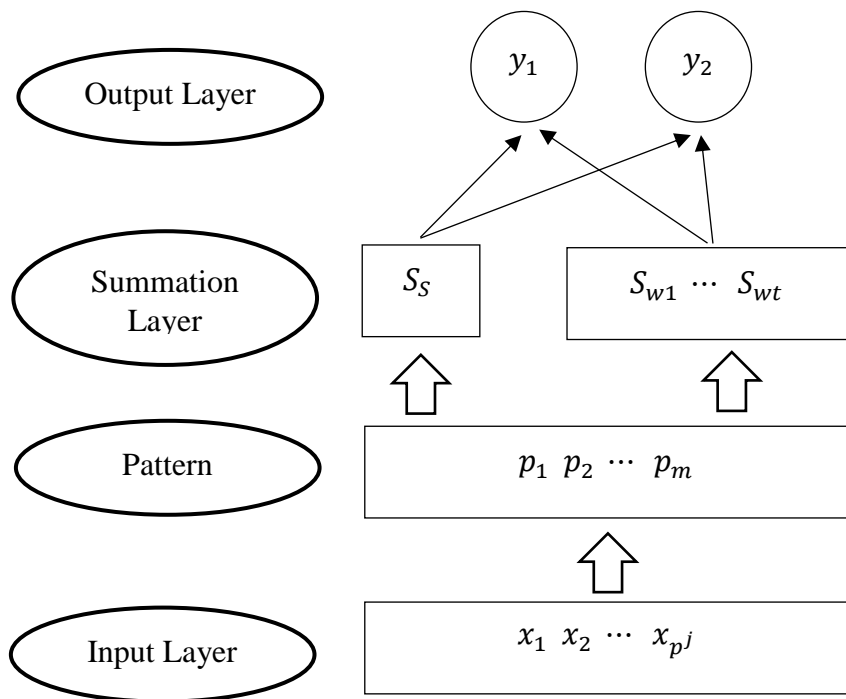

Figure 6.6 Architectural implementation of multiple GRNN after FCMPCA **[119]**

Freq. (Hz)	Clusters	Total sound power level, (dBA)	Room Type	Room Surface Area (m2)	Room volume, V (m3)	Nearest Source 1 SWL, (dBA)	Dist. To Nearest source 1, (m)	Nearest Source 2 SWL, (dBA)	Dist. To Nearest source 2 (m)	Mean Absorption Coefficient	Max Sound Power Level of adjacent room, (dBA)	Room Type of Adjacent Room	Panel/ Insulation Thickness Between Adjacent Room (mm)	Number of Decks to Main Deck
	1	O	X	O	O	O	X	O	X	X	O	X	O	X
	2	X	O	O	O	X	O	X	O	O	X	O	X	O
125	3	O	X	O	O	O	X	O	X	X	O	X	O	X
	4	O	X	O	O	O	X	O	X	X	O	X	O	X
	5	O	O	O	O	O	X	O	X	X	O	O	O	X
	1	O	X	O	O	O	X	O	X	X	O	X	O	X
	2	O	X	O	O	O	X	O	X	X	O	X	O	X
250	3	O	X	O	O	X	X	X	X	X	O	X	O	X
	4	X	O	O	O	X	O	X	O	O	X	O	X	O
	5	O	O	O	O	O	O	O	X	O	X	O	O	O
	1	O	O	O	O	O	X	O	X	X	O	X	O	X
	2	X	O	O	O	X	O	X	O	O	X	O	X	O
500	3	O	X	O	O	O	X	O	X	X	O	X	O	X
	4	O	O	O	O	O	X	O	X	X	O	O	O	X
	5	X	X	O	O	X	X	O	X	X	O	X	O	X
	1	O	X	O	O	O	X	O	X	X	O	X	O	X
	2	X	O	O	O	X	O	X	O	O	X	O	X	O
1000	3	O	O	O	O	O	X	O	X	O	X	X	X	O
	4	O	X	O	O	X	X	O	X	X	O	X	O	X
	5	O	X	O	O	O	X	O	X	X	O	X	O	X
	1	O	O	O	O	O	X	O	X	O	X	O	X	O
	2	O	X	O	O	O	X	O	X	X	O	X	O	X
2000	3	O	X	O	O	O	X	O	X	X	O	X	O	X
	4	X	O	O	O	X	O	X	O	O	X	O	X	O
	5	O	X	O	O	O	X	O	X	X	O	X	O	X
	1	O	X	O	O	O	X	O	X	O	O	O	O	X
	2	O	X	O	O	O	X	O	X	X	O	X	O	X
4000	3	X	O	O	O	X	O	X	O	O	X	O	X	O
	4	O	X	O	O	O	X	O	X	X	O	X	O	X
	5	X	X	O	O	O	X	O	X	X	O	X	O	X
	1	O	X	O	O	O	X	O	X	X	O	X	O	X
	2	O	X	O	O	O	O	O	X	X	O	X	O	X
8000	3	O	X	O	O	O	X	O	X	X	O	X	O	X
	4	X	O	O	O	X	O	X	O	O	X	O	X	O
	5	O	O	O	O	O	X	O	X	X	O	O	O	X

Table 6.3 Selection of input variables in clusters. ''x'' refers to variable removed while ''o'' refers to the dominant variables to retain for subsequent GRNN training [119]

The primary function of GRNN [111] is to estimate a linear or nonlinear regression surface on independent variables. It assumes the continuous probability density function $f(\mathbf{X}^j, y^j)$ has a random variable $\tilde{\mathbf{X}}^j$ and $\tilde{y}^j$. The corresponding regression of y^j on $\mathbf{X}_i^j$ is given by:

$$E\left[y^j / \mathbf{X}^j\right] = \frac{\int_{-\infty}^{\infty} y^j f(\mathbf{X}^j, y^j) dy}{\int_{-\infty}^{\infty} f(\mathbf{X}^j, y^j) dy} \qquad \textbf{[6-13]}$$

where $\mathbf{X}^j$ refers to the data matrix $\mathbf{X}$ in jth cluster.

The probability density function $f(\mathbf{X}^j, y^j)$ is estimated by Parzen nonparametric estimator from $\mathbf{X}^j$ and y^j in reduced $\overline{N}^j$ observation samples (less than the initial number of samples, N^j in each cluster), l^j (less than the initial number of input variables, n in each cluster). The probability estimator $\hat{f}(\mathbf{X}^j, y^j)$ is based on the sample values $\mathbf{X}^j$ and y^j of the random variable $\tilde{\mathbf{X}}^j$ and $\tilde{y}^j$, respectively. The probability density function $\hat{f}(\mathbf{X}^j, y^j)$ [111] is expressed as

$$\hat{f}(\mathbf{X}^j, y^j) = \frac{1}{(2\pi)^{\frac{l^j+1}{2}} \sigma^{l^j+1}} \cdot \frac{1}{\overline{N}^j} \sum_{i=1}^{\overline{N}^j} \exp\left[-\frac{\left\|\mathbf{X}^j - \tilde{\mathbf{X}}^j\right\|}{2\sigma^2}\right] \cdot \exp\left[-\frac{\left\|y^j - \tilde{y}^j\right\|}{2\sigma^2}\right] \qquad \textbf{[6-14]}$$

A spread parameter r is assigned to $\mathbf{X}^j$ and y^j of jth cluster. The resulting regression[2] in equation [6-15] involves summations over the observations.

$$\hat{Y}^j(\mathbf{X}^j) = \frac{\sum_{i=1}^{\overline{N}^j} y^j \exp\left(-\frac{D_i^{j\,2}}{2\sigma^2}\right)}{\sum_{i=1}^{\overline{N}^j} \exp\left(-\frac{D_i^{j\,2}}{2\sigma^2}\right)} \qquad \textbf{[6-15]}$$

where the two norms of scalar function $D_i^{j\,2} = \left\|\mathbf{X}^j - \tilde{\mathbf{X}}^j\right\|$

The 'spread' refers to the spread of radial basis functions which plays a significant role in FCM-PCA-GRNNs function approximation [111]. The larger spread gives a smoother function approximation while the smaller spread fits the data closely. The optimal spread variables can be selected based on prior knowledge or intelligent optimisation algorithms [114]. In this study, a k-fold cross validation method is used to find the corresponding spread parameter for each neuron based on the training samples in the clusters. The selected value of spread parameter is chosen once the error of the validation data starts to increase. It is the point where overtraining of the network may occur. The mean squared error (MSE) criteria

measure the difference between the estimated and target. An updated spread parameter $\sigma_i = \sigma_0 + i \times \theta$ with θ is the adjustable learning factor and i is the current loop index.

In each cluster, the data samples are randomly divided into training and validation set with the following weighting of 80 and 20%, respectively, for each cluster (see figure 6.1). The validation set is used as an additional independent measurement to estimate the quality of the trained network. In the k-fold cross-validation, the original sample is randomly partitioned into similar-sized subsamples. In the subsamples, one subsample is used as the validation data for testing the model, and the remaining subsamples as training data. After a maximum of four iterations (from 0.01 to 3 with a step size of 0.01) for each cluster at 125, 250, 500, 1000, 2000, 4000, and 8000 Hz, the optimal spread variables that give the minimum MSE are chosen. For the sake of clarity, figure 6.7 illustrates the MSE of five clusters across different spread variables ranging 0.01–3 for 125 to 8000 Hz. The optimal spread variables for each group are different. Typically, the FCM PCA-GRNNs tend to perform better with a smaller the spread parameter than a larger value. As a result, the optimal spread parameter is approximately 0.001 for all frequencies.
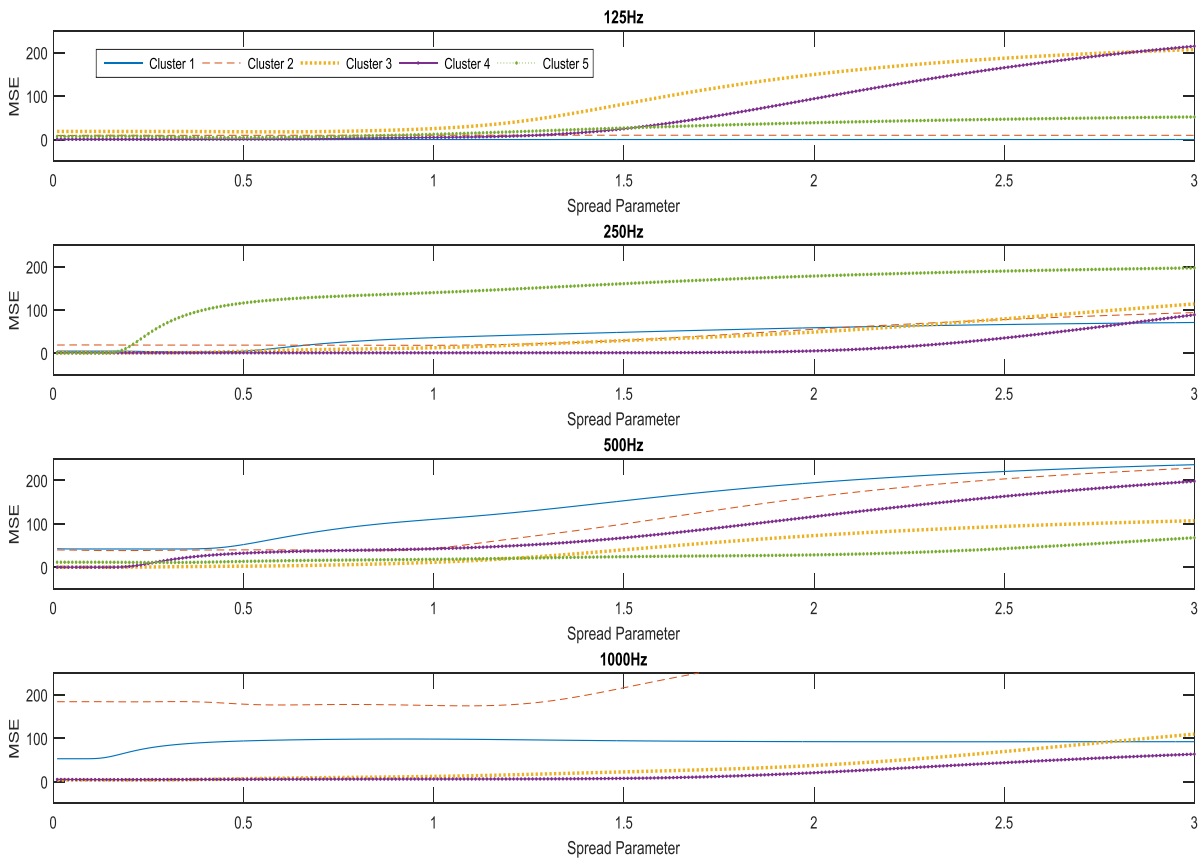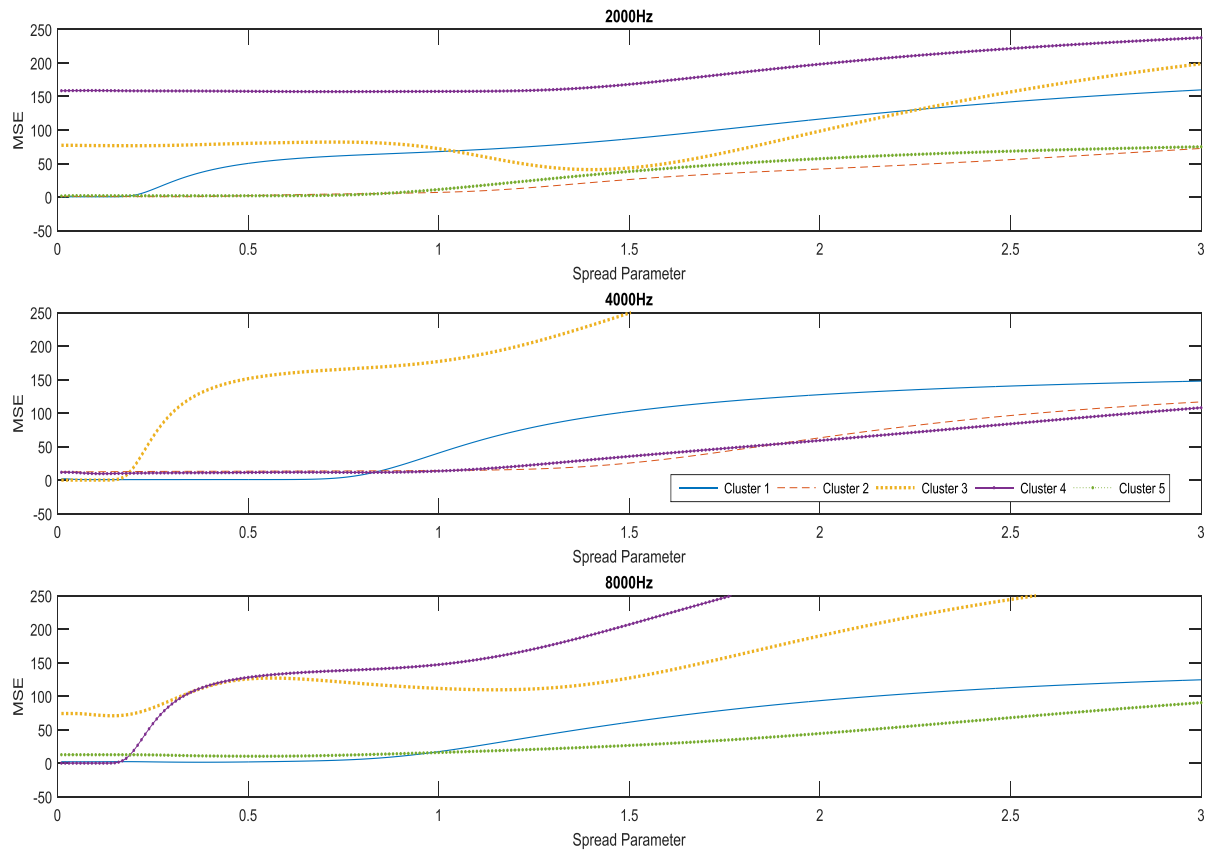
Figure 6.7 MSE of five clusters in 125 to 8000 Hz after FCMPCA-GRNN **[119]**

6.7.   **Results and discussion**

The data samples are randomly divided into training and validation set with the following weighting of 80 and 20%, respectively, for each cluster (see the earlier proposed architecture in figure 6.1). The optimal spread parameters are determined in Section 6.6, and the predicted SPLs are compared with the SEA-DF simulation from the validation set. The comparisons of spatial SPL and spatial average SPL are compared in the following octave frequency bands: 125, 250, 500, 1000, 2000, 4000, and 8000 Hz as shown in figure 6.8. The predicted, simulated spatial SPL and spatial average SPL are compared. The maximum and minimum noise levels, data distribution, and the data mean are quite consistent. The results imply the proposed FCM-PCA-GRNNs is able to predict the SPL quite accurately as compared with the SEA-DF simulation.
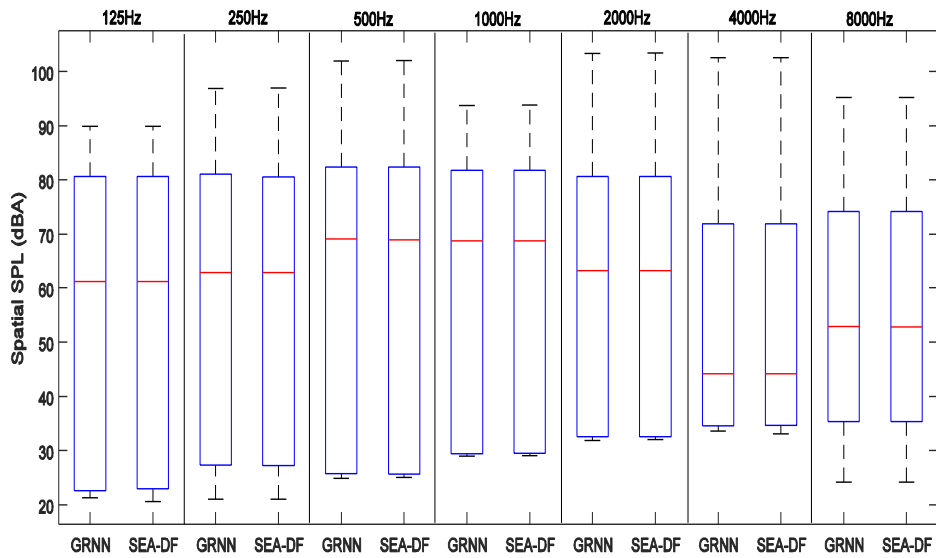
(a) Spatial SPL
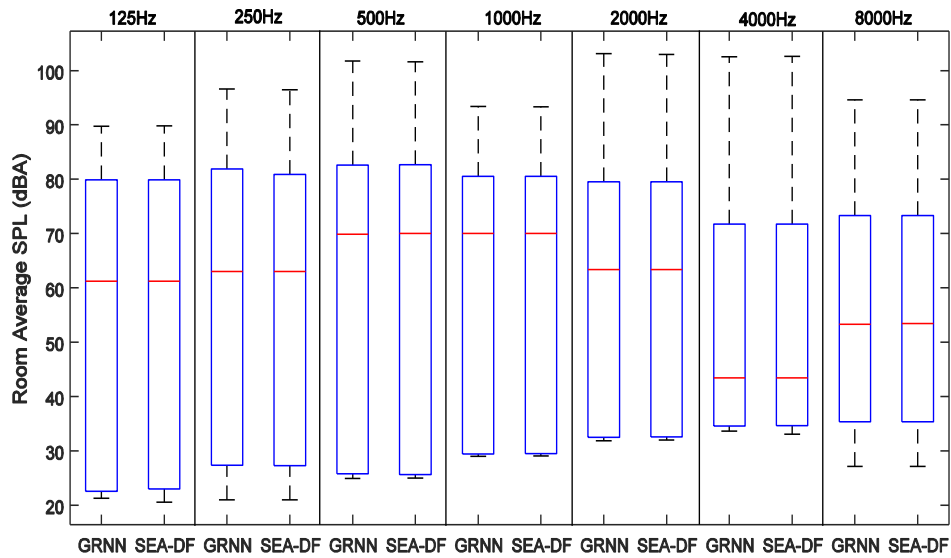
(b) Spatial average SPL

Figure 6.8 Comparisons between FCM-PCA-GRNNs prediction and SEA-DF simulation [119]

As seen in table 6.4, the maximum and the mean value of the errors at each frequency are tabulated to analyse the prediction performance of the proposed method. Table 6.4 presents the worst possible prediction results for spatial and spatial average occur at 1000 Hz. The errors of 1.8 and 1.75 dB can be determined in the maximum spatial and spatial average, respectively. The mean errors of the spatial and spatial average are 0.04 dB (8000 Hz) and 0.025 dB (4000 Hz), respectively. The error is well below the accepted limit of 3 dB for

engineering survey method. As seen in the prediction error tabulated in table 6.5, the error of FCM-PCA-GRNNs is quite small as compared to GRNNs for the spatial average at each frequency. The proposed FCM-PCA-GRNNs approach can predict the spatial and the spatial average noise level. Note that the training and validation sets are selected randomly such that the cross-validation can select the optimal spread value for each run. It ensures the proposed FCM- the PCA-GRNNs model is an optimal and robust for the data set.

Centre Frequency	Error (dB)			
(Hz)	Max Spatial	Mean Spatial	Max Spatial Average	Mean Spatial average
125	0.9	-0.016	0.9	0.02
250	0.7	0.01	0.7	-0.02
500	1.4	-0.01	1.3	-0.02
1000	1.8	0.03	1.75	0.01
2000	1.1	-0.02	1.05	0.02
4000	0.6	0.007	0.55	0.025
8000	0.7	0.04	0.66	0

Table 6.4 Summary of prediction errors between FCM-PCA-GRNNs and SEA-DF [119]

The use of FCM-PCA on samples has significantly improved the multiple GRNN models performance, i.e., FCM-PCA-GRNNs. Table 6.5 presents the average absolute prediction error for the spatial SPL and spatial average SPL before and after using FCM-PCA. It shows the improvement in the spatial error of 0.14–0.42 dB, while the improvement in the spatial average error is 0.21–0.43 dB. Additionally, the error fluctuation in different frequencies has been reduced. By defining the percentage of improvement, figure 6.9 shows an average percent improvement of minimal 25 and 85% in spatial and spatial average SPL, respectively, across all the frequencies. With the optimal GRNNs obtained, the use of FCM-PCA to pre-processing the input parameters enhances the reliability and robustness of the prediction model as more relevant parameters and multiple GRNN models are used.

The proposed FCM-PCA-GRNNs model performance is further evaluated by the actual measurement using the real engine room case study [60]. The structural and acoustic information of the engine room associated with the thirteen input variables is collected as the test samples. The frequency-dependent spatial SPL and spatial average SPL are directed mapped. As shown in figure 6.10, the result from FCM-PCA-GRNNs model is compared with the empirical acoustic models such as Thompson model (L1), Kuttruff model (L2), SNAME

method (L3), Heerema and Hodgson model (L4), Sergeyev model (L5), and SEA-DF. It shows that FCM-PCA-GRNNs noise model exhibits at least 16% less error than the SEA-DF and empirical-based acoustic models. In summary, FCM-PCA-GRNNs provides a comparable and more robust model for noise prediction at much lower cost as compared to commercial CAD modeling using SEA-based software.

Frequency	Description	Output (dB)		Error (dB)		Improvement%	
		Spatial	Room Average	Spatial	Room Average	Spatial	Room Average
125Hz	GRNN	0.62	0.50	0.38	0.43	61	86
	FCM-PCA-GRNNs	0.24	0.07				
250Hz	GRNN	0.54	0.29	0.19	0.25	35	86
	FCM-PCA-GRNNs	0.35	0.04				
500Hz	GRNN	0.73	0.33	0.37	0.30	50	90
	FCM-PCA-GRNNs	0.36	0.03				
1000Hz	GRNN	0.56	0.33	0.21	0.32	37	96
	FCM-PCA-GRNNs	0.35	0.01				
2000Hz	GRNN	0.54	0.25	0.14	0.21	25	86
	FCM-PCA-GRNNs	0.40	0.04				
4000Hz	GRNN	0.68	0.44	0.42	0.43	62	98
	FCM-PCA-GRNNs	0.26	0.01				
8000Hz	GRNN	0.46	0.27	0.19	0.26	40	96
	FCM-PCA-GRNNs	0.27	0.01				

Table 6.5 Model performance with and without FCM-PCA pre-processing [119]
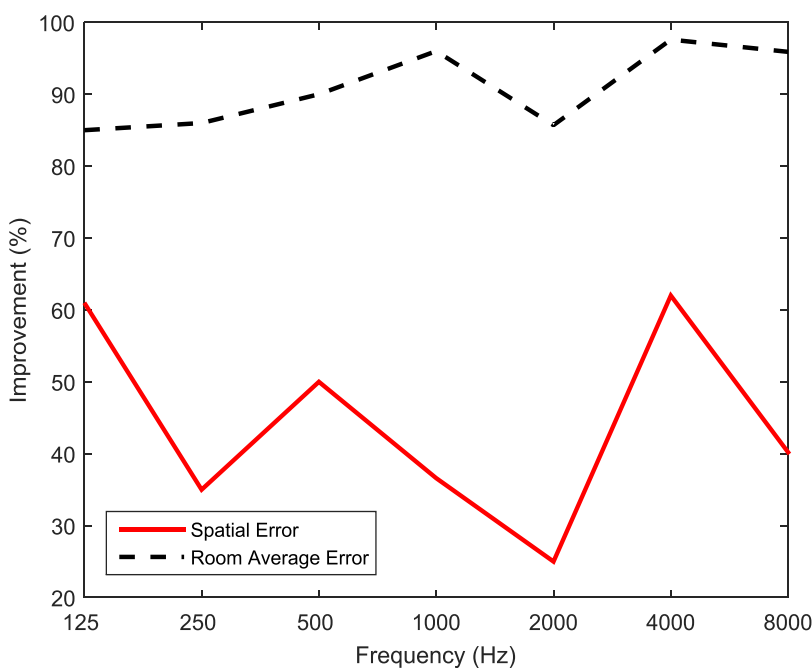
Figure 6.9 Performance improvement for FCM-PCA-GRNNs as compared to GRNNs only [119]
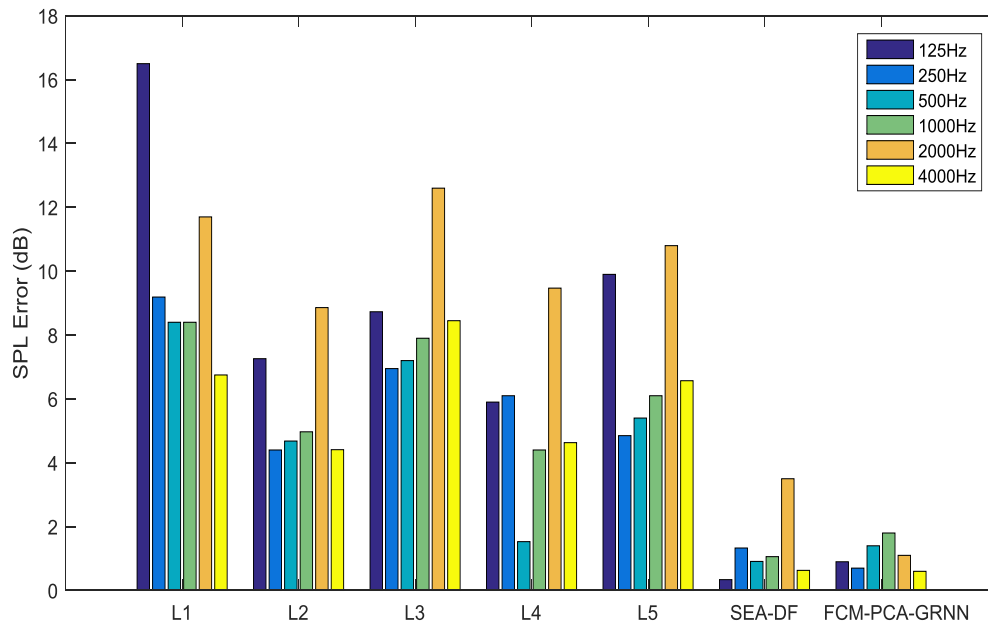
Figure 6.10 Prediction error between FCM-PCA-GRNNs, SEA-DF, and empirical acoustic models for engine room [119]

6.8. Conclusion

This chapter proposed a combined fuzzy and neural network method to predict the sound pressure level in the offshore platform. With the training and testing samples collected based on SEA-DF method validated in the Chapter 3, the FCM-PCA is firstly implemented to group the data samples into clusters with less and more relevant input variables by removing the less correlated parameters from the clusters in each frequency. The comparison results show that, this pre-process improved the result accuracy by approximately 0.14–0.42 dB and 0.21–0.43 dB. The spread parameters are identified by cross validation with minimum root mean squared error to ensure the FCM-PCA-GRNNs are an optimal and reliable predictor for the multiple frequency-dependent data. In the engine room case, the FCM-PCA on the fused multiple GRNN models exhibits less than 16% in the SPL error as compared to commercial acoustic software using statistical energy analysis (SEA) and empirical based acoustics models. The FCM-PCA-GRNNs are useful when the room arrangement tends to change too frequently due to different design requirements from owner and designers during the preliminary design stage. Hence, the proposed FCM-PCA-GRNNs model helps to predict the SPL of different compartments effectively at different frequencies as it consumes less time and resources when compared to the commercial software that requires approximately 2–3

months to build the functional CAD model for predicting the offshore platform noise level. Thus, using of the proposed FCM-PCA-GRNN method for SPL prediction can be more efficient than the CAD-based methods, and more accurate than the empirical methods reviewed in the chapter 3; it is also more practical than the analytical methods proposed in chapter 4 and 5. In the future, more works can be done to improve the FCM partition and fuzzy membership functions for the multiple frequency-dependent data set.

Chapter 7.   Conclusions and Future work

This chapter summarises the main contributions and provides few recommendations for future research.

7.1. Conclusions and Contributions

In this thesis, three types of model were presented to predict the sound level for the offshore platform environment. They are namely: empirical model, analytical model, and FCM-PCA-GRNN model. The contributions from this thesis are as follows:

1. **Proposed a suitable empirical acoustic model for Type 1 machinery room in the offshore platform** [60]**.** Empirical formula is preferred by engineers as it is easy to apply and understand. However, an empirical formula that is suitable for predicting offshore platform sound level is not validated in the literature. By validating the five selected empirical SPL models originated from other applications with experimental measurements, the Heerema and Hodgson model [67] have shown to estimate the sound pressure level accurately for the offshore platform.

2. **Proposed SEA-DF method to compute the sound level for compartments governed by the direct field in the offshore platform at the high-frequency regime** [60]**.** After validated the empirical formula with experiment results, the SEA-DF method can calculate the sound levels in various type of compartments such as Type 1 and 2 machinery room, cabins and control room. It considered the direct field component, reverberation field component, room geometry, sound absorption, damping effect, sound transmission, and structure-borne noise propagation in the acoustics modelling. This method provides more information in the acoustic space where significant absorptive materials are present, and the direct field component from the sound source dominates the total sound field than just the reverberant field, where the latter becomes the basis for constructing the conventional SEA method.

3. **A complete analytical model for analysing the vibro-acoustics of the three-dimensional fully coupled structural-acoustic system with general boundary conditions was developed.** By considering of the structural interconnection force and the moment at edges, and structural-acoustic interaction on the interface, the structural and acoustic systems are fully coupled. Artificial spring technique was implemented to illustrate the general coupling and boundary conditions by assigning the springs with corresponding values. The Chebyshev expansions solutions were obtained under the

Rayleigh-Ritz frame and reliability of current method were validated by checking natural frequencies of present methodology against those derived from finite element software. The Chebyshev polynomial overcomes the convergence problem along the boundaries encountered by conventional Fourier series expansions and reduces the scale of matrices in the characteristic equation for coupled structure problem faced by using the improved Fourier series. Therefore, rapid convergence numerical stability with efficient accuracy solution can be achieved for solving complex configurations analytically. By comparing the displacement and pressure response between rigidly coupled boundary plates and disconnected boundary plates, it confirmed that the structural coupling should take into account when analysing the vibro-acoustic of marine platform environment. The proposed method can handle the vibro-acoustic problem without requiring any prior modal information that was widely needed in conventional model coupling approaches. The present analytical method was extended to solve the vibration behavior of the more complicated case such as the conjugate rooms [106]. Parametric studies on direct sound transmission and effect of structural coupling were performed.

4. **Proposed a modified multiple generalised regression neural network (GRNN) to predict the noise level of various compartments on-board of the offshore platform** [119]. Using the conventional GRNN model to maps the available inputs to SPL for the entire offshore platform can cause errors due to the following problems.

- Limited samples available during the initial design stage
- lacked of appropriate or/and exact inputs from the design variables (such as actual position of the noise sources, room dimensions, and other acoustic variables)

The proposed method overcomes these problems by incorporating pre-processing by using Fuzzy C-Means (FCM) clustering and Principal Component Analysis (PCA). With more relevant variables used in each cluster after the FCM-PCA, it consumes less computational time as compared to conventional GRNNs that applied to original data set with higher dimensions. The performance of FCM-PCA-GRNNs has improved significantly as the results show an improvement on the spatial sound pressure level (SPL) and 85% improvement on the spatial average SPL than just GRNNs alone. By comparing with data obtained from real engine room on a jack-up rig, the FCM-PCA-GRNNs noise model performs better with more than 10% less error than the empirical-based acoustic models. Additionally, the results show comparable performance to SEA-DF that requires more time and resources to solve

during the early stage of the offshore platform design. The FCM-PCA-GRNNs is therefore useful when the room arrangement tends to change too frequently due to different design requirements from owner and designers during the preliminary design stage. Hence, the proposed FCM-PCA-GRNNs model helps to predict the SPL of different compartments effectively as it consumes less time and resources when compared to the commercial acoustics software that requires two to three months to build the functional acoustics model.

7.2. Future work

The future works recommended for this research are as follows.

1. **Consider more complex situations or detailed structures in the offshore platform**. Analytical models are a very useful and precise tool. However, the present analytical model is based on simple cases constructed by flat surfaces. Actual offshore platform structures are made of stiffeners, girders, and brackets. The analytical model may take into the account these details to develop a complete solution. In addition, the analytical model for the conjugated rooms can be further extended to solve the coupled room by employing the domain partition technique and modifying the energy terms of the interior plate.

2. **Extend the FCM-PCA-GRNNs model to predict low-frequency sound levels.** The present FCM-PCA-GRNNs model showed good performance for high-frequency noise level prediction. The relevant input variable and training samples at low-frequency regime can be identified and collected from the analytical model for training and testing. It will enable the FCM-PCA-GRNNs model to perform noise prediction at low frequencies.

3. **Optimize and improve the computation efficiency of the proposed FCM-PCA-GRNNs model**. More works will be done to improve the FCM partition and fuzzy membership functions for the multiple frequency-dependent data set. In addition, use of appropriate smoothing parameter improves the generalisation ability of the GRNN model. An optimisation routine to obtain the smoothing parameter will be used to improve the sound pressure level prediction.

7.3. Publications

The following papers were published in the journals and conferences. The contents in these papers were used in various sections of Chapter 1 to 6 in this thesis.

[60] X. Ji and C. Chin, "Analysis of acoustic models and statistical energy analysis with direct field for machinery room on offshore platform," Acta Acustica united with Acustica, vol. 101, no. 6, pp.1234-1244, 2015. DOI: 10.3813/AAA.918916

[78] X. Ji, C. Chin and E. Mesbahi, "The effect of damping treatment for noise control on offshore platforms using statistical energy analysis," in 17th International Conference on Noise and Vibration Engineering, Amsterdam, 2015.

[105] X. Ji and C. S. Chin, "Analytical Modeling of Vibroacoustics Interaction for Conjugate Enclosures," in *Inter.Noise 2017*, Hong Kong, 2017.

[118] C. S. Chin, X. Ji, W. L. Woo, T. J. Kwee and W. X. Yang, "Modified multiple generalised regression neural network models using fuzzy C-means with principal component analysis for noise prediction of offshore platform," Neural Computing and Applications, pp. 1-16, 2017, DOI. 10.1007/s00521-017-3143-0.

References

[1] IMO, "MSC 91/22/ADD.1 ADOPTION OF THE CODE ON NOISE LEVELS ON BOARD SHIPS," 2012.

[2] ABS, "Guideline for Crew Habitability on Offshore Installations," 2012.

[3] NORSOK, "NORSOK STANDARD S-002, Working Environment," 2004.

[4] HSE, "Noise Exposure and Control in the Offshore Oil and Gas Industry," Health & Safety Executive.

[5] M. F. Mendes and M. A. d. S. Fran¢a, "Noise and Vibration: Computational Analysis Applied to Offshore Platforms and FPSOs," in *Proceedings of the Ninth International Offshore and Polar Engineering Conference*, Brest, France, 1999.

[6] J. M.C. and F. D., Sound, structures, and their interaction, MIT Press, 1993.

[7] A. Pierce, "An introduction ot its physical principles and applications," in *Acoustics*, New York, McGraw Hill, 1981.

[8] F. Ihlenburg, "Finite element analysis of acoustic scattering," in *Applied Mathematical Sciences*, vol. 132, New York, Springer-Verlag, 1998.

[9] H. Kuttruff, Room Acoustics, 5th Edition ed., CRC Press, 2009.

[10] W. L. Li, X. f. Zhang, J. t. Du and Z. g. Liu , "An exact series solution for the transverse vibration of rectangular plates with general elastic boundary support," *Journal of sound and vibration,* vol. 321, pp. 254-269, 2009.

[11] J. T. Du, G. y. Jin, T. j. Yang and Z. g. Liu, "An analytical method for the in-plane vibration analysis of rectangular plates with elastically restrained edges," *Journal of sound and vibration,* vol. 306, pp. 908-927, 2007.

[12] J. T. Du, W. L. Li, H. A. Xu and Z. G. Liu, "Vibro-acoustic analysis of a rectangular cavity bounded by a flexible panel with elastically restrained edges," *J. Acoust. Soc. Am,* vol. 131, no. 4, pp. 2799-2810, 2012.

[13] Y. Chen, G. Jin, S. Shi and Z. Liu, "A general analytical method for vibroacoustic analysis of an arbitrarily restrained rectangular plate backed by a cavity with general wall impedance," *Journal of Sound and Vibration,* vol. 136, pp. 031015-1-11, 2014.

[14] E. H. Dowell and D. Tang, Dynamics of very high dimensional system, New Jersey: World Scientific, 2003.

[15] D. Desmet, "A wave based prediction technique for coupled vibro-acoustic analysis," K.U. Leuven, Division PMA, Leuven, 2008.

[16] J. Pan and A. Bies, "The effect of fluid-structural coupling on sound waves in an enclosure—Theoretical part," *J. Acoust. Soc. Am,* vol. 87, pp. 691-707, 1990.

[17] R. B. Davis, "Technique to access acoustic-structure interaction in liquid rocket," Duke University, 2008.

[18] F. Fahy and P. Gardonio, Sound and structural vibration: radiation, transmission and response, Acadamic Press, 2007.

[19] M. C. Remillieux, S. M. Pasareanu and U. P. Svensson, "Numerical modeling of the exterior-to-interior transmission of impulsive sound through three-dimensional thin-wall elastic structures," *Journal of sound and vibration,* vol. 332, pp. 6725-6742, 2013.

[20] S. X. Shi, G. Y. Jin and Z. G. Liu, "Vibro-acoustic behaviour of an elastically restrained double-panel structure with an acoustic cavity of arbitrary boundary impedance," *Applied Acoustics,* vol. 76, pp. 431-444, 2014.

[21] H. Peters, N. Kessissoglou and S. Marburg, "Modal decomposition of exterior acoustic-structure interaction problems with model order reduction," *J. Acoust. Soc. Am. ,* vol. 135, pp. 2706-2717, 2014.

[22] H. Petersa, N. Kessissoglou and S. Marburg, "Modal decomposition of exterior acoustic-structure interaction," *Modal decomposition of exterior acoustic-structure interaction,* vol. 133, pp. 2668-2677, 2013.

[23] D. Arne, "Wave based calculation methods for sound-structure interaction," Katholieke Universiteit, 2011.

[24] E. Deckers, C. Claeys, O. Atak, J.-P. Groby, O. Dazel and W. Desmet, "A wave based method to predict the absorption, reflection and transmission coefficient of two-dimensional rigid frame porous structures with periodic inclusions," *Journal of Computational Physics,* vol. 312, pp. 115-138, 2016.

[25] A. Dijckmans and G. Vermeir, "A wave based model to predict the sound transmission through multilayered structures," in *9th National Congress on Theoretical and Applied Mechanics*, Brussels, 2012.

[26] B. Pluymers, W. Desmet, D. Vandepitte and P. Sas, "Application of an e\$cient wave-based prediction technique for the analysis of vibro-acoustic radiation problems," *Journal of Computational and Applied Mathematics ,* vol. 168, pp. 353-364, 2004.

[27] E. Trefftz , "Ein Gegenstuck zum Ritzschen Verfahren," in *International Congress on Applied Mechanics*, Zurich, Switzerland, 1926.

[28] Y. Zhang , J. DU, Y. Liu, T. Yang and Z. Liu, "Sound transmission between rooms coupled through partition with elastically restrained edges," in *Internoise 2014*, Melbourne, 2014.

[29] P. E. Cho and R. J. Bernhard, "Energy flow analysis of coupled beams," *Journal of Sound and Vibration,* vol. 211, pp. 593-605, 1998.

[30] Rayleigh, The Theory of Sound, 1877.

[31] R. Walter, "Theorie der transversalschwingungen einer quadratischen platte mit freien

randern," *Annalen Der Physik,* vol. 333, no. 4, pp. 737-786, 1909.

[32] O. Zienkiewicz and T. R, The finite element method, Butterworth-Heinermann, 2000.

[33] O. Zienkiewicz, T. R.L., Z. J.Z. and N. P., The Finite Element Method - The three volume set (6h ed.), Butterworth Heinemann, 2005.

[34] I. SENJANOVIĆ, Ship vibration III, Zagreb: University of Zagreb, 1990.

[35] T. Shuku and N. Ishihara, "The analysis of the acoustic field in irregularly shaped rooms by the finite element method," *Journal of Sound and Vibration,* vol. 29, pp. 67-76, 1973.

[36] T. Lodygowski and W. Sumelka, "Limitations in Application of Finite Element Method in Acoustic Numerical Simulation," *Journal of the Theoretical and Applied Mechanics,* vol. 44, no. 4, pp. 849-865, 2006.

[37] S. Maluski and B. Gibbs, "Application of a finiteelement model to low-frequency sound insulation in dwellings," *J. Acoust. Soc. Am,* vol. 108, pp. 1741-1751, 2000.

[38] José Guilherme Santos da Silva, Ana Cristina Castro Fontenla Sieira, Luciano Rodrigues Ornelas de Lima and Bruno Dias Rimola, "Vibration Analysis of an Oil Production Platform Submitted to Dynamic Actions Induced by Mechanical Equipment," in *Vibration Analysis and Control - New Trends and Developments*, InTech, 2011, pp. 281-308.

[39] A. Yucel and A. Arpaci, "Free and forced vibration analyses of ship structures using the finite element method," *Journal of Marine Science and Technology,* vol. 18, pp. 324-338, 2013.

[40] D. Duhamel, B. Mace and M. Brennan, "Finite element analysis of the vibrations of waveguides and periodic structure," *Journal of Sound and Vibration,* vol. 294, pp. 205-220, 2006.

[41] G. Robin, N. Mathieu, M. Jrad, E. Daya and F. Choquart, "The effect of the geometric parameters of the corrugation shape on the vibration analysis of 3D structured beams," *Mechanics Research Communications ,* vol. 84, pp. 65-71, 2017.

[42] C. Hong and K. Shin, "Modeling of wall pressure fluctuations for finite element structural analysis," *Journal of Sound and Vibration,* vol. 329, pp. 1673-1685, 2010.

[43] J. W. Ringberg, P. Ernholm and L. Hagstrom, "Analysis of free vibration characteristics and mode shaples of a semi-submersible platform," in *OMAE2011*, Rotterdam, The Netherlands, 2011.

[44] G. Everstine, "Finite element formulations of structural acoustics problems," *Comput. Struct,* vol. 65, no. 3, pp. 307-321, 1997.

[45] T. Kihlman and J. Plunt, "Prediction of noise levels on ships," in *Proceedings International Symposium of Shipboard Acoustics*, 1976.

[46] T. Kihlman and J. Plunt, "Structure-borne sound in ships, a study of different wave types," in *Proceedings International Congress on Acoustics (ICA 8)*, 1974.

[47] T. Kihlman and J. Plunt, "Prediction of noise level on ships," in *Proceedings International Symposium of Shipboard Acosutics*, 1976.

[48] N. A.C., "Noise prediction and prevention in ships," in *Ship vibration symposium* , Arlington, 1978.

[49] R. H. Lyon and T. D. Scharton, "Vibrational Energy Transmission in the Three Element Structures," *J. Acoust. Soc.,* pp. 253-261, 1965.

[50] P. Smith, "Response and radiation of structural modes excited by sound," *Journal of the Acoustical Society of Amercia,* vol. 34, pp. 640-647, 1962.

[51] B. R. Mace, "Statistical energy analysis, energy distribution models and system modes," *Journal of Sound and Vibration,* vol. 264, pp. 391-409, 2003.

[52] W. d. Lima and A. Ravindran, "Prediction of the cabin noise of business jet using statistical energy analysis," *The Journal of the Acoustical Society of America,* vol. 127, 2010.

[53] M. Sadri and D. Younesian, "Vibroacoustic analysis of a sandwich panel coupled with an enclosure cavity," *Composite Structures,* vol. 146, pp. 159-175, 2016.

[54] A. Culla, W. D'Ambrogio, A. Fregolent and S. Milana, "Vibroacoustic optimization using a statistical energy analysis model," *Journal of Sound and Vibration,* vol. 375, pp. 102-114, 2016.

[55] R. Ribeiro and M. Smith, "Use of SEA to Model the Sound Field in Large Acoustic Spaces," in *Forum Acusticum*, Budapest, 2005.

[56] L. Ye, P. Jie and S. Meiping, "Study on noise prediction and reduction in coupled workshops using SEA method," *International Scholarly Research Network,* 2011.

[57] G. Eddy, "Estimation methods for sound levels and reverberation time in a room with irregular shape or absorption distribution," *Acta Acustica United with Acustica,* p. 797, 2006.

[58] J. Yin , "Structure-borne sound transmission between isotropic, homogeneous plates and periodic ribbed plates," University of Liverpool , 2012.

[59] F. Fahy , "Statistical energy analysis: A critical overview.," *Philosophical Transactions of the Royal Society of London ,* vol. 346, pp. 429-554, 1994.

[60] X. Ji and C. Chin, "Analysis of acoustic models and statistical energy analysis with direct field for machinery room on offshore platform," *Acta Acustica united with Acustica,* vol. 1244, p. 1234, 2015.

[61] L. Maxit and J. Guyader, "Extension of SEA model to subsystems with nonuniform modal energy distribution," *Journal of Sound and Vibration,* vol. 265, pp. 337-358,

2003.

[62] A. Putra, A. Munawir and W. M. Farid, "Corrected Statistial Energy Analysis Model for Car Interior Noise," in *Advances in Mechanical Engineering*, 2014.

[63] J. M. Keith, "Architectural Acoustic Modeling of Ship Noise and Sound Field Mapping," *Journal of Sound & Vibration,* 2011.

[64] L. L. Beranek, Noise and vibration control engineering: principles and applications, New York: John Wiley and Sons, 1992.

[65] L.D. Mitchell, J.K. Thompson and C.J. Hurst, "A modified room acoustics approach to determine sound pressure levels in irregularly-proportioned factory spaces," in *Inter-Noise 76*, Washington DC, USA, 1976.

[66] R. W. Fischer, "Design Guide for Shipboard Airborne Noise Control," SNAME Technical & Research Bulletin, 1983.

[67] N. Heerema and M. Hodgson, "Emprical models for predicting noise levels, reverberaion times and fitting densities in indstrial workshops," *Applied Acoustics,* vol. 57, no. 1, pp. 51-60, 1999.

[68] M. V. Sergeyev, "Propagation of airborne noise in workshops of manufacturing companies," in *Reduction of Noise in Buildings and Residential Districts*, Moscow, Moscow Building Publication, 1987.

[69] J. M. Keith, "Architectural Acoustic Modeling of Ship Noise and Sound Field Mapping," *Journal of Sound & Vibration,* 2011.

[70] N. R. Heerema, "Empirical prediction and auralization of noise levels and reverberation times in industrial workrooms," The Faculty of Graduate Studies, University of British Columbia, 1996.

[71] "Machine learning," Wikipedia, [Online]. Available: http://en.wikipedia.org/wiki/Machine_learning.

[72] N. Vladimir, D. Danijela, C. Slobodan, D. Milan and B. Sasa, "Comparison of classical statistical methods and artificial neural network in traffic noise prediction," *Environmental Impact Assessment Review,* vol. 49, pp. 24-30, 2014.

[73] G. Cammarata, S. Cavalieri and A. Fichera, "A Neural Network Architecture for Noise Prediction," *Neural Networks,* vol. 8, no. 6, pp. 963-973, 1995.

[74] A. Mohsen, G. Rostam, M. Muharram and K. Hassan, "An empirical technique for predicting noise exposure level in the typical embroidery workrooms using artificial neural networks," *Applied Acoustics,* vol. 74, pp. 364-374, 2013.

[75] K. Menderes, "Experimentally vibration and noise analysis of two types of washing machines with a proposed neural network predictor," *Measurement,* vol. 47, pp. 184-192, 2014.

[76] G. P. Tan, D. F. Wang and Q. Li, "Vehicle Interior Sound Quality Prediction Based on Back Propagation Neural Network," *Procedia Environmental Sciences,* vol. 11, pp. 471 - 477, 2011.

[77] M. Michael and K. W. D, "Prediction of outdoor sound transmission loss with an artificial neural network," *Applied Acoustics,* vol. 67, pp. 324-345, 2006.

[78] X. Ji , C. Chin and E. Mesbahi, "The effect of damping treatment for noise control on offshore platforms using statistical energy analysis," in *17th International Conference on Noise and Vibration Engineering*, Amsterdam, 2015.

[79] K. S. Sum and J. Pan , "A study of the medium frequency response of sound field in a panel-cavity system," *Journal of the Acoustical Society of Amercia,* vol. 103, pp. 1510-1519, 1998.

[80] Y. H. Chen , G. Jin, S. Shi and Z. G. Liu, "A general analytical method for vibroacoustic analysis of an arbitrarily restrained rectangular plate backed by a cavity with general wall impedance," *Journal of Sound and Vibration,* vol. 136, pp. 031015-1-11, 2014.

[81] M. Pirnat, G. Cepon and M. Boltezar, "Structural-acoustic model of a rectangular plate-cavity system with an attached distributed mass and internal sound source: Theory and Experiment," *Journal of Sound and Vibration,* vol. 333, no. 7, pp. 2003-2018, 2014.

[82] K. Namcheol , "Aeroelastic Flutter Mechanisms of a Flexible Disk Rotrrating in an Enclosed Compressible Fluid," *Journal of Applied Mechanics,* vol. 71, pp. 120-130, 2004.

[83] J. Kyeong-Hoon and K. Heung-Seok, "Free vibration of multiple rectangular plates coupled with liquid," *International Journal of Mechanical Sciences,* vol. 74, pp. 161-172, 2013.

[84] S. Arash and R. R. Ahmad, "Effects of in-plane loads on free vibration of symmetrically cross-ply laminated plates resting on Pasternak foundation and coupled with fluid," *Ocean Engineering,* vol. 115, pp. 196-209, 2016.

[85] X. Xie, H. Zheng and Y. g. Qu, "A variational formulation for vibro-acoustic analysis of a panel backed by an irregularly-bounded cavity," *Journal of Sound and Vibration,* vol. 373, pp. 146-163, 2016.

[86] H. Seyyed M, K. Hojat A and S. Razgar, "Free vibration and dynamic response of a fluid-coupled double elliptical plat system using Mathieu function," *International Journal of Mechanical Sciences,* vol. 75, pp. 66-79, 2013.

[87] J. Nitin K and S. Venkata R, "Structural Acosutics of a Rectangular Panel Backed by a Cavity: An Analytical Matrix Approach," *Journal of Vibration and Acoustics,* vol. 139, pp. 031004-1-8, 2017.

[88] Y. Chen, G. Jin, Z. Feng and Z. Liu, "Modeling and vibro-acoustic analysis of elastically restrained panel backed by irregular sound space," *Journal of Sound and*

Vibration, vol. 409, pp. 201-216, 2017.

[89] J. Pan, "A third note on the prediction of sound intensity," *The Journal of the Acoustical Society of Amercia,* vol. 105, pp. 560-562, 1999.

[90] C.-G. Ahn, H.-G. Choi and J.-M. Lee, "Structural-acoustic coupling analysis of two cavities connected by boundary structures and small holes," *Journal of Vibration and Acoustic,* vol. 127, pp. 566-574, 2006.

[91] F. N.H and P. J, "On the free and forced vibration of single and coupled rectangular paltes," *Journal of the Acoustical Society of Amercia,* vol. 104, pp. 2204-216, 1998.

[92] J. t. Du, W. L. Li, Z. g. Liu, T. j. Yang and G. y. Jin, "Free vibration of two elastically coupled rectangular plates with uniform elastic boundary restraints," *Journal of sound and vibration,* vol. 330, pp. 788-804, 2011.

[93] G. Y. Jin, Y. H. Chen and Z. G. Liu, "A Chebyshev-Lagrangian method for acoustic analysis of rectgular cavity with arbitrary impedance walls," *Applied Acoustics,* vol. 78, pp. 33-42, 2014.

[94] S. Mehran, S. Rezgar and H. Seyyed Mohammad, "An analytical solution for free and forced vibration of a piezoelectric laminated plate coupled with an acoustic enclosure," *Computers and Methemetics with Applications,* vol. 69, pp. 1329-1341, 2015.

[95] R. P. M, A. S. A and K. M.S., "Analytical solution for free vibration of flexible 2D rectangular tanks," *Ocean Engineering,* vol. 122, pp. 118-135, 2016.

[96] M. Xianglong, J. Guoyong, S. Shuangxia, Y. Tiangui and L. Zhigang, "An analytical method for vibration analysis of cylindrical shells coupled with annular plate under general elastic boundary and coupling conditions," *Journal of Vibration and Control,* pp. 1-24, 2015.

[97] K. p. Zhang, T. Zhang, H. Wu and D. y. Shi, "Free vibration of a box-type structure by plates with arbitrary boundary conditions," in *Inter-noise* , Melbourne, 2014.

[98] J. Lee, "Application of Chebyshev-tau method to the free vibration analysis of stepped beams," *International Journal of Mechanical Sciences,* Vols. 101-102, pp. 411-420, 2015.

[99] D. Zhou, S. Lo and Y. Cheung, "3-D vibration analysis of annular sector plates using the Chebyshev-Ritz method," *Journal of Sound and Vibration,* vol. 320, pp. 421-437, 2009.

[100] M. Filippi, A. Pagani, M. Petrolo, G. Colonna and E. Carrera, "Static and free vibration analysis of laminated beams by refnied theory based on Chebyshev polynomials," *Composite Structures,* vol. 132, pp. 1248-1259, 2015.

[101] Y. Chen, G. Jin and Z. Liu, "Flexural and in-plane vibration analysis of elastically restrained thin rectangular plate with cutout using Chebyshev–Lagrangian method," *International Journal of Mechanical Sciences,* vol. 89, pp. 264-278, 2014.

[102] Q. Li, V. Iu and K. Kou, "Flexural and in-plane vibration analysis of elastically restrained thin rectangular plate with cutout using Chebyshev–Lagrangian method," in *Computational Methods in Engineering and Science*, Hainan,China, 2006.

[103] X. Xie, H. Zheng and Y. G. Qu, "A variational formulation for vibro-acoustic analysis of a panel backed by an irregularly-bounded cavity," *Journal of Sound and Vibration,* vol. 373, pp. 146-163, 2016.

[104] L. Fox and I. B. Parker, Chebyshev Polynomial in Numerial Analysis, Oxford University Press, 1972.

[105] Y. Chen , G. Jin, Z. Feng and Z. Liu, "Modeling and vibro-acoustic analysis of elastically restrained panel backed by irregular sound space," *Journal of Sound and Vibration,* vol. 409, pp. 201-216, 2017.

[106] X. Ji and C. S. Chin, "Analytical Modeling of Vibroacoustics Interaction for Conjugate Enclosures," in *Inter.noise 2017*, Hong Kong, 2017.

[107] L. Finn, C. Karin Noren and M. Christian, "Simulating low frequency sound transmission through walls and windows by a two-way coupled fluid structure interaction model," *Journal of Sound and Vibration,* vol. 396, pp. 203-216, 2017.

[108] J. Finn , P. Torben, R. Jens Holger, G. Anders Christian and O. Mogens, "Fundamentals of Acoustics and Noise Control," Department of Electrical Engineering, Technical University of Denmark, 2011.

[109] A. Osipov, P. Meesb and G. Vermeif, "Low-Frequency Airborne Sound Transmission through Single Partitions in Buildings," *Applied Acosutics,* vol. 52, pp. 273-288, 1997.

[110] A. C. Nilsson, "Noise Prediction and Prevention in Ships," New York, 1978.

[111] D. F. Specht, "A general regression neural network," *IEEE Transactions on Neural Networks,* vol. 2, pp. 568-576, 1991.

[112] M. F. Hamoda, "Modeling of Construction Noise for Environmental Impact Assessment," *Journal of Construction in Developing Countries,* vol. 13, p. 11, 2008.

[113] J. Nirmal, M. Zaveri, S. Patnaik and P. Kachare, "Voice conversion using General Regression Neural Network," *Applied Soft Computing,* vol. 24, pp. 1-12, 2014.

[114] J. l. Liu, W. Bao, L. Shi, B. q. Zuo and W. d. Gao , "General regression neural network for prediction of sound absorption coefficients of sandwich structure nonwoven absorbers," *Applied Acoustics,* vol. 76, pp. 128-137, 2014.

[115] N. Djarfour, J. Ferahtia, F. Babaia, K. Baddari, E. A. Said and M. Farfour, "Seismic noise filtering based on Generalized Regression Neural Networks," *Computers & Geosciences,* vol. 69, p. 10, 2014.

[116] J. Chatillon, "Influence of source directivity on noise level in industrial halls: Simulation and experiments," *Applied Acoustics,* vol. 68, no. 6, pp. 682-698, 2008.

[117] M. Hodgson, "Ray-tracing evaluation of empirical models for predicting noise in industrial workshops," *Applied Acoustics,* vol. 64, no. 11, pp. 1003-1048, 2003.

[118] P. Azma, A. Munawir , W. Mohamad and J. Mohammad, "The Effect of Direct Field Component on a Statistical Energy Analysis (SEA) Model," *Applied Mechanics and Materials,* vol. 471, pp. 279-284, 2013.

[119] C. S. Chin, X. Ji , W. L. Woo, T. J. Kwee and W. x. Yang, "Modified multiple generalized regression neural network models using fuzzy C-means with principal component analysis for noise prediction of offshore platform," *Neural Computing and Applications,* pp. 1-16, 2017.

[120] Z. d. Wu, W. x. Xie and J. p. Yu, "Fuzzy C-Mean Cluster Algorithm based on Kernel Method," in *Proceednigs of the Fifth International Conference on Computational Intelligence and Multimedia Applications*, Xi'an, China, 2003.

[121] A. Strehl, "Relationship-based clustering and cluster ensembles for high-dimensional data mining," The University of Texas at Austin, PhD Dissertation, 2002.

[122] S. Ghosh and S. Dubey, " Comparative analysis of K-means and fuzzy C-means algorithms," *Int J Adv Comput Sci Appl ,* vol. 4, pp. 35-39, 2013.

[123] J. Heinrich and D. Weiskopf, "State of the art of parallel coordinates," in *EUROGRAPHICS 2013*, Girona, Spain, 2013.

[124] Y. h. Lu, T. h. Ma, C. h. Yin, X. y. Xie, W. Tian and S. m. Zhong, "Implementation of the Fuzzy C-Means Clustering Algorithm in Meteorological Data," *Internationa Journal of Database Theory and Application,* vol. 6, no. 5, pp. 1-18, 2013.

[125] J. Nirmal, M. Zaveri, S. Patnaik and P. Kachare, "Voice conversion using General Regression Neural Network," *Applied Soft Computing,* vol. 24, p. 13, 2014.

[126] A. U. Ozturk and M. E. Turan, "Prediction of effects of microstructural phases using generalized regression neural network," *Construction and Building Materials,* vol. 29, p. 5, 2012.

[127] M. Miroslaw, "Acoustic energy density distribution and sound intensity vector field inside coupled spaces," *J. Acoust. Soc. Am. ,* vol. 132, pp. 228-238, 2012.

[128] C. CristinaDíaz, P. J. Poblet and F. A. Rodr´ıguez, "Numerical estimation of coupling loss factors in building acoustics," *Journal of Sound and Vibration,* vol. 332, pp. 5433-5450, 2013.

[129] A. Dijckmansa, G. Vermeir and W. Lauriks, "Sound transmission through finite lightweight multilayered structures with thin air layers," *J. Acoust. Soc. Am.,* vol. 128, pp. 3513-3524, 2010.

[130] B. Alexis, P. Judicael and V. Vincent, "Acoustic Predictions in Industrial Spaces Using a Diffusion Model," *Advances in Acoustics and Vibration,* vol. 2012, 2012.

[131] X. Ning , E. Jose , N. Juan M and J. Yun , "Investigation on the effect of aperture sizes and receiver positions in coupled rooms," *J. Acoust. Soc. Am.,* vol. 133, pp. 3975-3985,

2013.

[132] S. Jason E, T. Rendell R. and S. Yasushi, "Statistical-acoustics models of energy decay in systems of coupled rooms and their relations to geometrical acoustics," *J. Acoust. Soc. Am. ,* vol. 116, pp. 958-969, 2004.

[133] N. Xiang and J. E. Summers, "ACOUSTICS IN COUPLED ROOMS: MODELLING AND DATA ANALYSIS," in *International Symposium on Room Acoustics ,* Seville, 2007.